

Fall 1993

Computer aided stress analysis of the femur with prosthetic hip stem utilizing computed tomography

Wei-Chun Chang

New Jersey Institute of Technology

Follow this and additional works at: <https://digitalcommons.njit.edu/dissertations>



Part of the [Mechanical Engineering Commons](#)

Recommended Citation

Chang, Wei-Chun, "Computer aided stress analysis of the femur with prosthetic hip stem utilizing computed tomography" (1993). *Dissertations*. 1084.

<https://digitalcommons.njit.edu/dissertations/1084>

This Dissertation is brought to you for free and open access by the Theses and Dissertations at Digital Commons @ NJIT. It has been accepted for inclusion in Dissertations by an authorized administrator of Digital Commons @ NJIT. For more information, please contact digitalcommons@njit.edu.

Copyright Warning & Restrictions

The copyright law of the United States (Title 17, United States Code) governs the making of photocopies or other reproductions of copyrighted material.

Under certain conditions specified in the law, libraries and archives are authorized to furnish a photocopy or other reproduction. One of these specified conditions is that the photocopy or reproduction is not to be “used for any purpose other than private study, scholarship, or research.” If a user makes a request for, or later uses, a photocopy or reproduction for purposes in excess of “fair use” that user may be liable for copyright infringement,

This institution reserves the right to refuse to accept a copying order if, in its judgment, fulfillment of the order would involve violation of copyright law.

Please Note: The author retains the copyright while the New Jersey Institute of Technology reserves the right to distribute this thesis or dissertation

Printing note: If you do not wish to print this page, then select “Pages from: first page # to: last page #” on the print dialog screen

The Van Houten library has removed some of the personal information and all signatures from the approval page and biographical sketches of theses and dissertations in order to protect the identity of NJIT graduates and faculty.

INFORMATION TO USERS

This manuscript has been reproduced from the microfilm master. UMI films the text directly from the original or copy submitted. Thus, some thesis and dissertation copies are in typewriter face, while others may be from any type of computer printer.

The quality of this reproduction is dependent upon the quality of the copy submitted. Broken or indistinct print, colored or poor quality illustrations and photographs, print bleedthrough, substandard margins, and improper alignment can adversely affect reproduction.

In the unlikely event that the author did not send UMI a complete manuscript and there are missing pages, these will be noted. Also, if unauthorized copyright material had to be removed, a note will indicate the deletion.

Oversize materials (e.g., maps, drawings, charts) are reproduced by sectioning the original, beginning at the upper left-hand corner and continuing from left to right in equal sections with small overlaps. Each original is also photographed in one exposure and is included in reduced form at the back of the book.

Photographs included in the original manuscript have been reproduced xerographically in this copy. Higher quality 6" x 9" black and white photographic prints are available for any photographs or illustrations appearing in this copy for an additional charge. Contact UMI directly to order.



University Microfilms International
A Bell & Howell Information Company
300 North Zeeb Road, Ann Arbor, MI 48106-1346 USA
313/761-4700 800/521-0600

Order Number 9417353

**Computer aided stress analysis of the femur with prosthetic hip
stem utilizing computer tomography**

Chang, Wei-Chun, Ph.D.

New Jersey Institute of Technology, 1994

Copyright ©1994 by Chang, Wei-Chun. All rights reserved.

U·M·I

**300 N. Zeeb Rd.
Ann Arbor, MI 48106**

ABSTRACT

Computer Aided Stress Analysis of The Femur with Prosthetic Hip Stem Utilizing Computed Tomography

**by
Wei-Chun Chang**

A computer aided design and analysis method, utilizing computed tomography (CT) is developed, which together with a finite element program determines the stress and deformation patterns in the femur with hip prosthesis. The CT scan data file provides the geometry and the material parameters for the generated finite element model. The three-dimensional finite element model of the femur with hip prosthesis is automatically generated from the CT data file by a preprocessing procedure. The preprocessor includes a CT image display, edge detector, nodes generation, prosthesis simulator, mesh generator and model display. The loading conditions applied on the finite element model are determined from existing gait analysis including joint force and muscle force. Formatted input data for ANSYS (Swanson Analysis Systems Inc.) finite element program is generated by the preprocessor.

In this research, the influence on the stress pattern of different prosthetic materials and fixation, such as cobalt-chromium alloy or titanium alloy prosthesis, also cemented or porous-coated prosthesis are studied. A comparison of the stress patterns for the three different femora is made and a radiographic follow-up study in two cases is carried out at 14 months and 12 months postoperation for analyzing the bone remodeling process.

As a result of the calculated stress patterns in the femur with prosthesis, it is found that the cobalt-chromium alloy prosthesis unloads the calcar cortical bone and the titanium alloy prosthesis decreases the stress within the prosthetic stem except for the proximal side. The highest calculated stress is approximately 12% of the fatigue limit for cobalt-chromium alloy prosthesis, and approximately 4% for the titanium alloy prosthesis.

Comparing the porous coating model with the cemented model, the porous coating model leads to decreased bone stresses, reduced stress concentrations in bone surrounding the prosthesis and more uniformly distributed stress to the surrounding bone tissue. For the effect of stiffness and Poisson's ratio of the porous coating layer, lower elastic modulus and Poisson's ratio will reduce the interface stress between cancellous bone and the porous coating layer. The average stress of the fractured femur with prosthesis is approximately twice the amount of the femur with prosthesis in the proximal and distal side of the prosthetic stem. Furthermore the average stress of the male femur with prosthesis is about 4% lower than the female femur with prosthesis. In regards to stress changes in the postoperative femur, the bone remodeling results indicate that bone resorption of the cortex around the proximal prosthesis would increase the stress in the proximal prosthetic stem and femoral surface slightly while decreasing the stress of the midregion. Bone hypertrophy around the distal prosthesis would decrease the stress up to 35% in the distal prosthetic stem and femoral surface.

**COMPUTER AIDED STRESS ANALYSIS
OF THE FEMUR WITH PROSTHETIC HIP STEM
UTILIZING COMPUTED TOMOGRAPHY**

**by
Wei-Chun Chang**

**A Dissertation
Submitted to the Faculty of
New Jersey Institute of Technology
in Partial Fulfillment of the Requirements for the Degree of
Doctor of Philosophy**

Department of Mechanical and Industrial Engineering

January 1994

Copyright © 1994 by Wei-Chun Chang
ALL RIGHTS RESERVED

APPROVAL PAGE

COMPUTER AIDED STRESS ANALYSIS OF THE FEMUR WITH PROSTHETIC HIP STEM UTILIZING COMPUTED TOMOGRAPHY

Wei-Chun Chang

Dr. Martin J. Linden, Dissertation Advisor Professor of Mechanical Engineering of the Department of Mechanical and Industrial Engineering, NJIT	Date
---	------

Dr. Rong-Yaw Chen, Committee Member Professor of Mechanical Engineering and Graduate Advisor of the Department of Mechanical and Industrial Engineering, NJIT	Date
---	------

Dr. Peter Engler, Committee Member Associate Professor of Electrical Engineering and Assistant Chairperson of the Department of Electrical Engineering and Computer Engineering, NJIT	Date
---	------

Dr. Nouri Levy, Committee Member Associate Professor of Mechanical Engineering of the Department of Mechanical and Industrial Engineering, NJIT	Date
---	------

Dr. Clarence W. Mayott, Committee Member Assistant Professor of Mechanical Engineering of the Department of Mechanical and Industrial Engineering, NJIT	Date
---	------

BIOGRAPHICAL SKETCH

Author: Wei-Chun Chang

Degree: Doctor of philosophy in Mechanical Engineering

Date: January, 1994

Undergraduate and Graduate Education:

- Doctor of Philosophy in Mechanical Engineering,
New Jersey Institute of Technology, Newark, NJ, 1994
- Master of Science in Mechanical Engineering,
New Jersey Institute of Technology, Newark, NJ, 1990
- Bachelor of Science in Mechanical Engineering,
Feng-Chia University, Taichung, Taiwan, 1986

Major: Mechanical Engineering

Presentations and Publications:

Chang, W. C., M. J. Linden, S. Robbins, C. Mayott, and P. Engler, "Computer Aided Stress Analysis of The Femur With Prosthetic Hip Stem Utilizing Computed Tomography." 19th IEEE Annual Northeast Bioengineering Conference, March, 1993, PP. 60-61.

**This dissertation is dedicated to my beloved parents and wife
Wu-Lia Chang, Li-hsiang Jao and Shu-Fen Huang**

ACKNOWLEDGMENT

I wish to express my sincere gratitude to my advisor, Dr. Martin J. Linden, for his guidance, and encouragement throughout this research. I would like to thank Steven Robbins M. D. at Saint Barnabas Medical Center for his generous advice and providing resources necessary to accomplish this work.

I would also like to thank Dr. Clarence W. Mayott for his invaluable and knowledgeable remarks. Thanks in particular to Dr. Peter Engler for his encouragement and support. Additionally, sincere thanks to Dr. Rong-Yaw Chen and Dr. Nouri Levy for serving as members of the committee.

I gratefully acknowledge Mr. Thomas R. Fisler and Mr. Tom Curry for their assistance. I especially thank my parents and wife for their love and continuing support throughout my studies.

TABLE OF CONTENTS

Chapter	Page
1 INTRODUCTION	1
1.1 The Application of Finite Element Methods in Orthopedics	1
1.2 Femur Morphology	5
1.3 Computed Tomography	10
1.4 Mechanical Properties Description in Femoral Bone	16
1.5 Stress Analysis of the Femur with a Prosthesis	21
1.5.1 Finite Element Model	22
1.5.2 Loading Patterns	26
1.6 Objectives	28
2 THEORETICAL APPROACH.....	32
2.1 Introduction	31
2.2 Stress and Strain	31
2.2.1 Definitions	31
2.2.2 Stress-Strain Relations	33
2.3 Stress in a Cylindrical Shaft	35
2.4 Finite Element Method	39
3 FEMORAL PROSTHESIS	44
3.1 Introduction	44
3.2 Design Criteria for Femoral Prostheses	45
3.2.1 Introduction	45
3.2.2 Design Principles	46
3.3 Material Properties of Prostheses	50
3.3.1 Introduction	50
3.3.2 Metal	50

TABLE OF CONTENTS (Continued)

Chapter	Page
3.3.3 Ceramic	51
3.3.4 Polymers	52
3.4 Bone Cement Interface	53
3.4.1 Introduction	53
3.4.2 Mechanical Properties	54
3.5 Porous-Coated System	56
3.5.1 Introduction	56
3.5.2 Porous Materials Developed for Bone Ingrowth	56
3.5.3 Mechanical Properties	58
4 MATERIALS AND METHODS	61
4.1 Scanning Femoral Bones	61
4.2 Processing the CT Data	63
4.2.1 Transferring the CT data	63
4.2.2 Structure of the CT Data	64
4.2.3 Converting the CT Data	64
4.3 Reconstruction and Display	65
4.3.1 Reconstructing the CT Images	65
4.3.2 Gray Level Images and Color Display	67
4.4 The Design of Auxiliary Software for a Finite Element Program	71
4.4.1 Introduction	71
4.4.2 Edge Detection	74
4.4.3 The Node Selection Method	77
4.4.3.1 Straight Search	77
4.4.3.2 Radial Search	80

TABLE OF CONTENTS

(Continued)

Chapter	Page
4.4.4 The Bone Prosthesis Simulation	82
4.4.5 Mesh Generation	86
4.4.6 Elastic Properties Definition	90
4.4.6.1 Radiographic Density-Apparent Density Relationship	92
4.4.6.2 Calculation of Elastic Modulus in The Cortical Bone Element ..	94
4.4.7 Loading and Boundary Conditions	96
4.4.8 Generating the Finite Element Model	97
4.4.8.1 The Uniform Cylinder Model	97
4.4.8.2 The CT Data Model	101
4.5 Model Verification	101
5 RESULTS AND DISCUSSION	104
5.1 Stress Analysis of the Femur with a Prosthesis at Preoperation	104
5.2 Comparison of Stress Pattern with Previous Works.....	112
5.3 Evaluation of Three Cases.....	119
5.4 Bone Remodeling.....	120
5.5 Discussion	130
5.6 CT Data Applied in CAD/CAM System	133
5.6.1 Creating 3D Bone Geometry in CAD System	133
5.6.2 Creating 3D Bone Model in SLA Machine	135
6 CONCLUSION	139
APPENDIX A: STRESS PATTERNS OF THE FEMUR WITH PROSTHESIS	143
APPENDIX B: FORMULATION OF FINITE ELEMENT METHOD.....	158
BIBLIOGRAPHY	161

LIST OF TABLES

Table	Page
1.1 Typical CT number for various tissues	15
3.1 Mechanical properties of 316 L stainless steel, Co-Cr alloy, Ti and Ti-6Al-4V	51
3.2 Properties of polyethylene	53
3.3 Typical mechanical properties of some acrylics	55
3.4 Ultimate tensile strength and apparent modulus of elasticity of porous polysulfone	59
3.5 Ultimate compressive strength of Ti-6% and Al-4% V-VMC porous structure	60
4.1 The scanned information for the femora	62
4.2 Material properties for each material region of the femur and prosthesis	91
4.3 The comparison of calculated results between the elastic theory and the finite element method	103
5.1 The maximum stress quantities along the interfaces and femoral surface	110
5.2 Failure criteria for metal alloys used in total joint replacement	110
5.3 Failure criteria for bone and acrylic cement	112
5.4 Comparison of the finite element model with previous studies	115
5.5 The comparison of the external modeling between the bone-remodeling theory and the measurement from radiographs	128

LIST OF FIGURES

Figure	Page
1.1 Flow diagram of the finite element method for solving static problems	4
1.2 The anterior aspect of the right femur	6
1.3 The structure of a femoral bone	9
1.4 Principle of CT system with translating and rotating source-detector	11
1.5 X-ray attenuation of the cross sectional pixels	12
2.1 (a) External loads acting the femur (b) 3-D internal loads in a cross section of a femoral diaphysis (c) The orientations of the bending moments with respect to the principal inertia axes are shown	38
3.1 Essential design criteria currently under discussion for an ideal cemented stem design in total hip replacement	48
4.1 The reconstructed area of the scanned femoral cross section	66
4.2 The reconstructed images of Case 1	68
4.3 The reconstructed images of Case 2	69
4.4 The reconstructed images of Case 3	70
4.5 The CT scans generated by the different threshold values (a) 1100 (b) 1200 (c) 1280 (d) 1400 for the first cross section of Case 1	75
4.6 The cross section borders as defined in the edge detector	76
4.7 Definition of the selected lines in straight searching method	79
4.8 Display of selected nodes in straight searching method	79
4.9 The scanned cross sections and the selected nodes in Case 1 for image number (a) 5, (b) 6, (c) 9, and (c) 10	81
4.10 The simulated prosthetic hip stem in (a) anterior (b) lateral view	83
4.11 Display of selected nodes in each cross section of the femur with prosthesis	85
4.12 An analyzed model of a femur with prosthesis	87
4.13 (a) The element definition of a brick-type element. (b) The element definition for the prosthesis part of radial node selecting routine	89

LIST OF FIGURES (Continued)

Figure	Page
4.14 The correlation between radiographic density and apparent density	93
4.15 A two dimensional element consists of two triangles and one trapezoid	95
4.16 Coordinate system and loading conditions of the femur with prosthesis	96
4.17 The 3D finite element model of a uniform cylinder with prosthesis	98
4.18 The 3-D finite element model of Case 1 with prosthesis generated by CT data	99
4.19 The 3-D finite element model of Case 3 with prosthesis generated by CT data ...	100
4.20 (a) External loads acting at the femur and the femoral geometric dimensions (b) The geometric dimension in a cross section of a femoral diaphysis	102
5.1 Characterization of 3-D stress state at a geometric point of the femur with prosthesis model	105
5.2 The hip joint force acting on an uniform cylinder with cemented stem (a) The longitudinal normal stress distribution along the cylinder surface (b) The longitudinal normal stress distribution along the metal stem	106
5.3 The hip joint force and the muscle force acting on an uniform cylinder with cemented stem (a) The longitudinal normal stress distribution along the cylinder surface (b) The longitudinal normal stress distribution along the metal stem	106
5.4 The percentage of load transfer in (a) cemented (b) porous-coated structure. The stress values of proximal prosthetic stem serve as the reference values, which are (a) 54.6 MPa (b) 44.7 MPa	111
5.5 Comparison of the longitudinal stress distribution of medial side along prosthetic surface with previous stress analyses for the cemented femur- prosthesis	113
5.6 Comparison of the longitudinal stress distribution of lateral side along prosthetic surface with previous stress analyses for the cemented femur- prosthesis	113
5.7 Comparison of the longitudinal stress distribution of medial side along femoral surface with previous stress analyses for the cemented femur-prosthesis	114

LIST OF FIGURES (Continued)

Figure	Page
5.8 Comparison of the longitudinal stress distribution of lateral side along femoral surface with previous stress analyses for the cemented femur-prosthesis	114
5.9 Comparison of the normalized longitudinal stress distributions on the medial prosthetic stem with previous stress analyses	117
5.10 Comparison of the normalized longitudinal stress distributions on the lateral prosthetic stem with previous stress analyses	117
5.11 Comparison of the normalized longitudinal stress distributions on the medial femoral surface with previous stress analyses	118
5.12 Comparison of the normalized longitudinal stress distributions on the lateral femoral surface with previous stress analyses	118
5.13 Anteroposterior radiographs showing the pattern of femoral remodeling in Case 1 (a) Immediate postoperative radiograph (b) 14 months postoperative radiograph	122
5.14 Lateral radiographs showing the pattern of femoral remodeling in Case 1 (a) Immediate postoperative radiograph (b) 14 months postoperative radiograph	123
5.15 Anteroposterior radiographs showing the pattern of femoral remodeling in Case 2 (a) Immediate postoperative radiograph (b) 12 months postoperation for left femur and 1 month postoperation for right femur	124
5.16 Illustration showing the bone remodeling in Case 1 and Case 2 measured on the anteroposterior radiograph of the femur	125
5.17 Three-dimensional femoral models for (a) a fractured femur, and (b) a normal shape femur are constructed in CAD system	134

LIST OF SYMBOLS

Symbol	Meaning
A	Area of cross section
C	Elastic constant of material
E	Modulus of Elasticity
F	Applied force
F_i	Force matrix
f	Frictional force
G	Shear modulus of elasticity
h	Element length
I	Moment of inertia
K_i	Stiffness matrix
L	Beam length
M	Applied moment
M_T	Applied torque
r	Radius
T	Stress tensor
u	Displacement in the x direction
v	Displacement in the y direction
w	Displacement in the z direction
σ	Normal stress
τ	Shear stress
ϵ	Normal strain
γ	shear strain
ν	Poisson's ratio
θ	Twist per unit length

CHAPTER 1

INTRODUCTION

1.1 The Application of Finite Element Methods in Orthopedics

The process of calculating the stress in any body from applied forces, called stress analysis, is a well established discipline. There are a variety of theoretical stress analysis techniques. The most popular method is the finite element method which is a computational technique. The popularity of the method is due to its ability to handle various geometries, loading conditions and material properties. This popularity and quick acceptance is based on the fact that the analysis can be displayed using computer graphics. This organization of the elements which represents the structure to be analyzed, is called the finite element mesh. Graphical display of this mesh allows some of the characteristics of the model, as well as the results, to be quickly communicated — even to those not familiar with the details of the solution method (Cowin, 1989; Pilkington et al., 1993).

A finite element model describes the four relevant aspects of a structure; loading conditions, geometry, material properties and boundary conditions. The geometric shape of an element is defined by geometric points, called nodes. Each node in a finite element model is referenced by a number (a node number) that is uniquely assigned to it. Thus, each node represents a geometric coordinate position. Nodes are required at the corner of each element, but additional nodes, called side nodes, may be present along the line or curve that connects these corner nodes.

The element mesh is usually generated automatically (at least partly) by a computer program, called a finite element preprocessor. This program organizes the mesh numbering, generates a nodal-point coordinate file (the element member and accessory nodal point numbers), and a nodal-point coordinate file (the nodal-point numbers and their three dimensional coordinates). In these two files the element mesh (geometry) is

completely characterized. The finite element program further requires an element characteristics file containing element of material properties, such as Young's modulus and Poisson's ratio. This file contains the numbers of the nodal points at which forces are introduced to the structure, the direction of these force, and their magnitudes.

Based on this information, the finite element program calculates the displacements of all nodal points and calculates the stresses from material properties in all nodes and in the element centroids. The solution is obtained numerically through a set of linear equations, equal to the number of degrees of freedom in the model. The number of degrees of freedom is the number of nodal points times the number of displacement components in each node (two in a 2-D, three in a 3-D model). The computer time and memory space required for a problem depends on the number of degrees of freedom. A time-efficient element mesh is of crucial importance, due to the fact that computer capacity is the only practical limit to the level of model complexity feasible.

Finite element analysis as applied in stress analysis is based on the principle of minimum potential energy. This states that a loaded structure deforms in such a way that the energy stored within it is minimum. The characteristic feature of the finite element is that the total energy in the structure is discretized in individual contributions of each element. All (internal) forces working on an element are assumed to be concentrated in the nodal points. The relation between these nodal point forces and the nodal point displacements is expressed by a collection of parameters, called the element stiffness matrix. The parameters in this matrix depend on the specific nature of the element and on the properties of the material it represents. By applying the Newton's law to nodal points (a node belongs to more than one element), the requirements of compatibility (an element must not deform in such a way that it "looses" its neighbors), and the element stiffness matrices, the stiffness matrix of the whole structure is assembled. This matrix characterizes the energy in the structure (ANSYS User's Manual, 1990; Cowin, 1989; Huiskes, 1983).

Defining a degree of freedom as a displacement or rotation of a node, the stiffness equation can be formed:

$$[k] \times [d] = [r] \quad (1.1)$$

where $[k]$ is the stiffness matrix, $[d]$ is the nodal displacement vector and $[r]$ is the vector of each element nodal load. The stiffness matrix is always symmetric and positive definite for structural problems and for governing differential equations that are self adjoint. The diagonal coefficients, k_{ii} , are always positive and relatively large when compared to the off-diagonal values in the same row (see Section 2.5). The matrix and vector dimensions depend on the number of degrees of freedom in the element nodes. In the finite element program, the system is:

$$[K] \times [D] = [R] \quad (1.2)$$

which consists of the same terms used in the previous equation except that these are global elements. This equation can be solved for $[D]$. Hence, because $[d]$ for each element is contained in $[D]$, deformations of all elements are known. From deformations, the stresses are computed at the model elements using linear elastic theory (ANSYS User's Manual, 1990; Cook, 1981; Reddy, 1984).

If a stress or displacement field satisfies equilibrium, compatibility and boundary conditions, then a solution has been found. This is related to finite element analysis in a sense that if elements are based on displacement fields, so that nodal displacements are the primary unknowns, then the compatibility condition is satisfied within elements. Suitably chosen fields also provide compatibility between elements and satisfy displacement boundary conditions. Equilibrium equations and boundary conditions on stress are satisfied only approximately. The approximation improves as more degrees of freedom are used and, barring computational difficulties, the exact solution is achieved in the limit of infinitely refined mesh (Figure 1.1).

The most difficult steps in finite element analyses are the creation of the model and the interpretation of results in the light of the model limitations. Considerable expertise is

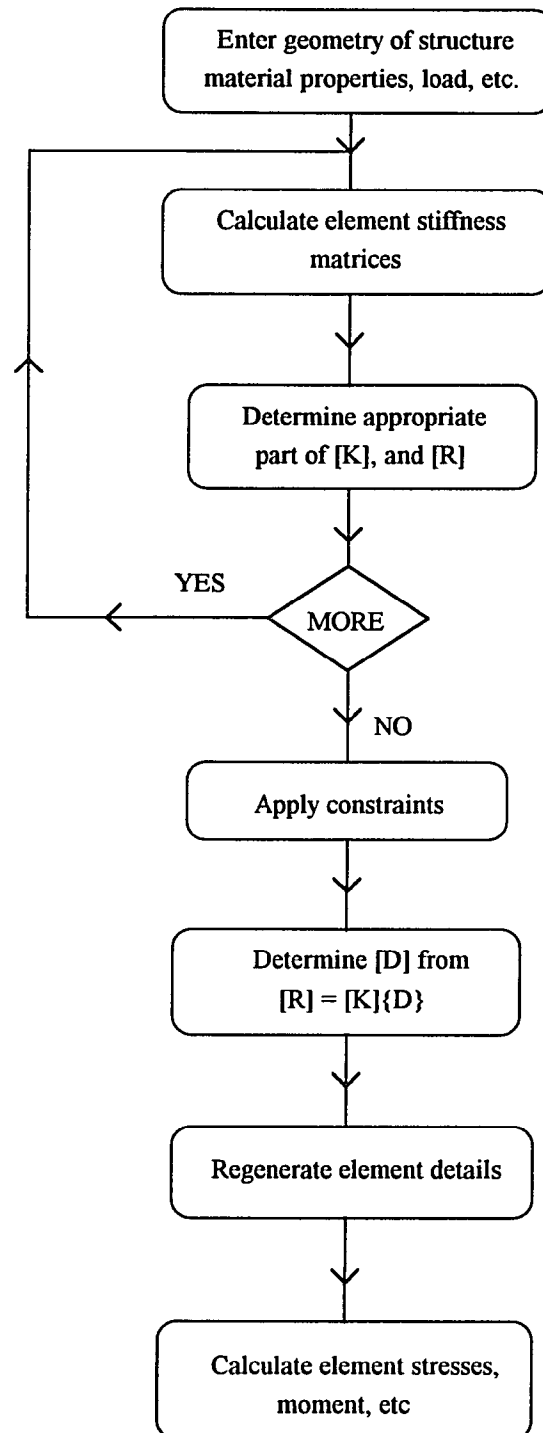


Figure 1.1 Flow diagram of the finite element method for solving static problems.

needed to judge the accuracy, the validity, and the significance of the computer output. Accuracy is mainly a question of adequate (local) mesh density. Convergence checks (repeating the calculations with a finer mesh) are always feasible, but sometimes expensive. Judging the validity of results requires a realistic assessment of model limitations. Another possibility is the use of verifying experiments on laboratory models, which may be simulated in finite element models to compare theoretical with experimental results.

Modeling the femur and the prosthesis for finite element analysis requires determining the bone geometry, then designing the prosthesis. Accurately determining bone boundaries is difficult due to the complex bone geometry. With the development of the computed tomography (CT), it is now possible to obtain bone structures. CT technique displays a three-dimensional image of bone, using a series of two-dimensional cross sectional scans of the bone. The CT data can be transformed to establish a three-dimensional finite element model.

Complex boundary conditions, together with the intricate bone geometry and the anisotropic, nonhomogenous, viscoelastic mechanical properties all affect the accuracy of conventional finite element stress analyses of the femoral bones with prostheses. The method of using the computed tomography provides an efficient model for the finite element stress analysis of the femur with prosthesis.

1.2 Femur Morphology

Human bones may be described as belonging to one of five general categories: long bones, such as the femur and the tibia; short bones, such as found in the wrist and ankle; flat bones, such as the skull; irregular bones, and sesamoid bones (Revell, 1986; Wheeler and Burkitt, 1987). The femur (Figure 1.2) is the longest and strongest bone in the body. Its shaft is nearly cylindrical and fairly uniform in caliber, but its two ends are quite irregular. The inferior extremity of the bone is broadened to form the knee joint and has smooth

articular surfaces for the condyles of the tibia and the facets of the patella. The superior extremity of the bone has a nearly spherical head mounted on an angulated neck and prominent trochanters provide for muscle attachments (Hamilton, 1976; Woodburne, 1983).

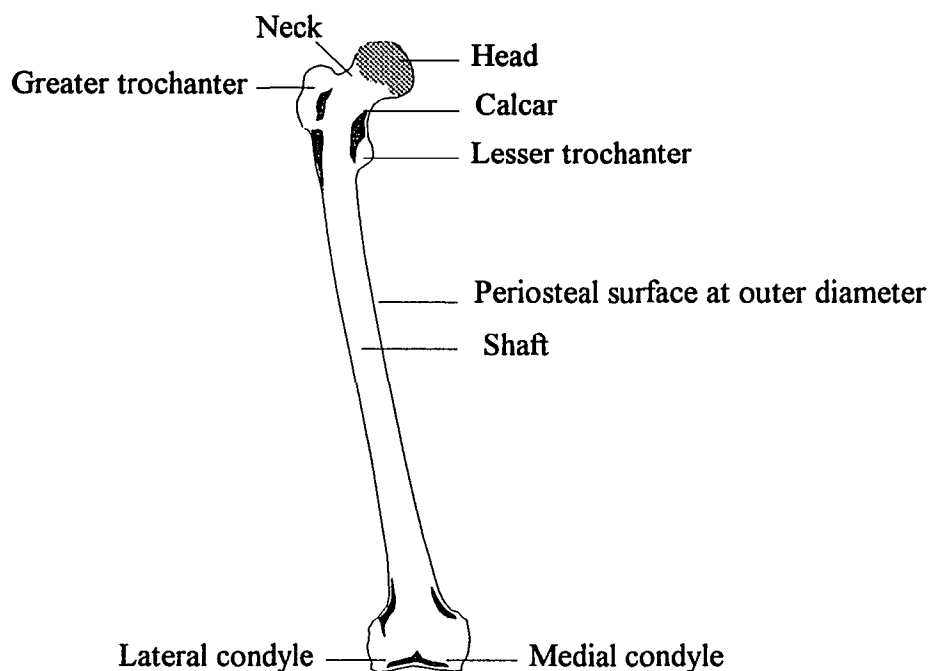


Figure 1.2 The anterior aspect of the right femur.

The head of the femur is smooth and forms about two-thirds of a spherical surface. Below the center of the head medially there is a pit for the attachment of the ligamentum flavus. The head, except for the depression in it, is covered with hyaline cartilage and articulates with the acetabulum to form the hip joint.

The neck is a strong buttress of bone which connects the head with the shaft in the region of trochanters. It is compressed anteroposteriorly and contains a large number of prominent pits, especially on its posterosuperior aspect, for the entrance of blood vessels. The neck is about 5 cm long and allows the femur free movement without interference of contact. The neck forms an angle with the shaft, which varies in the normal individual

from 115 to 140°. The head also points somewhat forward as the result of a forward angle between the neck and shaft, which averages 8°. The superior border of the neck leads to the greater trochanter; the inferior border slopes down and approaches the direction of the shaft as it ends in the lesser trochanter.

The greater trochanter is a large, square prominence on the upper end of the femur. It is separated from the smooth shaft below by a horizontal ridge. The greater trochanter is the bony prominence of the hip joint and is palpable 12 or 14 cm below the iliac crest. The lateral quadrilateral surface of the greater trochanter is divided by an oblique ridge which runs between its posterosuperior and anteroinferior angles. Its posterior rounded border bounds the trochanteric fossa and contributes to the intertrochanteric crest. The trochanteric fossa is a deep pit on the medial aspect of the greater trochanter.

The lesser trochanter, to which are attached the psoas and iliacus, is a smaller rounded projection where the lower part of the neck joins the medial side of the shaft. The pectineus muscle is attached to the bone below the lesser trochanter.

The shaft of the bone, which is fairly uniform in caliber, nevertheless broadens slightly at its extremities. Bowing somewhat forward, its surface is smooth, except along the linea aspera, and it is covered by muscles. The almost circular cross section of the shaft is modified by a thickened ridge along its posterior aspect; the linea aspera. The linea aspera is especially prominent in the middle one-third of the bone, where it exhibits a lateral lip and medial lip. The lateral and medial lips diverge below and form the supracondylar ridges of the femur. Superiorly, the linea aspera is prolonged into two muscular impressions, (1) a line which runs medially and gives attachment to the vastus medial muscle; and (2) a rough lateral ridge, the gluteal tuberosity (sometimes replaced by a gluteal fossa) to which is attached part of the gluteus maximum and the upper part of the adductor musculature. The vastus intermedius is attached to the anterior and lateral surfaces of the shaft.

The shaft gradually widens toward its lower end and has a flattened triangular popliteal surface on its posterior aspect. The linea aspera continues below into two diverging lines that bound this surface and give attachment medially to the adductor magnus and laterally to the vastus lateralis and the short head of the biceps femoris.

The shaft of the femur is composed of a tube of cortical bone enclosing a medullary cavity. The ends of the femur are composed of cancellous bone covered by a thin layer of cortical bone. The structure of the femur shows an excellent adaption to the mechanical conditions existing at all points along bone. Its internal architecture appears to be determined by the requirements of mechanical laws which result in a maximum of strength with a minimum of material (Cowin, 1989; Hamilton, 1976; Schmid-Schonbein et al., 1985; Woodburne, 1983).

Two types of bone make up the femur: cortical bone and cancellous bone. Figure 1.3 shows the structure of a femoral bone. Cortical bone forms the dense protective shell (cortex) of the bone and envelops the central region containing cancellous bone. However, no distinct boundary exists between the two bone types. Cortical bone is organized by concentric haversian systems (osteons) and circumferential lamellae near its inner and outer surfaces. Within a lamellae, the collagen fibers are arranged roughly parallel to each other. In neighboring lamellae, the collagen fibers are in different orientations. As a result, cortical bone is stiff, strong, and brittle relative to cancellous bone. Conversely, cancellous bone consists of a network of fine, irregular trabeculae separated by interconnecting spaces containing bone marrow. In the load bearing femur, the role of the trabecular bone is to support and direct the load through the ends of the femur to the midshaft and down to the knee. Trabecular bone patterns show the progressive development of the trabeculae in the capital femoral ossification center and femoral neck. In the total hip replacement, the calcar (proximal-medial femoral neck) supports a femoral prosthesis to restore the joint functions. As a general observation, trabecular bone is oriented to provide maximum strength while utilizing minimum osseous material. The trabeculae are thicker and more

tightly meshed in regions of greater stresses. Also, the trabeculae orientation coincides, in general, with the principle stress directions of a femoral bone.

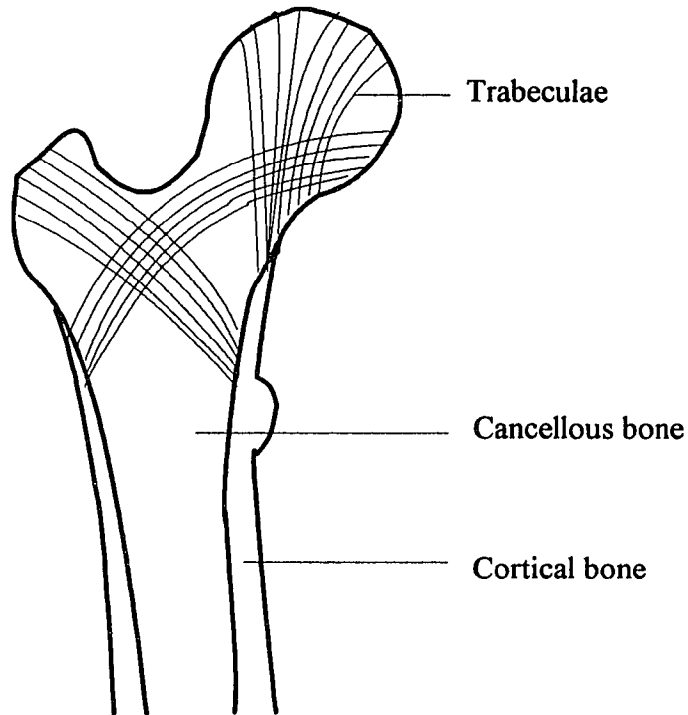


Figure 1.3 The structure of a femoral bone.

The general structure of cancellous bone may be approximated as an open-cell two-phase composite. One phase is bone while the other phase consists of blood, red and yellow marrow, nerve tissue, and miscellaneous cell tissue and fluid. Because of its calcified nature, bone can grow only by opposition. That is, bone can increase in size only by adding material to one of its surfaces through a process known as bone remodeling. New bone added to the sides of trabeculae is usually deposited in the form of fairly even lamellae. As new lamellae are added to the sides of trabeculae in a cancellous network, the spaces are correspondingly narrowed and filled. Accordingly, the continued deposition of fresh bone lamellae on trabeculae that enclose spaces soon affects the character of the bone in that it changes from a structure consisting of large spaces with little bone

(cancellous bone) to one of narrow spaces with much bone (compact bone). All bone is porous and the important structural feature that distinguishes cortical bone from cancellous is the quantity, size, shape and distribution of the cavities. The difference between these bone structures may be indicated by their apparent densities, i.e., their mass divided by their bulk volume. The most obvious difference between these two types of bone is their relative densities, or volume fractions of solids. Bone with a volume fraction of solids less than 70% is classified as cancellous; that over 70%, compact (Bogumill et al., 1984; Cowin, 1989; Mears, 1979; Revell, 1986).

1.3 Computed Tomography

During the past twenty years, computed tomography (CT) has obtained widespread acceptance as an important technique for the imaging of biological structures. Radiography is based on two-dimensional projection of tissue radiopacity, as obtained by recording the modulation of X rays penetrating the body. Due to the variance of absorption coefficients and spatial dimensions, different types of tissue and organs become visible and discernible as the projection of anatomical structures onto the film. Important volume information is lost in the projection, therefore reconstruction techniques, known as X-ray computed tomography, have been developed to generate true 2-D sectional views of single tissue layers from a multitude of projections. Successive sectional views can be combined to compute sectional views with various arbitrary orientations or even to generate 3-D image (Kline, 1988; Stark, 1987).

In CT, the image is not formed directly by the X-ray, but it is a multiple step process of scanning, data processing and graphical image reconstruction. Most CT systems contain three functional unit: scanning unit, computer and viewing unit. In addition, these systems contain one or more data storage devices with the ability to store the image data such as optical discs or magnetic tapes.

The basic principles of the simplest of CT systems, consisting of a finely collimated X-ray beam and single detector (Figure 1.4) will demonstrate. The attenuation of X-ray is measured between the source and detector. Then the source and detector are translated, defining another path through the body, parallel to the first. The process is repeated until the entire body section has been scanned. The internal structures of the body attenuate the X-ray beam according to their density, effective atomic number and thickness. At the end of this translation the source-detector assembly will return to its starting position, and the entire assembly will rotate and begin a second translation. During the second translation, the detector signal will again be proportional to the beam attenuation of anatomic structures, and a second detected intensity pattern will be described. If this process is repeated, a large number of intensity profiles will be generated. These intensity profiles are not displayed visually but are stored in numeric form in the computer. The computer processing of these data involves the effective superposition of each intensity profile to reconstruct the anatomic structures (Bushong, 1988; Weisberg et al., 1978).

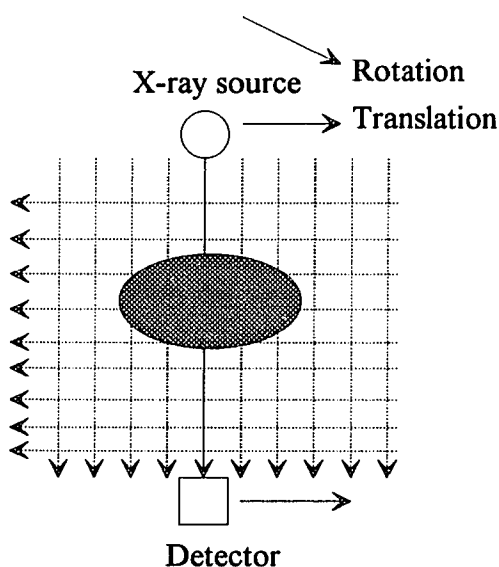


Figure 1.4 Principle of CT system with translating and rotating source-detector.

A digital computer within the CT system forms the CT image from the intensity profile data by a process which is generally referred to as image reconstruction. The image created by the computer is a numerical image with specific values for each "pixel" within the image. The computed pixels are arranged as rows and columns of a matrix. A typical matrix size is 512×512 pixels.

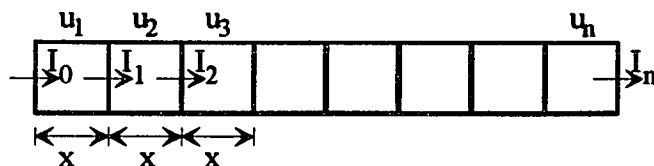


Figure 1.5 X-ray attenuation of the cross sectional pixels.

Image reconstruction begins with the resulting file generated by the CT scan. This file contains a large number of individual ray sums. The cross sectional layer of the body is divided into many elements or pixels. Each pixel is assigned a number proportional to the degree that the element attenuates the X-ray beam. The composition and thickness of the element, along with the intensity of the X-ray beam, determine the degree of attenuation.

In a cross section, the individual pixels can be viewed as a series of elements lined up end to end. The initial intensity (I_0) strikes the first pixel. The exit intensity (I_1) becomes the entrance intensity to the second, and so on. Figure 1.5 shows the X-ray attenuation in the cross sectional pixels. The equation progresses as follows:

$$I_1 = I_0 e^{-u_1 x_1} \quad (1.3)$$

$$I_2 = I_1 e^{-u_2 x_2} = (I_0 e^{-u_1 x_1}) e^{-u_2 x_2} = I_0 e^{-(u_1 x_1 + u_2 x_2)}$$

.

.

$$I_n = I_{(n-1)} e^{-u_n x_n}$$

For n elements, this equation can be written:

$$I_n = I_0 e^{-(u_1 x_1 + u_2 x_2 + \dots + u_n x_n)}$$

For a straight projection, $x_1=x_2=x_3\cdots$ the equation becomes

$$I_n = I_0 e^{-x(u_1+u_2+\cdots+u_n)}$$

Taking the log of both sides yields

$$\sum u = (u_1 + u_2 + \cdots + u_n) = \left(\frac{1}{x}\right) \ln\left(\frac{I_0}{I_n}\right) \quad (1.4)$$

If the incident intensity (I_0), projecting intensity (I_n) and element length (x) are known, the sum of the attenuation coefficients along the length can be calculated.

For a $n \times n$ square image, the linear equations can be expressed as follows:

For the translated detection (row examination)

$$\begin{aligned} a_{11}x_1 + a_{12}x_2 + \cdots + a_{1n}x_n + 0 + 0 + \cdots &= c_1 \\ 0 + \cdots + a_{21}x_{n+1} + a_{22}x_{n+2} + \cdots + a_{2n}x_{2n} + 0 + \cdots &= c_2 \\ . \\ . \\ 0 + \cdots + a_{n1}x_{n(n-1)+1} + a_{n2}x_{n(n-1)+2} + \cdots + a_{nn}x_{n^2} &= c_n \end{aligned}$$

For the rotated detection (column examination);

$$\begin{aligned} a_{11}x_1 + a_{21}x_{n+1} + \cdots + a_{n1}x_{n(n-1)+1} + 0 + 0 + \cdots &= c_{n+1} \\ a_{12}x_2 + a_{22}x_{n+2} + \cdots + a_{n2}x_{n(n-1)+2} + 0 + 0 + \cdots &= c_{n+2} \\ . \\ . \\ a_{1n}x_n + a_{2n}x_{2n} + \cdots + a_{nn}x_{n^2} + 0 + 0 + \cdots &= c_{2n} \end{aligned}$$

For the leading diagonal detection;

$$a_{11}x_2 + a_{22}x_{n+2} + a_{33}x_{2n+3} + \cdots + a_{nn}x_{n^2} = c_{2n+1}$$

.

.

In this case, a and x represent the ratio of the passing length to the pixel length in a pixel, and the X-ray attenuation in the cross sectional pixels. Where $a_{ij} = 1$ for a straight projection, and $a_{ij} \neq 1$ for an angle projection.

The matrix form of the system is $AX = B$, where A is a $n \times n$ matrix of coefficients. If there are $n \times n$ independent equations for $n \times n$ unknown values for u , the Gaussian elimination procedure can be applied to solve individual pixels.

The recent CT system records sets of reading in the form of a wide-fan beam. The X-ray tube circles around the body. As a result of having thousands of ray projections for a scan, thousands of equations can be solved simultaneously. The capabilities of the computer allow rapid calculations for individual values within the data matrix of attenuation values. Solving for individual pixels by these matrix algebra techniques will yield a cross sectional profile of pixel attenuation, corresponding to the density of the individual pixels, and thus a two-dimensional image of the object in the field at that slice position. In order to determine the linear attenuation coefficients of all of the pixels in an image matrix, several different algorithms are currently in use in an attempt to solve these equations as quickly and accurately as possible. These methods include back projection, filtered back projection, and the iterative technique.

A numerical value is calculated for each pixel within the image, referred to as CT numbers. The numbers are related to the attenuation coefficient values of the materials within the scanned body section. The linear attenuation coefficient is generally expressed as a decimal number. Because the human body is composed largely of water, an alternative way of presenting the data is with CT numbers. This is defined by comparing the attenuation coefficient of the tissue under consideration to that of water (Herman, 1980; Magid, 1985; Robertson, 1984).

$$\text{CT number} = \frac{[u(\text{tissue}) - u(\text{water})] \times k}{u(\text{water})} \quad (1.5)$$

In this case, k is a scale factor set to either 500 or 1000. Siemens CT scanner, Somatom DR, is used in this research and the scale factor is 1000 (Kline, 1988; Siemens Technical Information, 1978; Robertson, 1984).

A CT scanner is capable of recording variations in X-ray attenuation of as little as 0.5%. To view such small differences, independent control of picture brightness and contrast is provided. The brightness (usually called window level) selects the mid-gray range of attenuation around the mid-gray level corresponding to peak black and white. Typical CT number ranges for various tissues are shown in Table 1.1.

Table 1.1 Typical CT number for various tissues.

CT number scale	Tissue range	Typical CT number
+1000 to +300	Bone	Compact bone (≥ 1000) Cancellous Bone (800 to 1000)
+200 to -300	Soft tissue	Calcified tissue (600)
0	Water	Soft tissue (0 to 35)
-1000	Air	Air (-1000)

A CT scanner is primarily limited to provide two-dimensional axial cross-sectional views. However, gathering a number of parallel projections enables the construction of arbitrarily oriented sectional views by rearranging the pixel values. Furthermore, three-dimensional imaging is also feasible.

One of uses for CT data has been in the design of custom orthopedic implants. One of the problems with standard stock prostheses is that there is a potential for poor fit, resulting in subsequent prosthesis loosening, patient discomfort, or premature fatigue. In theory, a custom prosthesis designed to fit individual anatomy should be associated with better results. In the past, custom implants have fallen short of this goal due to the use of two radiographic images (anteroposterior and lateral) to model the three-dimensional geometry of the bone. CT has presently, allowed us to generate more accurate three-dimensional bone models.

Therefore, computed tomography is one of the best methods available at this time for performing non-invasive bone density and geometry measurement. CT is also able to

separately assess cortical and trabecular bone at the clinically important sites of osteoporosis. The high resolved consecutive cross-sectional images obtained by scanning the femur can be used for generating a three-dimensional finite element model of the femur.

1.4 Mechanical Properties Description in Femoral Bone

The study of the mechanical properties of bone has been an area of interest for investigators for many years. Most of these studies aim at the properties of bone which comprise the femora. In these studies, bone samples are tested either by mechanical methods or by ultrasonic measurements in order to determine their elastic properties.

Anisotropic materials, such as bone, exhibit different mechanical properties when tested in different directions. Complete characterization of anisotropic material requires properties to be applied in several different orientations. Ultrasonic testing offers some advantages over mechanical testing for determining the elastic properties of bone. Specifically, ultrasonic specimens can be smaller, with less complicated shape, which makes specimen fabrication easier. Moreover, several anisotropic properties can be measured from one specimen. Due to the inhomogeneity, anisotropy, and limited size of bone, both advantages are significant.

The anisotropy of the elastic and strength properties of bone has been demonstrated in uniaxial testing by number of experimenters (Ashman et al., 1984; Bensusan et al., 1983; Currey, 1988; Linde et al., 1991; Martens et al., 1983; Martin, 1991; Schaffler et al., 1988; Reilly et al., 1975; Rohl et al., 1991; Van Buskirk and Ashman, 1981; Yoon et al., 1976). Most authors agree that human bone is both anisotropic and heterogeneous, and several studies use experimental methods to characterize the degree of anisotropy and to determine the elastic properties of bone as a function of anatomical position. The main difficulty in such work is that the traditionally mechanical testing methods are difficult to

apply to bone tissue. Elastic moduli determined ultrasonically have been shown to compare well with those measured by mechanical testing techniques.

Van Buskirk and Ashman (1981), Ashman and co-workers (1984) and others used ultrasonic technique to determine the five elastic constants of cortical bone assuming a transversely isotropic material. Reilley and Bastein (1974) showed that cortical bone is an orthotropic material that is approximately transversely isotropic. These findings seem consistent with the observation that bone histologically displays the symmetry of a transversely isotropic material.

The choice of material symmetry for an elastic model of compact bone depends to a large extent on the intended application of the elastic model. For example, Huiskes (1984) indicates that the stress analysis of a human long bone is adequately served with an isotropic model. The data on the measured elastic constants of bone reported by Van Buskirk and Ashman (1983) show that the percentage difference between the orthotropic elastic constant values and the transversely isotropic constant values are quite small, and unlikely to have a significant effect on the stress analysis of bone.

The trabecular bone tissue is considered by most authors (Ashman et al., 1988; Bensusan et al., 1983; Linde et al., 1991; Martens et al., 1983; Martin, 1991; Rohl et al., 1991) as a nonhomogeneous, anisotropic, nonlinearly viscoelastic substance, and as such, its detailed properties are difficult. The ratio of vertical to lateral stiffness ranges up to a factor of ten in the proximal trabecular bone. Therefore, the anisotropy in stiffness can be considerable. The source of the anisotropy is obviously the trabecular morphology. The existence of a preferred direction of structure leads to the anisotropy. As a consequence, long bones are much less stiff in the lateral direction than along the long axis, not only because there is less material to resist the load but because the lateral deformation occurs more by bending of the resisting structures rather than by direct compression as appears to occur in the stiffest direction.

Some of the variables which determine bone material properties include porosity, mineralization, and density. The porosity may be determined as the fraction of a bone volume occupied by "void" filled with soft tissues e.g., Haversian canals or inter-trabecular marrow spaces. This is due to the fact that marrow and other soft tissues have little stiffness. It is reasonable to expect bone to lose strength and stiffness with increasing porosity. Stiffness goes from almost zero in sparse trabecular bone to about 15,000 MPa (1 MPa = 145 psi) in cortical bone. Given the difference between compact bone (porosity less than approximately 15%) and cancellous bone (porosity greater than approximately 70%) with respect to morphology and mechanical properties, some researchers regard these two types of lamellar bones as different materials in an engineering sense (Pugh et al., 1973).

Porosity distinguishes between void and solid matrix in bulk bone. Mineralization distinguishes between the mineral and organic components of the solid matrix, and is the mass fraction of the mineral. Curry and Burstein et al. (1975) have shown that the mechanical properties of bone are very sensitive to the degree of mineralization of the bone matrix, measured as the ratio of ash mass to dry mass. Many studies have shown linear or exponential increases in bone stiffness with increasing mineralization.

On the other hand, recent experiments suggest that bone's material strength is not related to mineralization in a strong, positive way (Currey, 1990). Some studies have even found negative correlation between mineralization and strength (Martin, 1990).

Mineralization is largely governed by the rates of bone remodeling, since newly made bone takes about six months to reach full mineralization. Mineralization can also be affected by defective calcification of osteoid (osteomalacia) or of growth cartilage in children. In these cases, the reduced mineralization is usually detrimental because the bones become too weak and compliant.

Density is expressed in terms of the mass per unit volume. "Apparent density", or "bulk density" is defined as the mass divided by the total volume of a region of bulk bone,

which includes Haversian canals, marrow spaces, and other voids. Hence, apparent density is a function of both the porosity and mineralization of the bone material. Carter and Hayes (1977) showed that the compressive strength (s^-) and elastic modulus (E) of bone specimens have

$$s^- = 68(\dot{\epsilon})^{0.06} \rho^2 \quad (\text{MPa}) \quad (1.6)$$

$$E = 3790(\dot{\epsilon})^{0.06} \rho^3 \quad (\text{MPa}) \quad (1.7)$$

which were correlated with the square and cube, respectively, of density in g/cm^3 ($\rho = 0.15$ to 1.9 g/cm^3). In these equations, $\dot{\epsilon}$ is strain rate in inverse seconds (s^{-1}). The relationship, (Equation 1.7), is called the combined data relationship because the data upon which it is based depend upon both bovine and human cancellous bone data and bovine and human cortical bone data. The inclusion of cortical bone as a datum in a relationship between cancellous bone and apparent density is based on the suggestion of Wolff that cortical (compact) bone is simply a more dense cancellous bone. The inclusion of the data has the advantage of giving a wider data base for determining a relationship between elastic modulus and apparent density.

The relationship between the axial elastic modulus and apparent density was also investigated by Rice et al. (1988). In this later analysis the distinction between bovine and human bone was maintained, and the data for cortical bone were not included. Under these conditions, it was found that the axial elastic modulus was proportional to the square rather than the cube of the apparent density. Furthermore the constants of proportionality between elastic modulus and apparent density differ for human and bovine cancellous bone. The analysis of Rice et al. employed the data considered by Carter and Hayes as well as the bovine cancellous data reported by Williams and Lewis (1982) and Bensusan et al. (1983). The data of other investigators were adjusted to the strain rate used by Carter and Hayes, using the dependence of modulus upon strain rate established by Carter and Hayes. As Equation 1.8 shows, the axial elastic modulus (E) is proportional to the strain rate to 0.06 power. Carter and Hayes conducted their compression test at a strain rate of

0.01 s⁻¹ while Bensusan et al. (1983) used a strain rate of 0.42 s⁻¹. It follows from Equation 1.7 that

$$\begin{aligned} E \text{ (at } 0.01 \text{ s}^{-1}\text{)} &= \left(\frac{0.01}{0.042}\right)^{0.06} E \text{ (at } 0.42 \text{ s}^{-1}\text{)} \\ &= 0.92E \text{ (at } 0.42 \text{ s}^{-1}\text{)} \end{aligned} \quad (1.8)$$

Hence, all the Bensusan et al. data were multiplied by 0.92 to convert them to a strain of 0.01 s⁻¹. The data of Williams and Lewis were adjusted in a similar way. Williams and Lewis used a strain rate of 0.005 s⁻¹.

Some investigators have estimated the mechanical properties from quantitative CT assessments. Garg and Walker (1986) used CT number to determine the elastic modulus for the tibial bone. It was decided to generate data experimentally for the bones under analysis. A knee was cut into 8 mm sagittal slices, from which as many 7 mm cubes as possible were cut, aligned with the principal trabecular orientation determined visually. The cube locations were superimposed on the CT number printouts and an average CT number was obtained. Load-deflection curves were obtained across each face of each cube, straining to 3% at approximately 1% strain s⁻¹. The modulus of elasticity was defined as the maximum slope on the load-deflection curves. Sixty-five cubes were tested and the data was plotted as E against CT number. For the region of 400 to 1000 (cortical bone), the relationship are

$$E = 3995 - 19.55 \times CT + 0.0255 \times (CT)^2 \quad (1.9)$$

Because of the different CT scale factor, this relationship can be applied only to the specific CT scans.

The second independent constant for an isotropic material, the Poisson's ratio, is the ratio of strain in a direction perpendicular to that of a uniaxial stress, to the strain in the direction of uniaxial stress. The reported values of Poisson's ratio in human compact and cancellous bone are difficult to compare due to specimen type, moisture, and strain rate during the relatively low number of experiments conducted for this purpose. Reilly and

Burstein (1974) tested a transversely isotropic model to determine five independent elastic constants for human compact bone tissue. The high values for Poisson's ratio reported by Reilly and Burstein (1974) have raised the question of whether the human compact bone is incompressible. Mahanian and Piziali (1985) who investigated the incompressibility for a transversely isotropic material in general and the human compact bone in particular, showed that the values reported by Reilly and Burstein are in the acceptable range, and below the incompressible limit.

It is generally accepted by many authors that the Poisson's ratio is related to some bone physical properties such as the level of moisture in the tested bone tissue, the microscopic architecture, the applied strain rate and more. However, no attempt has been found in the literature to correlate the Poisson's ratio of human compact or trabecular bone to any of these physical properties. Instead, experimental values of Poisson's ratio have been obtained for various types of bone tissues and topographic location in the long bone.

An empirical formula (Equation 1.7) developed by Carter and Hayes (1977) is used to determine the elastic modulus of the cortical bone from the mean CT number of each single element. Because the cancellous bone with a wide range density is more complicated than the cortical bone, the empirical relationship is not reliable for the cancellous bone. Therefore, except for the elastic modulus of the cortical bone, all other elastic properties are obtained from the literature (see Section 4.6).

1.5 Stress Analysis of the Femur with a Prosthesis

The total requirements of a finite element model of the femur with prosthesis are extensive. Bone is a living material that constantly reforms in response to the implanted material. This leads to changing boundary conditions at the bone-prosthesis interface which are difficult to model. Since the interface stresses are difficult to measure, the best way to calculate interface stresses is with the finite element method.

Stress calculations of the finite element method in the femur with prosthesis require a number of assumptions. These include the determination of the border between cortical and cancellous bone, the material properties and their distribution, and the loading conditions of a model. These assumptions influence the results considerably.

1.5.1 Finite Element Model

Svensson et al. (1977) created a two dimensional plane stress model which uses side plate elements (2D shell elements). The prosthetic stem was modelled with two elements across its width, the cement by one element and the bone by the other element. The total number of elements is 112. This subdivision is the minimum amount and not sufficiently fine to give good stress value. No shear stress in antero-posterior (A-P) direction can be assessed in this paper. The authors found that for Charnley prosthesis and in the situation where bonding exists and no loosening occurs it was not possible to alter the stem shape or cement properties to provide better stress fields in the metal/bone/cement complex.

A three-dimensional finite element model of an implanted femoral stem was developed by Hampton et al. (1980). The geometrically simplified model contained 31 elements and 200 nodes resulting in 600 degree of freedom and all materials were assumed to be isotropic, linear and homogeneous. Although the three dimensional mesh is probably the most advanced at that time, it still is not sufficiently accurate, since the authors could not simulate the real bone geometry. The authors used three orthogonal loads applied to the ball of the stem directed inferiorly, laterally and posteriorly. The resulting stress distributions indicated that the inferiorly directed load is responsible for most clinically observed failures.

Crowninshield et al. (1980) studied a symmetrical model with 400 hexahedral elements. They also tabulated the maximum tensile stresses in the stem found by different authors. These values differed greatly as such authors had made different assumptions. In a parametric study Huiskes (1982) used an axisymmetrical model consisting of 750 ring

elements with 1900 nodal points. He obtained a general fundamental basis for the load transfer from the implant to the bone. From this he derived simple formulae for assessing the influence of the geometries and material properties of the hip implant components on the stress.

Rohlmann et al. (1983) used the anteroposterior and lateral radiographs of a cadaveric femur to create the finite element model. The authors also used radiographs compared to the selected radiological density to determine the radiological density and bone density. A stepped wedge of aluminum served as a quantitative standard of density. This minimizes the influence of varying conditions during radiography. The authors tried to simulate more accurate bone geometry and bone properties. In this report, the authors also applied strain gauges to the cadaveric femoral surface measuring the femoral surface stresses. They had established the qualitative investigations of the stresses in the femur-prosthesis.

Brown et al. (1988) applied computed tomography (CT) to obtain transverse section images. They used the transverse section images to construct a three dimensional finite element model. The source CT scans came from the femur of a normal male cadaver, into which a plastic replica of a HD-type femoral component had been conventionally implanted using acrylic cement. They did not simulate the greater trochanter and the more accurate material properties in the finite element model. The three dimensional finite element mesh contained 867 nodes (2601 degree of freedom) which were connected to form 768 linear elastic elements. In this paper, the authors mainly investigated the stress effect with the formation and proliferation of a compliant fibrous membrane at the bone/cement interface. They found progressive decay of border zone stiffness, a thin zone bordering the cement, and a production of complex changes in load transmission. Foremost this was a generalized increase in stress levels in the proximo-lateral cancellous bone, and a corresponding generalized decrease in stress levels in the proximo-medial cancellous bone.

Rohlman et al. (1988) used a geometrically simplified finite element model to investigate load transfer between a porous hip endoprosthesis and a femur. This research indicated that maximum values for relative motion in the interface between bone and implant occurred for implants with the same elastic modulus as compact bone. They also found that the elastic modulus of the porous coating had only a small influence on bone stress. Huiskes et al. (1989) used a two dimensional simplified finite element model for the cemented femur-prosthesis to determine optimal prosthetic designs which minimize interface stress. Their results showed that 30 to 70% cement and interface stress reductions could be obtained in principle with an optimized design. They applied the finite element method for mathematical shape optimization of prosthetic design in general, using the femoral hip stem as an example.

Harrigan et al. (1992) used the radiographs of an intact human cadaver femur in which an HD-2 total hip prosthesis had been cemented to create a three dimensional finite element model. The material properties of the finite element model were taken from the published literature data and found to be linearly isotropic. The elastic modulus of the prosthesis was 200,000 MPa (1 MPa = 145 psi); the cement elastic modulus used was 2,800 MPa, the cancellous bone elastic modulus was 1,000 MPa, and the cortical bone elastic modulus was 16,000 MPa. Poisson's ratio was taken as 0.3. This model of a cemented femoral component showed three likely initiating events in the failure of cemented total hip femoral components; (1) debonding between the prosthesis and the cement in the proximal antero-medial region due to the peak loads during stair climbing; (2) crack initiation at the surface of a void or bubble in cement at the proximal postero-medial corner of the implant during stair climbing; (3) crack initiation at the surface of voids less than 5 mm between the prosthesis tip in both gait and stair climbing. The possibility of crack initiation at the cement-bone interface was not studied.

Cheal et al. (1992) created a three dimensional finite element model of an intact femur using the digitized data of the bone cross sections. The authors used 20-node

quadratic solid element for a total of approximately 3,700 nodal points and 1,000 elements. The linear heterogeneous isotropic material properties were assumed for the bone using the published data. The elastic modulus of the prosthesis was taken to be 234,000 MPa; the cement elastic modulus used was 3,000 MPa, the cancellous bone elastic modulus was 600 MPa, and the cortical bone elastic modulus was 17,500 MPa. Poisson's ratios for prosthesis, cement and cortical bone were taken as 0.3 and 0.205 for cancellous bone. A wide range of loading conditions were applied on the finite element model of a femur with a conventional straight-stem endoprosthesis. The authors tried to establish the role of loads and prosthesis material properties on the mechanics of the proximal femur after total hip arthroplasty.

Weinans et al. (1993) combined the stress patterns of a finite element model in a dog with the adaptive bone-remodeling theory developed by Huiskes et al. (1987) to predict patterns of bone remodeling. In this work, the enlarged contact radiographs of the bone cross sectional slices and the longitudinal radiographs from a lateral-posterior view of one dog were used to create a finite element model. Three-dimensional orientations of the slices were determined by the longitudinal radiographs and the contact radiographs of the bone cross sections were digitized. In the adaptive bone-remodeling theory (Huiskes et al., 1987), the hypothetical adaptive remodeling process can be further explained. A bone is loaded by external forces which result in internal loads and deformations, represented by stresses and strains. These stresses or strains can be considered to be local mechanical stimuli that can be sensed by the bone. If the stimulus is abnormal, due to altered loading patterns or placement of a prosthesis, the mechanical signal is transduced to a biochemical one and subsequently integrated with several other factors to cause a remodeling potential. The potential will affect the turn-over rate of the bone by activating osteoblasts or osteoclasts. This will result in adaptation of the geometry and the density. As a result, the stresses and strains in the bone will change as well, affecting the remodeling potential again. This process will continue until the mechanical stimulus is normalized.

Weinans et al. (1993) used the mathematical description of the adaptive bone-remodeling theory to relate the input (the stresses and strains) to the output (the net loss or gain of bone). The simulation results of the adaptive bone-remodeling process were compared with cross sectional measurements of the canine femurs after 2 years of follow-up. The comparison showed that long-term changes in the morphology of bone around femoral components of total hip replacements can be explained with the adaptive bone-remodeling theory. This work provides information concerning the relationship between bone remodeling and stress patterns. The prosthetic designs can be optimized to produce as little bone loss as possible according to the adaptive bone-remodeling theory.

Besides investigations concerning the stress analysis of the femur with prosthetic hip stem, a number of finite element analyses of the bones have been designed for problems of fracture and fracture fixation (Simon et al., 1977; Beaudoin et al., 1989; Mihalko et al., 1992). The main objective of the finite element method in orthopedic biomechanics is to provide information and evaluation for artificial joint design and fixation.

1.5.2 Loading Patterns

The load conditions are important variables for finite element stress analysis. Each particular loading system leads to different stress patterns, and may result in different outcomes. External measurements have been made on patients (Andrews et al., 1972; Andriacchi et al., 1979) from which the magnitudes of internal forces have been inferred. This approach to the determination of the joint-contact forces and forces in other structures acting across the joint (muscles, ligament, and so on) is obviously attractive because it is non-invasive and is easy to apply during a broad array of activities of the patient.

The major difficulty in determining the joint force and muscle force is the indeterminate nature of the muscular force distribution. Because of the large number of loading-carrying elements that act across the joint, it is not possible to calculate the muscle

and joint-contact forces directly (Crowninshield et al. 1981). McLeish and Charnley (1970) grouped the involved muscles on the basis of electromyography and other information, and they estimated the joint-contact force in the hip to be approximately two times the body weight of a person; in contrast, Williams and Svensson (1968) estimated it to be approximately six times body weight during single-limb stance. Paul (1965) predicted that the peak joint-contact force in the hip for normal subjects during gait is approximately 3.5 to 6 times body weight, depending on strike length and speed.

The first attempt at direct measurement of the forces across the joint was reported in 1966 by Rydell, who inserted Austin Moore prostheses that had been instrumented with strain-gauges. Six months after implantation, access was gained to subcutaneous leads to the strain-gauges, and measurements of force were obtained. The contact forces during gait had peak values of three times of a body weight. Similar values were obtained by English et al. (1979) with a telemeterized hip prosthesis.

Davy et al. (1988) used a triaxial telemeterized total hip prosthesis to obtain the data on the forces acting across a total hip prosthesis in vivo in one patient. These data were obtained several times and during several activities during the first thirty-one postoperative days. They found that the magnitude of the joint-contact force during double limb stance was 1.0 times body weight. During ipsilateral single-limb stance the joint-contact force was 2.1 times body weight, and during the stance phase of gait the peak force typically was 2.6 to 2.8 times body weight, with the resultant force located on the anterosuperior portion of the ball. During stair-climbing, the force was 2.6 times body weight. At peak loads, the angle between the resultant force and the axis of the femoral neck was 30 to 35 degrees and that between the resultant force and the plane of the prosthesis was 20 degrees. During stair-climbing or straight-leg raising, the out-of-plane orientation of the resultant force increased substantially.

Burke et al. (1990) also used the telemeterized total hip prosthesis in experimental studies to measure the magnitude and orientation of loads. In order to simulate the

midstance of gait, the femur was measured as in neutral rotation and in 12° of adduction, with the prosthesis inserted in neutral varus-valgus and 15° of anteversion. The loading conditions for one-legged stance simulated the experimental loading conditions for strain measurement. A 100 lb spinal load was applied to the loading fixture for strain measurement. This corresponds to the load applied by a person weighing approximately 125 lbs, because the weight of the supporting leg is subtracted from body weight to arrive at the spinal load. The load on the head of the prosthesis was 1,460 N (328 lbf) and was approximately 2.6 times body weight. The greater trochanter load of 880 N (180 lbf) was tensile and applied 15 degrees medial to the vertical. The loading condition (Burke et al., 1990) is selected in this research due to the loading condition which includes the joint contact force and muscle force regarded as reasonable estimations during gait (see Section 4.7).

These measured data provide information concerning the forces that are sustained by prosthetic hip joints during a number of common activities of daily living. However, the complex loading conditions, together with the geometry and material properties of finite element model, can provide a meaningful basis for stress analysis and prosthetic design in general.

1.6 Objectives

The production of accurate bone models from preoperative CT scans may provide a means of better surgical planning of complex total joint replacement and a more precise method of manufacturing customized implants for problem cases. The CT images can also help the clinician to obtain an optimum selection of the hip implant in a specific case. Because three dimensional images may be made of the medulary canal of any long bone, customized manufacture of stemmed prostheses may be simplified and can be more accurate than those made from measurements taken from plain radiographs.

CT cross sectional images of a bone provides bone shape (geometry) and bone property information. This can be used to develop a three dimensional shape (geometrical) display of the bone which can be subdivided into finite elements. The internal forces in the bone, stresses, can then be calculated and studied. The three dimensional biomechanical finite element studies applied to the reconstructed bone images can then help to predict and analyze the outcome of hip and knee replacement surgery. The detailed understanding of the three dimensional stress patterns may help to decrease the mechanical failure rate of joint replacement. Previous studies have shown that stress analysis for hip implants have given some clues to the causes of stress patterns that could predispose to loosening of the implant.

Several kinds of biological and mechanical phenomena may contribute to increased failure rates of a bone-prosthesis composite; they include infections, component fracture, excessive wear, bone resorption, and aseptic (noninfectious) loosening. The latter is considered to be the most important complication, limiting the life span of hip implants. Normal bone is continuously remodeling due to stresses. Hence, the implant-bone interface is not a static physical entity, but changes its characteristics over time. This process may be influenced by interface stress or strain patterns, in the same way that normal, intact bone is able to adapt its structure and shape to an altered loading environment.

These biological and mechanical stimuli may act to reduce the strength of the implant-bone interface in cemented and cementless prostheses alike, if only locally. High interface stresses may provoke interface loosening. Once local failure is initiated, failure propagation may occur, introducing (micro) motions of the implant relative to bone. It is quite probable that these (micro) motions and particulate debris provoke bone resorption and the progressive development of the fibrous tissue membrane seen in radiological loosening.

Therefore, it would be useful to have an understanding of the stress patterns of the femur with prosthesis. The CT finite element method has the potential to be a useful tool to calculate and analyze the stress patterns of the femur with prosthesis.

The developed analysis method has established a procedure including the following specific steps:

1. Use CT to scan femoral cross sections.
2. Translate the scanned cross sectional images and reconstruct the original image.
3. Develop a data base structure to store and manipulate the image.
4. Develop the edge detection method to localize bone from CT scan.
5. Calculate the geometrical center of each cross section and simulate the bone prosthesis according to the canal size of the scanned bone and manufacture's prosthesis templates.
6. Develop the node selection method to determine the node positions of the scanned bone and prosthesis.
7. Generate three dimensional finite meshes from cross sectional images.
8. Calculate the elastic modulus of each element from the CT number and assign the material elastic properties to the three dimensional elements.
9. Create an input data file for ANSYS finite element program to calculate the stress patterns.
10. Analyze the stress patterns of the femur with prosthesis structure.
11. Establish a CAD/CAM procedure to create plastic bone model in Stereolithography Apparatus (SLA).

This computer aided analysis method then provides a semi-automatic, noninvasive procedure for modeling of the femur with prosthesis and finite element stress analysis.

CHAPTER 2

THEORETICAL APPROACH

2.1 Introduction

The stress analysis of the femur with a prosthesis, in the most general sense, involves the combination of the tension, compression, bending and torsion. In this chapter, the relationship between bone and the science of mechanics is introduced, then the basic stress and strain are defined. Finally the cylindrical shaft is used as the bone model to explain various load conditions and to prove the validity of the finite element method.

The discipline of mechanics is the physical science that deals with the effects of forces and moments on the deformation of an object. The concern here is with the mechanics of deformable objects, in particular, bone. Bones are physical objects in that they obey the laws of mechanics. The primary law of mechanics which concern deformable objects is the law of elasticity of solid materials and Newton's law.

Hooke's law states that there is a linear relation between the force and deformation of a solid object. The laws of Newton and Hooke form the foundation of the mechanics of elastic objects. The biomechanical behavior of bone in normal physiological situations is quite similar to the mechanical behavior of an elastic object (Cowin, 1989; Ducheyne and Hastings, 1984; Schmid-Schonbein et al., 1985).

2.2 Stress and Strain

2.2.1 Definitions

When a body is subject to loading, it deforms. The molecules resist deformation through mutual bonds that generate internal loads. In solid mechanics, which studies this deformational behavior under loading, the local deformations are represented by strain; the internal loads are represented by stress. In the analyses of these phenomena in structures,

the principles of continuum theory are usually applied. Although the materials out of which a structure is made are not truly continuous at a molecular or even a microscopic level, the mechanical behavior of structures can usually be described and predicted with methods that neglect discontinuities on a smaller scale. Within the frame of continuum theory, materials are regarded as indefinitely divisible and thus variables as stresses and strains can be defined at an indefinitely small point. This assumption of material continuity is sometimes quite adequate, as in metals, and at other times rather inaccurate, as for instance, in trabecular bone.

To define the stress state in a point of a structure, an arbitrary point in plane is chosen. On this plane a certain internal load, divided by the plane area, represents a certain amount of stress (σ). The stress can be decomposed into a component normal to the plane (σ_n , called direct stress) and one parallel to the plane (τ , called shear stress). A three-dimensional stress state is characterized by six values: the magnitudes of three direct-stress and three shear stress components. The stress components can be assembled in the following matrix form, wherein each row represents the group of stresses acting on a plane passing through $P(x, y, z)$:

$$T = \begin{bmatrix} \sigma_x & \tau_{xy} & \tau_{xz} \\ \tau_{yx} & \sigma_y & \tau_{yz} \\ \tau_{zx} & \tau_{zy} & \sigma_z \end{bmatrix} \text{ or } T = \sigma_{ij}, i=1, 3; j=1, 3$$

In this stress matrix, it can be proven that $\tau_{xy} = \tau_{yx}$, $\tau_{xz} = \tau_{zx}$, and $\tau_{yz} = \tau_{zy}$ by the equilibrium conditions of an element. Hence, the stress state in the point concerned is fully characterized by six independent variables, three normal and three shear stress components.

Strain is fundamentally a different physical quantity and a non-dimensional measure of geometric change, while stress is a measure of force per unit area. Normal and shearing strain are concepts similar to normal and shear stress. The strains can be defined with

respect to an infinitesimal small cube, such as a geometric point. There are two types of strain: normal strain (ϵ), describing the relative changes in length of the cube faces, and shear strain (γ) describing the angular distortion.

The state of stress is described by a nine-term array, thus the strain tensor is denoted by ϵ_{ij} :

$$\epsilon_{ij} = \begin{vmatrix} \epsilon_x & \frac{1}{2}\gamma_{xy} & \frac{1}{2}\gamma_{xz} \\ \frac{1}{2}\gamma_{yx} & \epsilon_y & \frac{1}{2}\gamma_{yz} \\ \frac{1}{2}\gamma_{zx} & \frac{1}{2}\gamma_{zy} & \epsilon_z \end{vmatrix} \quad i = 1, 3; j = 1, 3$$

2.2.2 Stress-Strain Relations

The elastic characteristics of bone are a description of the response of the tissue to a mechanical stress incurred as it performs its structural functions. The response of the tissue in the region of elastic tissue behavior to external loads, that is, the relation between deformations and stresses, is characterized by the elastic constants of the bone tissue. This relation is known as Hooke's law and may be presented in tensor notation as (Borg, 1963; Cowin, 1989; Eisenberg, 1980; Ugural and Fenster, 1982):

$$\tau_{ij} = C_{ijkl} \epsilon_{kl} \quad \text{where: } i, j, k, l = 1, 2, 3$$

If the properties are different in every direction, the material is called "anisotropic" and has 36 elastic constants in the elasticity tensor. If the material is isotropic in two out of the three directions, then it is "orthotropic" and has 9 independent elastic constants. If, however, there is one plane in which the elastic properties are the same in every direction on the plane, the material is said to be "transversely isotropic" and has 5 elastic constants. If there is no directional independence of the elastic properties, the material is called "isotropic" and has only two elastic constants which are referred to as the modulus of elasticity and Poisson's Ratio. Physically, the elastic modulus is the ratio between stress

and strain, and Poisson's Ratio (ν) is defined as the negative of the ratio of transverse strain to longitudinal strain in the direction of uniaxial loading. The following equation represents a rather widely used expression for Hooke's law for orthotropic material.

$$\begin{bmatrix} \tau_{xx} \\ \tau_{yy} \\ \tau_{zz} \\ \tau_{xy} \\ \tau_{yz} \\ \tau_{zx} \end{bmatrix} = \begin{bmatrix} C_{11} & C_{12} & C_{13} & 0 & 0 & 0 \\ C_{21} & C_{22} & C_{23} & 0 & 0 & 0 \\ C_{31} & C_{32} & C_{33} & 0 & 0 & 0 \\ 0 & 0 & 0 & C_{44} & 0 & 0 \\ 0 & 0 & 0 & 0 & C_{55} & 0 \\ 0 & 0 & 0 & 0 & 0 & C_{66} \end{bmatrix} \times \begin{bmatrix} \epsilon_{xx} \\ \epsilon_{yy} \\ \epsilon_{zz} \\ \gamma_{xy} \\ \gamma_{yz} \\ \gamma_{zx} \end{bmatrix}$$

where

$$\begin{aligned} C_{11} &= \frac{1 - \nu_{yz}\nu_{zx}}{\epsilon_y\epsilon_z\Delta}, \quad C_{12} = \frac{\nu_{yx} + \nu_{zx}\nu_{yz}}{\epsilon_y\epsilon_z\Delta} = \frac{\nu_{xy} + \nu_{zy}\nu_{xz}}{\epsilon_x\epsilon_z\Delta} \\ C_{22} &= \frac{1 - \nu_{xz}\nu_{zx}}{\epsilon_x\epsilon_z\Delta}, \quad C_{13} = \frac{\nu_{zx} + \nu_{yx}\nu_{zy}}{\epsilon_y\epsilon_z\Delta} = \frac{\nu_{xz} + \nu_{xy}\nu_{yz}}{\epsilon_x\epsilon_y\Delta} \\ C_{33} &= \frac{1 - \nu_{xy}\nu_{yx}}{\epsilon_x\epsilon_y\Delta}, \quad C_{23} = \frac{\nu_{yz} + \nu_{yx}\nu_{xz}}{\epsilon_x\epsilon_y\Delta} = \frac{\nu_{yz} + \nu_{yx}\nu_{zx}}{\epsilon_x\epsilon_y\Delta} \\ C_{44} &= G_{yz}, \quad C_{55} = G_{zx}, \quad C_{66} = G_{xy} \\ \Delta &= \frac{1 - \nu_{xy}\nu_{yx} - \nu_{yz}\nu_{zy} - \nu_{zx}\nu_{xz} - 2\nu_{yx}\nu_{zy}\nu_{xz}}{\epsilon_x\epsilon_y\epsilon_z} \end{aligned}$$

For transverse isotropy, there are only five distinct elastic constants and they are obtained from the nine distinct orthotropic elastic constants by imposing the following restrictions:

$$\epsilon_x = \epsilon_y, \quad \nu_{xy} = \nu_{yx}, \quad \nu_{zx} = \nu_{zy}, \quad G_{yz} = G_{zx}$$

$$G_{xy} = \frac{\epsilon_x}{2(1 - \nu_{xy})}$$

The isotropic elastic constants can be obtained from the orthotropic elastic constants by imposing the following restrictions:

$$\varepsilon_x = \varepsilon_y = \varepsilon_z = \varepsilon \quad G_{xy} = G_{xz} = G_{yz} = G = \frac{E}{2(1 + \nu)}$$

$$\nu_{xy} = \nu_{yx} = \nu_{xz} = \nu_{zx} = \nu_{yz} = \nu_{zy} = \nu$$

The cancellous bone and cortical bone are considered by most authors as anisotropic and orthotropic materials respectively (see Section 1.4). Linear isotropy is assumed for the femoral bone in this research due to the limitation of the finite element program and computer (see Section 4.4.6).

2.3 Stress in a Cylindrical Shaft

The purpose of this subsection is to consider an elementary stress analysis occurring in a cylinder shaft when it is subject to various types of loading. A Cartesian basis x, y, z is selected so that its origin is located at the centroid of the transverse cross-sectional area and thus, the x is coincident with the long axis of the cylinder. The base vectors y and z are taken to be coincident with the principal axes of the area moment of inertia of the transverse cross section of the shaft. The area moments of inertia are denoted by, I_{yy} and I_{zz} , and the cross-sectional area by A . If the cylindrical shaft is subject to a force (F) in the x direction only, the stress component is:

$$\sigma_x = \frac{F}{A} \quad (2.1)$$

Form Hooke's law, the strain components are

$$\varepsilon_x = \frac{\sigma_x}{E} = \frac{F}{AE} \quad (2.2)$$

$$\varepsilon_y = -\frac{\nu F}{AE}, \quad \varepsilon_z = -\frac{\nu F}{AE} \quad (2.3)$$

$$\gamma_{xy} = \gamma_{yz} = \gamma_{zx} = 0$$

The deformations of the structure in x, y , and z coordinate system include the following:

$$u = \frac{F_x x}{A_z E}, \quad v = -\frac{\nu F_x y}{A_z E}, \quad w = -\frac{\nu F_x z}{A_z E} \quad (2.4)$$

When a shaft is bent by a couple M_z , the shaft is understood to be under simple bending. From experimental evidence, it is known that the stress value at a given point with distance y from the neutral line is:

$$\sigma_x = \frac{M_z y}{I_z} \quad (2.5)$$

$$\sigma_y = \sigma_z = \tau_{xy} = \tau_{yz} = \tau_{zx} = 0$$

where I_z is the moment of inertia of the cross section the cylindrical shaft about the z axis.

From Hooke's law, the strain components are

$$\epsilon_x = \frac{\alpha}{E}, \epsilon_y = \epsilon_z = -\frac{\nu \alpha}{E} \quad (2.6)$$

$$\gamma_{xy} = \gamma_{yz} = \gamma_{zx} = 0$$

The deformations of the shaft in x , y , and z coordinate system include the following:

$$u = \frac{M_z y x}{E I_z}, \quad v = -\frac{M_z x^2}{2 E I_z} - \frac{\nu M_z y^2}{2 E I_z} + \frac{\nu M_z z^2}{2 E I_z}, \quad w = -\frac{\nu M_z y z}{E I_z} \quad (2.7)$$

Consider the situation in which the shaft is subject to a twisting torque about z axis. The applied torque is M_T , and the length of the shaft is along the z axis. For a circular cross section, the shear stresses are

$$\tau_{zx} = -G\theta y = \frac{M_T}{I_p} y, \quad \tau_{yz} = G\theta x = \frac{M_T}{I_p} x \quad (2.8)$$

where G = shear modulus of elasticity

θ = twist per unit length

I_p = the polar moment of inertia of the circular cross section

The resulting shearing stress at any point (x, y) is:

$$\tau = \sqrt{\tau_{zx}^2 + \tau_{yz}^2} = \frac{M_T}{I_p} \sqrt{x^2 + y^2} = \frac{M_T}{I_p} r \quad (2.9)$$

Therefore, the value will be a maximum at the outside fiber, where r is a maximum. The warping is zero for the circular cross section. This represents a rigid body movement of the entire shaft, not a distortion of the cross section.

For the elliptical cross section:

the shearing stresses at any point in the elliptical cross section are

$$\tau_{zx} = -\frac{2M_T y}{\pi a b^3}, \quad \tau_{yz} = -\frac{2M_T x}{\pi a^3 b} \quad (2.10)$$

The resultant shearing stress at any point (x, y) is:

$$\tau = \sqrt{\tau_{zx}^2 + \tau_{yz}^2} = \frac{2M_T}{\pi a b} \sqrt{\frac{x^2}{a^4} + \frac{y^2}{b^4}} \quad (2.11)$$

The τ_{\max} occurs at the extremity of the minor axis, and $\tau_{\max} = \frac{2M_T}{\pi a b^2}$.

The warping function $w(x, y) = \frac{M_T(b^2 - a^2)xy}{\pi a^3 b^3 G}$

The closed-form solutions are listed as the above formulas for the various types of loading. Loading of slender bodies (as bars and beams) by axial forces, transverse forces, and bending moments results in axial direct stresses, normal to the cross sections. Although transverse forces generate shear stresses as well, the axial direct stresses are usually the most significant ones where chances for failure are concerned. If these loading cases occur in combination, then the stresses in the structure are found by superimposing the stresses as they would result from each loading case individually. This is an important principle in stress analysis (Fung, 1981; Schmid-Schonbein et al., 1985).

Assume a femur loaded by hip joint force and abductor force with a particular cross section. A free body diagram of the femur is developed and the internal loading configuration in the section is determined using equilibrium conditions (Figure 2.1). Generally, it consists of three moments (two bending moments and a torque), an axial force and two transverse forces (Cowin, 1989; Ducheyne and Hastings, 1984; Schmid-Schonbein et al., 1985). The concern here is the axial direct stress. Only the bending moments and the axial force produce axial direct stresses. The femoral shaft is assumed to behave as a linearly elastic, isotropic, and homogeneous 3-D beam. The cross section is treated as if it were a part of a shaft, the only difference being that the cross sectional

shape is irregular. To apply the formula of beam theory, the following values must be evaluated: (1) The cross sectional area, (2) The center of gravity location, (3) The principal inertia axes' orientations (α) with respect to the global (x-y) coordinate system, (4) The static moment of inertia. The evaluation of these parameters can be completed by digitizing the cross sectional shape and applying the appropriate formulas.

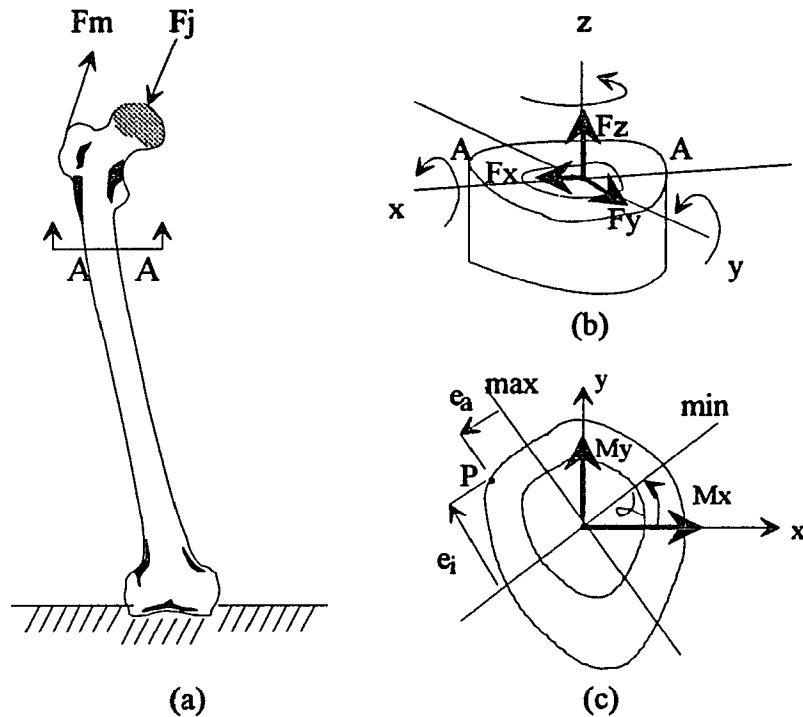


Figure 2.1 (a) External loads acting at the femur. (b) 3-D internal loads in a cross section of a femoral diaphysis. (c) The orientations of the bending moments with respect to the principal inertia axes are shown.

The axial direct stresses (σ_z) are then calculated by superimposing the individual contributions of the axial force and the two bending moments, applying the elastic formulas. Assume an arbitrary point P in the section (Figure 2.1). The stress in that point resulting from the axial force (in fact in the whole section, since the stresses as resulting from this force are uniformly distributed) is

$$\sigma_z = \frac{-F_z}{A} \quad (\text{compression is negative})$$

To calculate the stresses resulting from the bending moments, M_x and M_y , these loads must be decomposed in components around the principal inertia axes:

$$M_{\max} = M_y \cos \alpha - M_x \sin \alpha$$

$$M_{\min} = M_y \sin \alpha - M_x \cos \alpha$$

For the contribution to the stress at point P we find:

$$\sigma_z = \frac{M_{\max} e_a}{I_{\max}} + \frac{M_{\min} e_i}{I_{\min}}$$

where e_a and e_i are the distance from maximum and minimum principal axis.

Superimposing the contributions of the axial force and the bending moments gives:

$$\sigma_z = -\frac{F_z}{A} + \frac{e_a}{I_{\max}}(M_y \cos \alpha - M_x \sin \alpha) + \frac{e_i}{I_{\min}}(M_y \sin \alpha + M_x \cos \alpha) \quad (2.12)$$

The normal stress of longitudinal axis (z axis) of an arbitrary point in the femoral cross section can be expressed by the above formula.

Because of the complicated geometry of the femur, it is very difficult to calculate stresses by the 3-D beam theory and execution of theoretical analysis. Therefore, the finite element method provides the efficient tools to calculate stress patterns for irregular structures as femur and femur-prosthesis structure.

2.4 Finite Element Method

The development of the finite element method as an analysis tool was essentially initiated with the advent of electronic digital computer. In the numerical solution of a continuum problem it is necessary to establish and solve a system of algebraic equations. Therefore, a very important phase of a finite element analysis is the calculation of the finite element matrices.

The matrix displacement method of analysis based upon finite element idealization is employed throughout the ANSYS software. In the finite element displacement method, the displacement equations selected must satisfy the displacement boundary conditions, and the elements are assumed to be interconnected at a discrete number of nodal points situated on their boundaries. The displacements of these nodal points are taken as the basic unknown and the displacement field is defined in terms of these discrete variables. Once the discrete displacements are known, the strains are evaluated from the strain-displacement relations and, finally, the stresses are determined from the stress-strain relations. The general procedures involved in the finite element analysis are as follows (ANSYS User's Manual, 1990; Cook, 1981; Gallagher et al., 1982; Reddy, 1984):

1. Discretization of the given domain into a collection of preselected finite elements, i.e. selection of elements interconnected at certain nodal points.
2. Derivation of element equations for all typical elements in the mesh, i.e. evaluation of element stiffness and nodal force matrices.
3. Assembly of element equations to obtain the equations of the whole problem, i.e. assemblage of the stiffness and force matrices for the system of elements and nodes.
4. Imposition of the boundary conditions of the problem.
5. Solution of the assembled equations.
6. Postprocessing of the results, i.e. calculation of strains and stresses based on the nodal displacements.

ANSYS finite element program is developed using finite element method employing matrix displacement technique based on the energy principle. According to the principle of virtual work,

$$\delta U = \delta V \quad (2.13)$$

Here δU is the first variation of total strain energy (internal work) given by

$$\delta U = \int_V \delta \epsilon^T \sigma dv \quad (2.14)$$

and δV is the first variation of total potential energy (external work) given by

$$\delta V = (\delta u)^T F + \int_v \delta u^T b dv + \int_A \delta u^T s dA \quad (2.15)$$

Where u , F , b and s are nodal displacement, external force, body force and surface traction vectors, respectively. u^T , v and A represent the transpose of the u vector matrix, volume of element and area of element.

Substituting equations (2.14) and (2.15) into equation (2.13), one obtains the following equilibrium equations (see Appendix B).

$$Ku + f = F \quad (2.16)$$

Where K is an element stiffness matrix given by

$$K = \int_v B^T DB dv \quad (2.17)$$

Here B and D are a strain shape function and a material property matrix, respectively. f is a nodal element force vector given by

$$f = - \int_v N^T b dv - \int_A N^T s dA - \int_v B^T D \epsilon_0 dv + \int_v B^T \sigma_0 dv \quad (2.18)$$

Here N , ϵ_0 and σ_0 represent the displacement shape function, the self-strain vector, and the initial stress vector respectively. Equation (2.16) can be rewritten in partitioned matrix form:

$$\begin{bmatrix} K_{ii} & K_{ib} \\ K_{bi} & K_{bb} \end{bmatrix} \begin{bmatrix} u_i \\ u_b \end{bmatrix} = \begin{bmatrix} F_i \\ F_b \end{bmatrix} - \begin{bmatrix} f_i \\ f_b \end{bmatrix} \quad (2.19)$$

The subscripts i and b are used to refer the degrees of freedom that are free and imposed displacements, respectively. The first part of equation (2.19) may be solved for basic unknowns $\{u_i\}$.

$$\{u_i\} = -[K_{ii}]^{-1} [K_{ib}] \{u_b\} + [K_{ii}]^{-1} \{R_i\} \quad (2.20)$$

where $R = F - f$

The main portion of this solution procedure is to calculate the inverse of the stiffness matrix K . Although the Gaussian elimination procedure is a popular technique for this purpose, the total stiffness matrix is assembled before performing this procedure. Thus,

the back-up storage for the total unreduced stiffness matrix is inevitable. From a view point of storage manipulation, this technique is not efficient. ANSYS uses a more memory efficient technique; known as the wave front direct iteration solution method. This method deals with the only related stiffness matrices that are actually required to eliminate a specific degree of freedom and then it condenses out that degree of freedom (ANSYS User's Manual, 1990; Cook, 1981).

The active equations are represented by

$$\sum_{j=1}^n K_{ij} u_j = R_i \quad (2.21)$$

Here n is a total number of equations and i is an equation number, i.e., row number. To eliminate a typical equation $p = i$, the equation is first normalized to

$$\sum_{j=1}^n \frac{K_{pj}}{K_{pp}} u_j = \frac{R_p}{K_{pp}} \quad (2.22)$$

This equation may be rewritten as follows and stored in a file for later back-substitution:

$$\sum_{j=1}^n K_{pj}^* u_j = R_p^* \quad (2.23)$$

where,

$$K_{pj}^* = \frac{K_{pj}}{K_{pp}}, \quad R_p^* = \frac{R_p}{K_{pp}}$$

The remaining equations are modified and the p 's equation, i.e., p 's row, is eliminated from the following equations.

$$K_{ij}^* = K_{ij} - K_{ip} K_{pj}^* \quad (2.24)$$

$$R_i^* = R_i - K_{ip} R_p^* \quad (2.25)$$

$$\sum_{j=1}^{n-1} K_{ij}^* u_j = R_i^* \quad (2.26)$$

where $i \neq p$

This process is repeated for all other equations to be eliminated. Since this procedure is performed in the order of elements, the size of the wave front is directly affected by the

numbering scheme of elements. Therefore an effective numbering of elements is necessary to reduce the size of memory storage (see Section 4.4.5).

The main advantage that the finite element method has over other analysis techniques is its generality. Normally, it is possible by using many elements to approximate any continuum with a complex boundary and loading conditions to a degree that an accurate analysis can be carried out. In practice, however, obvious engineering limitations arise, a most important one being the cost of the analysis. As the number of elements used increases, a large amount of computer time is needed for the analysis and requires the preparation of relevant data to interpret the results. Furthermore, the finite element program and computer may limit the use of a larger number of finite elements to idealize the continuum. The limitations may be due to the high-speed and back-up storage available, or the round-off and truncation errors occurring in the analysis as a result of finite precision arithmetics.

A finite element program consists of three basic parts: pre and post processor and the finite element program itself (processor). In the preprocessor part of the program, the input data of the problem are read in and/or generated. This includes the geometry (e.g., length of the domain, boundary conditions, etc.), the data of the problem (e.g., coefficients in the differential equation, source term, etc.), finite element mesh information (e.g., number of elements, element length, connectivity matrix, etc.), and indicators for various options (print, no print, static analysis, degree of interpolation, etc.). The preprocessor generates the element matrices using numerical integration, assembles element equations, imposes boundary conditions, and solves the equations for the nodal point values of the primary variables. In the postprocessor the data is processed in a desired format for printout and/or plotting, and secondary variables that are derivable from the solution are then computed and printed.

CHAPTER 3

FEMORAL PROSTHESES

3.1 Introduction

The artificial reconstructions of diseased human joints have improved tremendously since the early 1960s, and the numbers of joint replacements in orthopedic surgery have grown almost exponentially. For the hip in particular, a multitude of different artificial joint designs are available, usually made of special metal alloys in combination with several types of plastics. Roughly speaking, artificial joint components can be categorized into intramedullary fixation device, where a stem is fixed into the medullary canal, and surface replacements.

Since some prostheses are wedged or screwed into the bone to obtain an appropriate support, some sort of fixation medium is required. The most popular is acrylic cement Polymethylmethacrylate (PMMA), a filling agent introduced in a viscous phase to adapt the smooth implant to the irregular bone. Recently, ready-made profiled surfaces or porous coatings are utilized, in closely fitting prostheses that allow bone to grow in and gradually grip the implant firmly.

An artificial joint has two distinct functions: to restore the natural kinematic motion of the joint, and to transfer the joint forces to the bone. The latter function must be fulfilled without causing pain or failure. Several types of biological and mechanical phenomena may enhance failure of a bone-prosthesis composite; these include:

1. Properties of the space-filling PMMA cement
2. Effect of wear and abrasion particles on the joint capsule and the tissues interfacing with the prosthesis
3. Possible sensitivity to the bone
4. Elastic properties of the implanted materials

5. Type and design of the implant
6. Implantation procedure
7. Biological, mechanical, and elastic properties of surrounding tissue

Most of these factors are interrelated and it is often impossible to delineate one single factor responsible for failure by loosening (Bogumill and Schwamm, 1984; Ducheyne and Hasting, 1984; Kline, 1988).

In this chapter dealing with the design criteria of femoral prosthesis, the separate sections are devoted to the discussion of the biomaterial, bone cement, and porous coating system.

3.2 Design Criteria for Femoral Prostheses

3.2.1 Introduction

The purpose of bone prostheses is to achieve a permanent anatomical substitution and functional replacement of bone tissue. The most common applications are hip prostheses, and the knee. The most widely accepted combinations are metal on plastic for the articulating surfaces of the artificial joint. A self-curing acrylic bone cement for fixation of the artificial joint to bone was first proposed by John Charnley (1961), originally for the case of the hip joint.

Since the prosthesis is designed to provide a permanent replacement of bone tissue, its durability is an extremely important factor. The demand for resistance to degradative processes (wear, fatigue, corrosion-fatigue, stress-corrosion cracking, etc.) is thus a major consideration in implant design. More durable metal such as titanium alloy and the cobalt-based alloy is used with greater frequency in bone implants. The use of 316L stainless steel is widespread as well. Similarly, the necessity for optimum implant design to reduce the stress in the prosthetic devices to values which are as low as possible, within geometrical constraints, while retaining a stress distribution in the surrounding tissue which is as physiologically normal as possible, is all the more important for bone implant.

This section will focus mainly on hip prosthesis. The detail of specific designs of these prostheses are considered. The emphasis will be based upon identification of some of the generic principles associated with such devices.

3.2.2 Design Principles

Although the total hip arthroplasty has helped to restore joint function and relieve pain for a long period of time, available prosthetic devices have had major problems in design and materials. The original generation of hip prostheses attempted to duplicate anatomical design, but the unsuitable alloys used in their construction resulted in unacceptable bending and fracture. A second generation prosthesis compensated with an exaggerated design and a valgus neck-stem angle which was prone to dislocation. A third generation, while taking advantage of new alloys, failed to consider the moment arm of the abductor muscles. As a result, hip mechanics were found to be abnormal. The new fourth generation prosthesis reproduces the normal anatomical axis of the hip joint (Bloebaum et al., 1984; Dorr, 1985). The design concept of restoring the normal anatomical relationships and stresses to the hip joint is accomplished by:

1. Reproducing Shenton's Line; the femur is realigned with the acetabulum into the natural anatomic position.
2. A metal-backed acetabular component increases rigidity, minimizes distortion, reduces peak stress concentrations in the cement, and distributes stresses evenly to the bone.
3. Varying the stem angle with neck length, and maintaining the body's normal weight bearing load line through the calcar.
4. A neck-stem angle which will restore the abductor moment arm. This allows the hip abductors to function more efficiently by decreasing the force required for stability. The resultant joint force is also diminished.

5. A tapered lateral flange can provide additional compressive load transfer to the cement.
6. The stem length may increase proportionately with the stem cross-section for a better fit in the femoral canal and reduce cement stress in the larger patient.
7. The stem cross-section is tapered with the lateral side wider than the medial side. This reduces shear stresses and increases compression at the cement-metal interface.
8. A titanium alloy for improved modulus of elasticity and fatigue strength.

Figure 3.1 collects and illustrates some of the design criteria for the ideal cemented stem design as far as present biomechanical knowledge and clinical experience allows (Cowan, 1989; Ducheyne and Hasting, 1984; Kline, 1988; Schmid-Schonbein, 1985; Skalak, 1987).

The diameter of the articulating ball (A in Figure 3.1) ranges from 22 to 36 mm in total hip replacement (THR) with a predominance of the 32 mm. Balls larger than 32 mm will certainly disappear in future, since they would require larger bone removal at the critical acetabular implantation site. However, a small diameter ball has certain disadvantages such as significantly higher rate of spontaneous postoperative dislocation.

Many THR devices offer three different neck lengths (B in Figure 3.1). The short-neck design should nearly never be used as it limits the postoperative range of motion (earlier contact of calcar or minor trochanter and socket in flexion/adduction or of greater trochanter and the lateral pelvic wall in flexion/adduction). In clinical experience the results concerning pain relief and range of motion are not satisfactory with a short-neck prosthesis. Long-neck prostheses which are most often used in the attempt to restore leg length equality tend to loosen earlier than standard medium-neck length prostheses. This can be explained by the lengthening of the lateral lever arm of the hip joint when using a long neck. This increases the load of the femoral prosthesis and the torque at the calcar area. Both parameters increase the risk of loosening of the femoral component through chronic overload of the bone-implant interface.

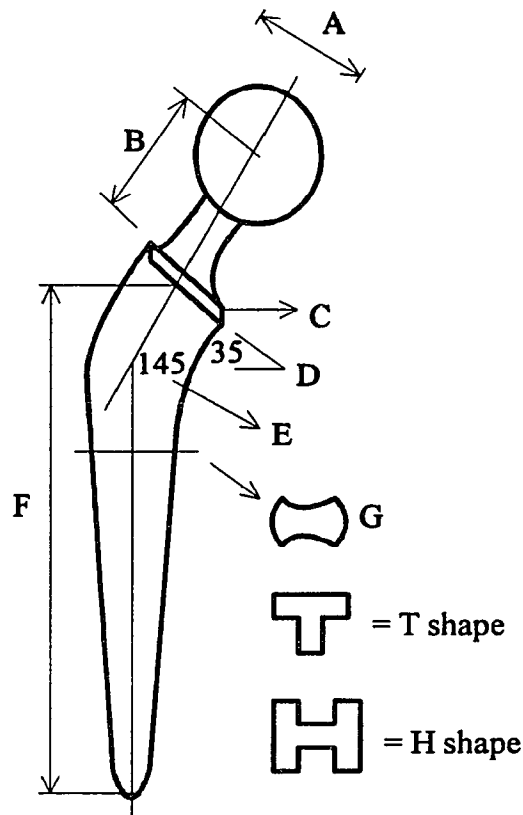


Figure 3.1 Essential design criteria currently under discussion for an ideal cemented stem design in total hip replacement.

The calcar support of a femoral prosthesis (C in Figure 3.1) is another component that affects prosthesis performance significantly. Small calcar supports (Charnley and Weber type femoral stems) have been preferred to large calcar supports because of their ability to affect loosening. The idea of having no calcar support has been supported by clinical and theoretical data. Small calcar support allows for resting the prosthesis on the cement cuff and therefore does not prevent the prosthesis from settling during remodeling. This combines the above advantages for small calcar support with a better load distribution on the cement cuff and minor risk of splitting of the cement cuff by sinking into it.

Biomechanical studies have stressed the importance of a neck support of 35 to 30° and a neck-shaft angle between 135 and 145° (valgus position, D and E in Figure 3.1). A

valgus prosthesis together with a long neck can be a dangerous prosthesis. The risk of persistent pain and early loosening overshadows the positive effects of this proposal. Lowering of the neck support angle from the original 45 to 35°, reduces the torque at this area during every load cycle. A femoral neck angle in valgus, i.e., more than 135° reduces the same torque by shortening of the lateral level arm. Both improvements within this "physiologic range" are considered to reduce the risk of loosening.

The length of the intramedullary system of the femoral prosthesis (F in Figure 3.1) varies from 12 to 18 cm for standard prostheses. Buchholz (1969) proposed a longer stem for permanent anchorage in the diaphysis of the femur. Most other researchers preferred a shorter (12 to 14 cm) stem and proposed a longer stem specifically for revision cases. It has been reported theoretically that the problem of mechanical loosening can be postponed by lengthening the prosthesis.

The rigidity of a femoral stem prosthesis is not only a matter of the material used, but also a matter of the size of the stem and its shape (G in Figure 3.1). Currently, the T and H shapes are the most acceptable since they are the most rigid against lateral bending.

There are three types of total hip prostheses in widespread use: straight-stem, curved-stem and M/D (Metaphyseal/Diaphyseal) fit prosthesis. The straight-stem prosthesis provides an anatomic medullary locking and the fit can be achieved by reaming endosteal bone. The curved-stem prosthesis which is designed according to the endosteal canal requires a wide range of sizes to fit the anatomic size and shape of the canal. One manufacturer has the curved-stem prosthesis available in twelve different sizes. The M/D fit prosthesis is a combination of the straight-stem and curved-stem prostheses and the prosthesis selection is accomplished by placing templates over the anteroposterior and lateral radiographs to minimize the amount of reaming.

The femoral prosthesis that is used in this study is made of cobalt-chromium alloy and has a M/D (Metaphyseal/Diaphyseal) fit stem with a non-collar, modular tapered neck, and is available in five lengths. The component is available in three-millimeter incremental

sizes ranging from 29 to 41 millimeters. The femoral component is porous-coated proximally and the stem shape is tapered. The stem length is available in sizes ranging from 121 mm to 148 mm and the stem diameter ranges from 11 mm to 17.5 mm. The prosthetic head is available in two sizes, 28 mm and 32 mm .

3.3 Materials Properties of Prostheses

3.3.1 Introduction

The variety and range of properties formed in various natural tissues in the body help set the criteria for properties that must be developed for a prosthesis. The advent and development of total joint replacement has brought many changes in the selection and applications of materials. Although materials used as implants in the musculoskeletal systems include metals, polymers, and ceramics, the considerations governing material selection are the same. These are; (1) no adverse effects of tissue on the implant or vice-versa (biocompatibility), (2) good mechanical properties and good maintenance of these properties (functionality), (3) wear and corrosion resistance in physiological environments, and (4) ease of fabrication and sterilization. Criteria, structures, and properties of metals, polymers, and ceramics for implants are described below (Black, 1988; Cowin, 1989; Ducheyne and Hasting, 1984; Kline, 1988; Schmid-Schonbein, 1985; Skalak, 1987; Wheeler, 1987).

3.3.2 Metal

Since bone has an ultimate tensile strength of approximately 70 MPa, the implant material should tolerate higher stress to increase the durability. The requirements for high ultimate tensile strength (about 700 MPa) in the past have restricted the choice of structural materials for fixation and prosthetic devices to metallic alloys. At present five metallic alloys are generally used:

1. Stainless steel

2. Cast cobalt-chromium-molybdenum alloy
3. Wrought cobalt-chromium-tungsten-nickel alloy
4. Commercially pure titanium
5. titanium 6Al 4V alloy

Some mechanical properties of metal implant alloys are given in Table 3.1.

Table 3.1 Mechanical Properties of 316 L Stainless Steel, Co-Cr Alloy, Ti and Ti-6Al-4V.

Material	Young's Modulus (MPa)	Tensile Strength (MPa)
316 L Stainless steel	193,000	540
Co-Cr (cast)	214,000	480
Ti (0% porosity)	110,000	400
Ti (40% porosity)	24,000	76
Ti-6Al-4V(0% porosity)	124,000	940
Ti-6Al-4V(40% porosity)	27,000	140

3.3.3 Ceramic

Ceramics is a group of materials that are compounds of metals and nonmetals in their highest oxidized state. In general, ceramics possess characteristic properties of mechanical brittleness, rigidity, and high temperature. The obvious advantage of ceramics is that they are relatively inert in body fluids and thus release negligible amounts of toxic degradation products. Their wear resistance is often quite good also. The main concern about the use of ceramics is the fact that they are brittle and may not have the mechanical properties required for the high load applications characteristic of many orthopedic implants. Thus, clinical applications of ceramic materials are mainly confined to situations where stresses are predominantly compressive.

The principal bulk parameters that control the mechanical properties of the ceramic component are the absence of sintering void (i.e., full theoretical density) and a fine grain size. Any void in the body of the ceramic acts as a stress-riser, similar to those at the

surface, and degrades mechanical properties. The fracture of ceramics is controlled by crack initiation, not by crack propagation. Grain size is also important because it controls the magnitude of the internal stresses produced by thermal contraction stresses. These are critical in ceramics because they can not be dissipated by plastic deformation as they can in ductile materials. Although the thermal contraction strains (stresses) are minimized by a random orientation of the individual grains and a small grain size.

3.3.4 Polymers

Polymeric materials generally have a restricted use in orthopedic applications, mainly because of strength limitations. There are several important exceptions, however. The bearing surfaces in artificial joint applications originally were direct metal upon metal designs. Due to unacceptable levels of metallic wear, this approach has been supplanted, and most present devices consist of a metallic component articulating against a polymer, usually ultra-high molecular weight polyethylene (UHMWPE).

The polymer used in over 95% of the polymeric joint components is high-density linear polyethylene. Polyethylene, polypropylene, and their copolymers are called polyolefins. These are linear orthoplastic polymers, meaning that they soften with increasing temperature at a little over 100°C. Polyethylene is available commercially in three major grades: low-density, high-density, and ultra-high molecular weight (UHMWPE). The general mechanical properties of the higher density polyethylene are improved over the other forms, although there is a decrease in the ductility and fracture toughness due to the crystallinity.

The first polyethylene was made by reacting ethylene gas at high pressure (100 to 300 MPa) in the presence of a catalyst (peroxide) to initiate polymerization. This process yields low-density polyethylene. By using a ziegler catalyst, one can produce high-density polyethylene at low pressure (10 MPa). There is a basic difference in the pattern of polymer-chain branching between a low-density and a high-density polyethylene. Unlike

the former, the high-density polyethylene does not contain branches. The result is better packing of the chains, which increases density and crystallinity. This is the reason why ultra high molecular weight polyethylene (UHMWPE) with its better mechanical properties of polyethylene are given in Table 3.2.

Table 3.2 Properties of polyethylene.

	Low density	High density	UHMWPE
Molecular weight (g/mol)	3×10^3 to 4×10^3	5×10^5	2×10^6
Density (g/ml)	0.90 to 0.92	0.92 to 0.96	0.93 to 0.944
Tensile strength (MPa)	7.6	23 to 40	3
Elongation (%)	150	400 to 500	200 to 250
Modulus of elasticity (MPa)	96 to 260	410 to 1240	800 to 1200

Finally, bone cements are employed for purposes of fixation in artificial joints. There are based on a polymethylmethacrylate (PMMA) system, and sometimes have additional material added such as BaSO_4 (a radiopaquing agent), antibiotics, or reinforcing fibers. Bone cement is discussed in the next section.

3.4 Bone Cement Interface

3.4.1 Introduction

Bone cement is one of the most effective methods for attachment. The success of total joint replacement is directly related to the ability to transfer the load uniform from the component to all of the surrounding bone. This depends largely on the fixation interface between the component and the bone. Presently, the fixation and stabilization of artificial joint components are accomplished by three different methods:

1. Polymethylmethacrylate (PMMA, also referred to as bone cement), pioneered by Charnley in 1970 has been used in the greatest number of clinical applicants to secure the firm fixation of joint prostheses such as hip and knee joints.

2. A much newer technique involves use of a porous surface between the component and bone that allows tissue growth into the pores, which forms a mechanically sound, interdigitating interface.
3. Current experiments use material to which bone will bond as coatings on the load-bearing components.

Bone cement is thought by many investigators to be the weak link in the artificial joint chain. Besides the problems with interfacial strength, and thermal necrosis due to the exothermic polymerization reaction, other difficulties identified rarely in some patients are tissue reaction, and difficulty in cement placement at surgery.

The widespread perception of the shortcomings of bone cement has provoked a great effort to find ways to improve the performance of this material. Precoating the prosthesis with a PMMA layer to (1) reduce the amount of released toxic products, heat production, and thermal shrinkage, (2) increase the interfacial strength, and (3) provide better positioning has been the focus of several investigations. Fiber reinforcement to improve mechanical properties of bone cement has been studied. Recently centrifugation and vacuum processing to reduce cement porosity and increase its strength and durability have been studied (Black, 1988; Cowin, 1989; Ducheyne and Hasting, 1984; Kline, 1988; Skalak, 1987).

3.4.2 Mechanical Properties

Acrylic in the hardened state can exhibit a variety of microstructures. Under surgical conditions, cold-curing, room-pressure systems, such as Simplex-P bone cement, exhibit considerably porosity (~8%). Presence of pores and defects leads to alteration of mechanical properties.

Table 3.3 contains various mechanical properties for bone cements. Where dashes appear, data are lacking in the literature. Comparisons of data obtained under totally

different conditions are difficult to make. This problem has led to the formation of ASTM and ISO testing standard.

Table 3.3 Typical mechanical properties of some acrylics.

Property	One-phase Heat-cure PMMA	Simplex-P radiolucent	Simplex-P radiopacifier	Zimmer regular	Zimmer LVC
Elastic Modulus (MPa) Tension	2620 to 3170	2414 to 3103	1310	—	—
Compression	2550 to 3170	—	3130	—	—
Tensile strength (MPa)	48 to 76	32	28 to 46	10	13
Compressive strength	83 to 124	97 to 124	90	69	103
Tensile elongation (%)	2 to 10	2.4 to 5.4	4.6	—	—
Density	1.186	1.088	1.183	1.180	1.160

It should be emphasized that since mechanical properties of acrylic bone cement are external-property sensitive, the curing conditions may alter its properties. These external properties include pressure and temperature and curing time prior to testing. Brand name variations and the addition of radiopacifiers or other materials such as antibiotics will also affect mechanical properties. From Table 3.3, comparisons of testing modes and fabrication methods illustrate the weakening effect of porosity in PMMA. Presence of porosity reiterate the fact that two-phase acrylics are weaker than the one-phase system.

3.5 Porous-Coated System

3.5.1 Introduction

Porous materials have been used as an alternative method of fixation to obtain a better mechanical interlock between prosthesis and bone. This is due to the fact that bone cement has not provided long-term optimal performance. Mechanical interlocking can be obtained if the surface of the prosthesis is porous in order for ingrowth of tissue and bone into the pores can occur.

The interface of a high-modulus prosthesis and lower-modulus bone results in high interfacial stress. It has been suggested that interposition of a porous material bonded to the surface of the stem of the prosthesis would reduce the magnitude of the interface stresses and at the same time allow mechanical interlocking via bone and tissue ingrowth. For this case, the surface must resist creep under the clinical stress state and also have sufficiently high yield strength to resist plastic deformation. Various, porous surfaces are in use these include metal, ceramics, polymers, and carbon.

3.5.2 Porous Material Development

A large variety of materials were produced for experimental bone ingrowth studies and for eventual clinical application. The specimens and implants came in either a fully porous from or as a substrate with a porous coating. Both for the porous structure (either by itself or as a coating) and for the substrate, the various materials which were already in experimental or clinical use were employed. The metals included stainless steel AISI 316L, cobalt-chromium alloys, and titanium. The ceramics were hydroxyapatite, calciumaluminates, zirconium oxide, and alumina. Polymers included porous polysulfone, porous polymethylmethacrylate, porous high-density polyethylene, and a composite form of porous polytetrafluoroethylene. In addition, different forms of porous carbon were used.

Although porous materials are still an active area of research, some of the basic principles underlying the use of porous materials have been clarified. There appears to be an optimum pore size range for tissue ingrowth provided that a material has sufficient intrinsic biocompatibility. The ranges obtained by various investigators indicate that a pore diameter less than about 50 to 100 μm will be infiltrated with fibrous tissue only.

Between 50 to 100 μm and about 250 μm mineralized tissue or osteoid will grow into the pore network. This has been attributed to the fact that a larger pore size is required for blood vessel ingrowth and to allow formation of full Haversian systems. Ingrowth speed increases with increasing pore size above 50 μm and reaches a peak at about 400 to 500 μm .

Tissue infiltration into some porous networks has been reported only to limited depths in the approximate range of 0.5 to 0.8 mm at implantation times ranging up to 5 months. Consequently there is no advantage to making an implant device porous throughout. The usual practice is to use a porous coating on a solid substrate. There are various manufacturing processes for producing porous coatings. Sintering is the most common which flame sprayed coatings are also possible.

Potentially there are great advantages to the use of porous implant materials. From the biomechanical point of view, a porous material offers a more even load transfer across the natural tissue-device junction. This lessens the difficulties associated with resorption, on the one hand, and sensitivity to impact loads, pressure necrosis, and pain due to wear of bone against the biomaterial, on the other. Another advantage of the use of porous implants is the elimination of problems associated with other types of fixation such as bone cement.

There are several potential disadvantages associated with the use of porous materials which should also be mentioned. The interstices in porous materials can be remote from the main blood supply, and if infection originates in the area before ingrowth has had a chance to occur, it can flourish within the material. Another disadvantage is that, to

achieve adequate fixation by tissue ingrowth, very restricted weight-bearing is required for relatively long periods of time amounting to several months. For substantial bone ingrowth to occur, micro-motion at the interface should be an order of magnitude less than the pore size. In contrast, a patient with a conventionally cemented total hip replacement is enjoying at least partial weight bearing on the affected limb after about one week.

There is a further disadvantage which potentially many occur with porous metals in surgery. In contrast to the relatively inert ceramic materials first studied for porous implant applications metallic material (even though they are quite corrosion resistant) are inherently more reactive. The use of a porous material with about ten times the surface area of a planar interface will cause roughly an order of magnitude increase in the amount of corrosion products released by the implant into the in vivo environment. The significance of these findings is uncertain. Although porous implants are usually considered biocompatible, a recent report has shown inflammatory reactions in a canine model one to two years after porous resurfacing hip arthroplasty.

3.5.3 Mechanical Properties

The pore size, the pore geometry, and the porosity directly influence the mechanical and elastic properties of porous structures and the bonding of these structures to any substrate. These properties can, but do not need to be, critical. This primarily depends upon the type of application and the magnitude of the loading environment.

Few data on the elastic and mechanical properties of porous ceramics have been published in the biomedical material literature. Lyng et al. (1973) evaluated porous Al_2O_3 for its potential use in the tibial plateau. They also characterized the strength of their implant material. This was a 96% pure $\alpha\text{-Al}_2\text{O}_3$ with 60% porosity and a pore size varying from 100 to 750 μm . Spector et al. (1978) determined mechanical properties of polymeric material, namely, polysulfone. As shown in Table 3.4, the tensile strength tested at one strain rate varies between 2.8 and 5.9 MPa, depending upon average pore size and

porosity. The apparent modulus of elasticity varies between 220 and 406 MPa. From the data it is not clear what factors govern the variation of tensile strength and apparent elasticity.

Table 3.4 Ultimate tensile strength and apparent modulus of elasticity of porous polysulfone.

Average pore size (μm)	Apparent modulus of elasticity (MPa)	Porosity (%)	Ultimate tensile strength (MPa)
56	323.8	54	2.8
88	289.4	54	4.1
127	337.6	55	3.6
181	406.5	66	5.9
269	406.5	60	4.6
336	220.5	61	3.4
386	303.2	66	4.8

For the properties of porous metals, a distinction must be made among the various approaches. Hirschhorn et al. (1971) reported ultimate tensile strength values for a coarse and a fine power. They found it necessary to use the larger powder size, since the smaller-size fraction yielded porous structures with very small pore sizes. Mercury porosimetry revealed an average pore size of only 10 to 15 μm at 60 to 65% density. The coarse Ti powders (+40 mesh) were compacted and sintered to different densities in the range of 65 to 95% density. Pores up to 200 μm were observed. However, the strength and ductility of these materials were limited. The strength and elongation at fracture were 23 MPa and 0 at 65.3% density and 56 MPa and 0.2 at 73.8% density.

The strength data of the VMC (Void Metal Composites) system were reported by Niles and Lapitsky and Wheeler et al. (1973). These data are compiled in Table 3.5.

Table 3.5 Ultimate compressive strength of Ti-6% and Al-4% V-VMC porous structure.

Material Ti-6% Al-4% V	Pore size(um)	Density(%)	Ultimate compressive strength(MPa)	Apparent modulus of elasticity(MPa)
	275	20	10	2800
	275	50	172	3500
	360	50	165	4200
	460	48	110	3150

The implant advantages resulting from the inherent mechanical and elastic properties of the porous or fiber structures were recently summarized.

1. With regard to polymeric coatings, metal coatings are characterized by superior bonding to a metal substrate.
2. A porous fiber structure is formed by a continuous network of channels with the same mean diameter throughout the structure. In contrast to this, porous ceramic or metallic powder structures have pores which are interconnected by much smaller channels.
3. Metals fiber structures display better strength and ductility for a given density and pore size.
4. The elasticity of porous fiber or wire structures closely matches the elasticity of surrounding bone tissues.
5. Upon tight insertion into the surgically prepared bone cavity, a press fit is readily achieved due to the elastic deformability of the structure; at the same time, the porous structure remains an open structure.

CHAPTER 4

MATERIALS AND METHODS

4.1 Scanning Femoral Bones

Three femora were scanned pre-operatively at the Radiology Department of Saint Barnabas Medical Center in Livingston, New Jersey. Case 1. An active, 30-year-old male patient had suffered osteoarthritis in the left femur and was treated by left total hip arthroplasty. The left femur was scanned from 20 mm below the femoral head to the knee in March 1992. Anteroposterior and lateral radiographs of the left femur were evaluated at 14 months postoperation. Case 2. An active, 36-year-old female patient had suffered osteoarthritis in the left femur and was treated by left total hip arthroplasty. The left femur was scanned from 10 mm below the femoral head to the midshaft in June 1992. Anteroposterior and lateral radiographs of the left femur were evaluated at 12 months postoperation. Case 3. An active, 50-year-old male patient, who had two motor vehicle accidents, presented with a markedly deformed femoral shaft in the right femur due to the femoral fixation. The patient had suffered post traumatic arthritis in the right femur and was treated by right total hip arthroplasty. The right femur was scanned from 10 mm below the femoral head to the midshaft in January 1993. All of the three femora were scanned by Siemens Scanner, Somatom DR.

Case 1 was scanned and the total of 60 slices were produced. In addition, a scout view, and four images with different pixel size at the same slice were produced. The anteroposterior or lateral view image of the scanned femur is called the scout view is produced by the computed radiographic localization, provides anatomic information to facilitate selection of the range and spacing of scan slice levels desired in a scan sequence and also facilitates patient positioning. In the computed radiographic localization, the X-ray tube and detectors remain stationary while the patient moves through the gantry

aperture. The tube is then energized to produce X-rays in rapid pulses, which are sent to the computer for synthesis. The result is an image that looks similar to the conventional radiographic image. Case 2 and Case 3 were scanned from 10 mm below the femoral head to the midshaft and there were 40 slices produced. These images were stored on the 12 inch optical disc in terms of digital information. This digital information, together with other parametric information stored in the disc directories, permit later reconstruction of the scanned images. The pixel data (CT numbers) indicating the pixel radiographic densities, are represented in the CT data file by positive integers in the range of 0 to 4095. These integer values are stored by the computer system in two-byte words, each byte consists of 8 bits. The scanned information is tabulated below (Table 4.1).

Table 4.1 The scanned information for the femora.

CT scanner	Siemens Somatom DR
Scanned bone	femoral bone in vivo
Slice numbers	60 and 40
Matrix size	Square (512×512)
Pixel size	0.257×0.257 mm
	0.260×0.260 mm
	0.279×0.279 mm
Slice spacing	5 and 10 mm

The Siemens Somatom DR is a CT scanner utilizing a direct fan-beam principle and a rotating detector array opposite a pulsed X-ray source. The image processor is capable of rapid scanning and high speed image reconstruction. With the Somatom DR, up to 1440 high voltage pulses are generated during one rotation of the X-ray tube detector system around the object scanned. The pulse duration can vary between 1 and 5 ms depending on the technique factors. The smallest angular distance between two consecutive pulses is 0.25 degrees, corresponding to 1140 projections in 360 degrees. Other pulse sequences result in angular intervals to 1 degree for high scan speeds. The output signal of each

detector is amplified and integrated, and are then digitized and held in an acquisition store for preprocessing and image reconstruction (Siemens Operating Instructions, 1986; Technical Information, 1978).

During one scan, between 240 and 1440 X-ray pulses are generated corresponding to scan times between 1.4 and 14 seconds. With each pulse, up to 512 projections across the object are accumulated. Up to a maximum of 737,280 raw data projections are processed to generate a reconstructed image. The measurements are recalled from the temporary buffer and processed by the high speed processor, resulting in a fully reconstructed image less than 1 second after the scan is completed.

The raw data and reconstructed images can be stored on a variety of archival devices, such as disk store, magnetic tape, and diskette. The digitally archived raw data files may also be post scan reconstructed using a variety of techniques for improved diagnostic images. A matrix size of 512×512 or 256×256 can be selected, and rapid reconstruction is possible with either matrix size.

Images with a total number of pixels 262,144 (512×512) are reconstructed in this research. It is within the capability of current computers, aided by special-purpose high-speed arithmetic hardware (often called array processors) to perform such reconstructions in a few seconds. After completion of the scans, the reconstructions are performed simultaneously in parallel with the scans.

4.2 Processing the CT Data

4.2.1 Transferring the CT Data

After the bone is scanned, the next important step is to transfer the CT data from the computer system of the CT scanner to the NJIT computer system. A 512×512 image occupies 0.5 MB (Mega Bytes) memory and an optical disc can save the data up to several GB (1 GB = 1000 MB). The NJIT computer systems translates the CT data stored by either the magnetic tape or cassette. CT data scanned at St. Barnabas Medical Center was

stored on a 12 inch optical disc. The optical disc CT data was transferred to cassette by Siemens Company in Iselin, New Jersey. This CT data is reconstructed to create a finite element mesh based on the CT file pixel information (see Section 4.3).

The translated CT output file contains text information and the CT number in binary format. In the following sections, the structure and translation of the CT data will be discussed.

4.2.2 Structure of The CT Data

A typical CT archive disc or tape consists, in general, of two main parts: disc directories and display file.

1. Disc Directories: Contain information on the display data files and consist of a main disc directory and display file directories.
2. Display Files: This section contains display files; each file consists of a file header and the CT data.

The file header contains information regarding the display file, such as the number of slices and thickness, pixel size, and more details used for later reconstruction and display of the scanned object. The slice header contains information regarding the given slices, such as number and relative location. The image pixel data, CT numbers are stored next to the header in 2-byte words, one word for each pixel. This information occupies the major part of CT archive disc. This kind of structure of CT data is used in modern CT scanners.

4.2.3 Converting the CT Data

Handling data conversion between binary format and decimal format under program control requires the details of file header and image size. For the scanned femur, each image contains 1032 blocks. Each block equals to 512 bytes, and each pixel occupies two bytes. Thus, the matrix size in each image is 512×512. A converting method is developed according to the original image format provided by Siemens Company. The C language

programming with the ability of setting a specific window was developed to solve the conversion problem. In this program the user can select the specific reconstructed area to decrease the memory occupied.

4.3 Reconstruction and Display

4.3.1 Reconstructing the CT Image

A typical 512×512 image generally occupies 0.5 MB (Mega Bytes) memory. For 60 images in a scanned femoral bone, the total memory required is 30 MB. To conserve memory, the general procedure is to reconstruct images which bound any desired portion of the scanned image by selecting the length and width of the image (Figure 4.1). Two "C" language programs were developed for the reconstruction and display the routine characterized by the following features:

1. The global Cartesian coordinate (x, y) is set in the square image (512×512). The first point of the image matrix, the upper left pixel, is taken as the origin (0,0).
2. The square image is designed to display on X-terminal using the gray levels. When the mouse is pressed at any position of the image, the screen will show the coordinate of this position.
3. A program lets the user select the coordinate of the starting point (the left corner point), width, and length to reconstruct the original image.

Since the useful size of the scanned bone cross sections occupied about 40 percent of the total reconstructed area, this reconstructed procedure is performed to save space and time. Before creating the 3-D finite element model, substantial amount of unnecessary data was eliminated, and then the reconstructed CT data was applied to create a 3-D model for prosthesis simulation and stress analysis.

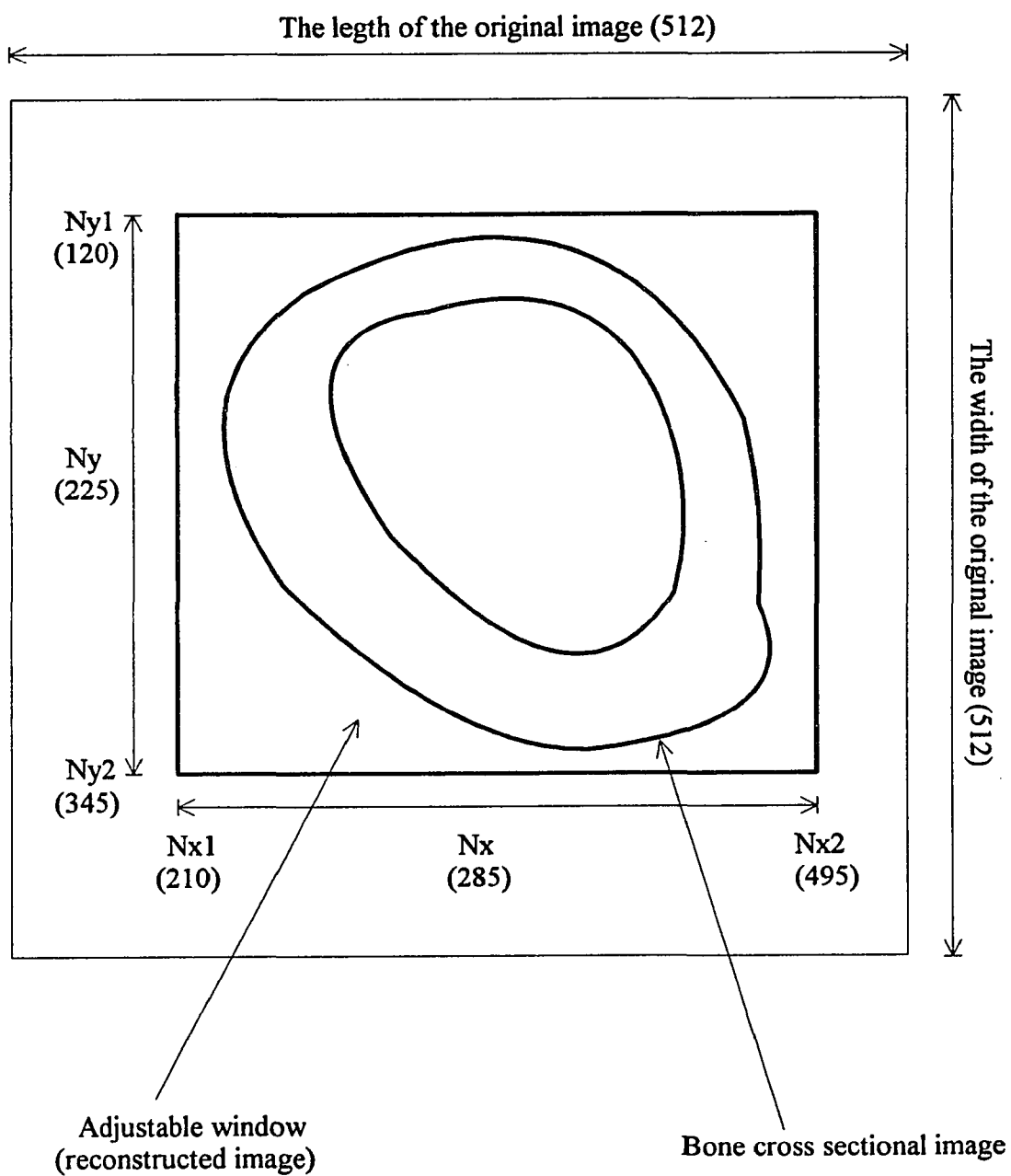


Figure 4.1 The reconstructed area of the scanned femoral cross section.

4.3.2 Gray Level Images and Color Display

A digital image is similar to a matrix. It is useful for representing pictures and is well suited for digital machines. Before the actual definition is given, an example will be presented.

Consider the xy plane as being partitioned into square regions, much like graph paper, with each square centered at a lattice point (i, j) , i and j in the set Z of integers. Each square centered at a lattice point is called a pixel, with the square centered at (i, j) being called the (i, j) th pixel. The set of all lattice points is denoted by $Z \times Z$. A digital image is obtained by assigning to each pixel a value, called a gray value, may be as small as 0, or as large as 255. Positive integer values are used in the study. Sometimes negative or noninteger values are used to denote gray levels in the other images.

In the computer system used, the monitor can display 256 gray levels at once, therefore, the gray values should be the range between 0 to 255. As the previous subsections mentioned, the CT data can be obtained. These CT numbers are not within the range of gray scale. Therefore, a scaling operator is used to obtain a presentation matrix. Since the CT numbers range from 0 to 4095, the scaling operation can be obtained to divide the elements of the matrix by 16.

In the UNIX computer system, two methods can be considered to display the cross sectional geometry and the intensity of each pixel of the image represented by the pixel of CT number. One uses gray levels on which variable gray values represent the variations in density of the cross section pixels. The other one is a high-resolution color to represent the pixel of CT number. For each of the two methods, programs are developed to display the gray levels and color image. The C language program is written to display gray levels image on an X-terminal. The other program written by FORTRAN language program, which combines HOOPS package to display the color image. Figure 4.2 displays 17 images of the scanned cross sections used to generate the finite element model for Case 1. Figure 4.3 displays 17 images of the scanned cross sections for Case 2. Figure 4.4 displays

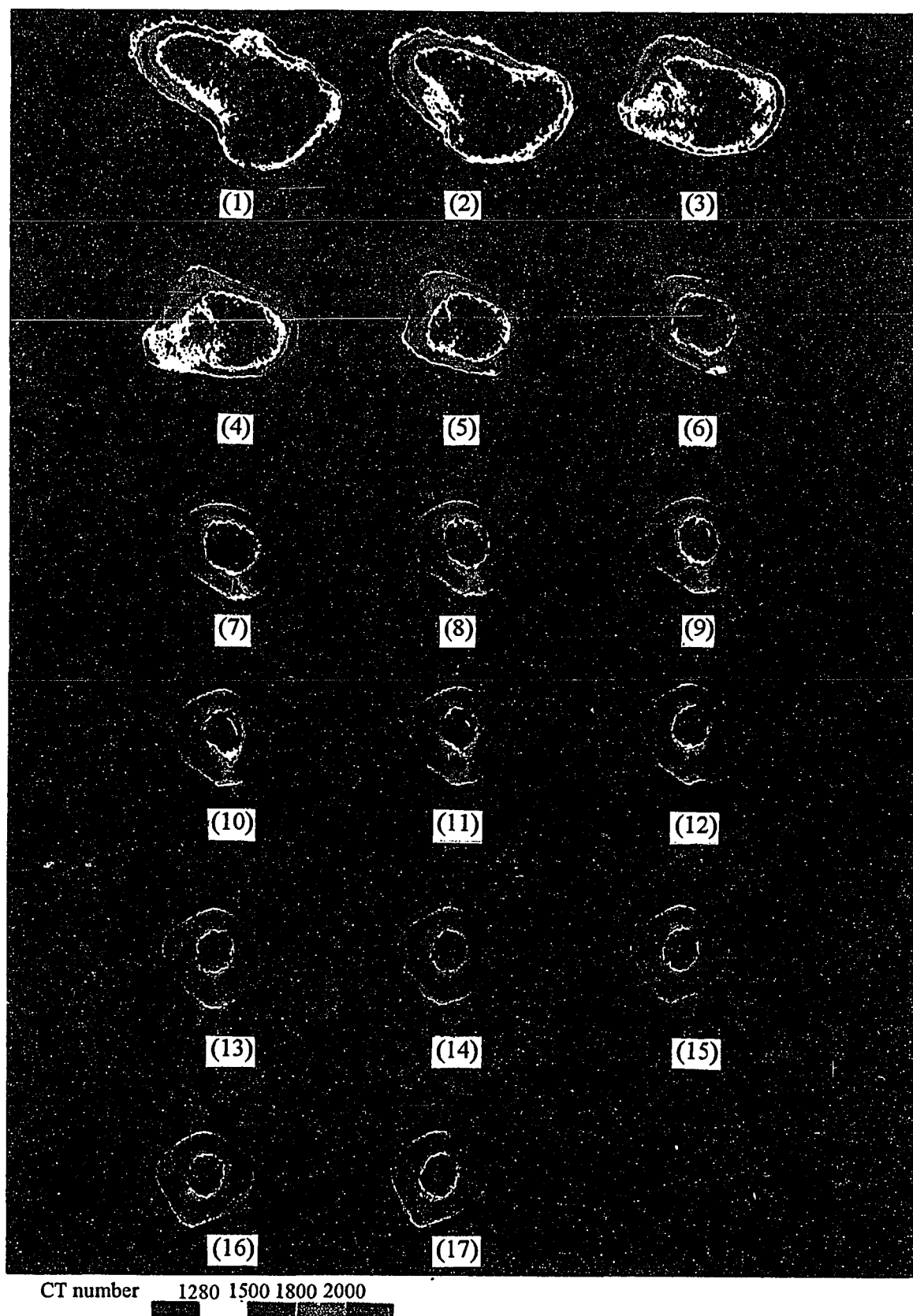


Figure 4.2 The reconstructed images of Case 1.

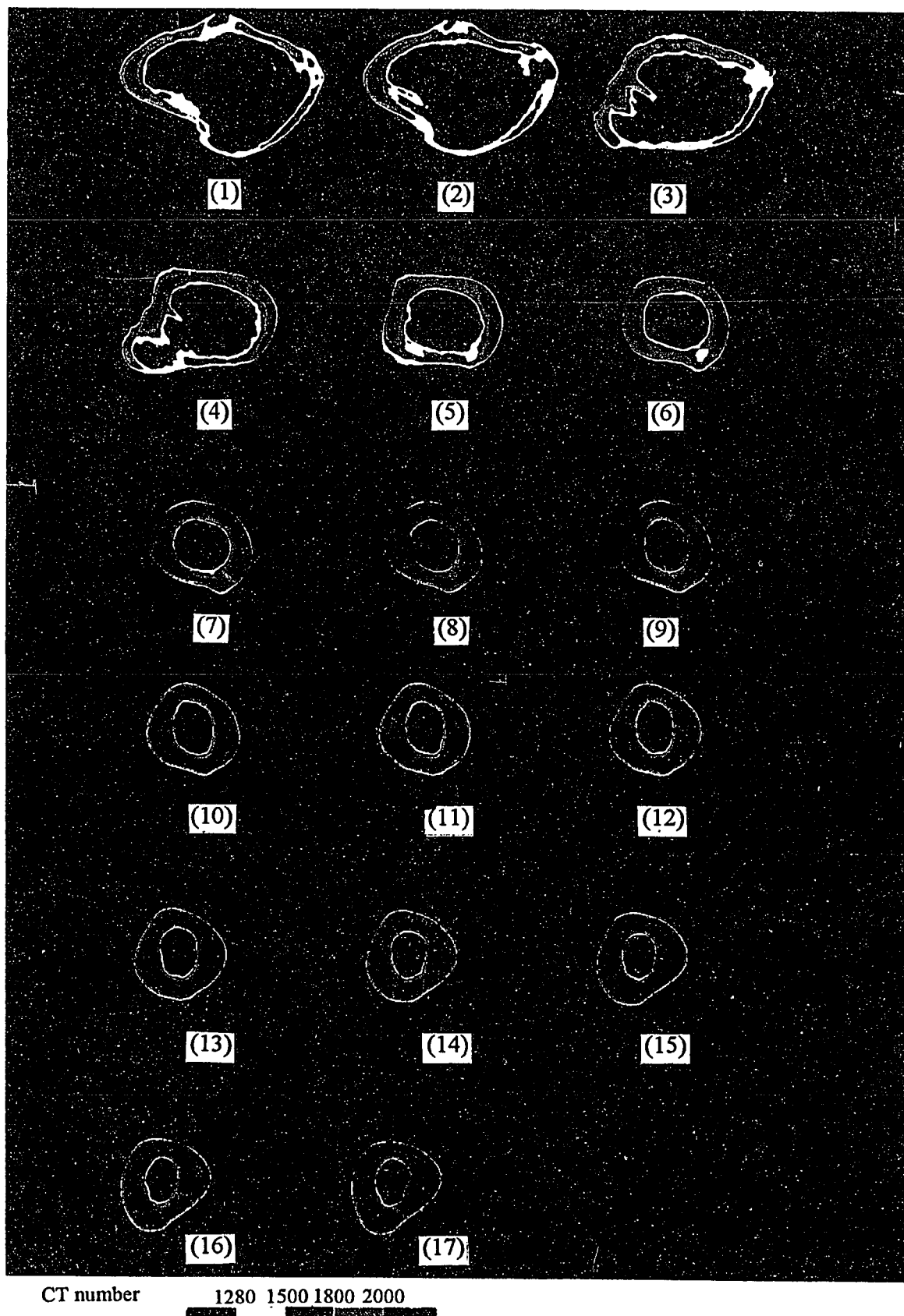


Figure 4.3 The reconstructed images of Case 2.

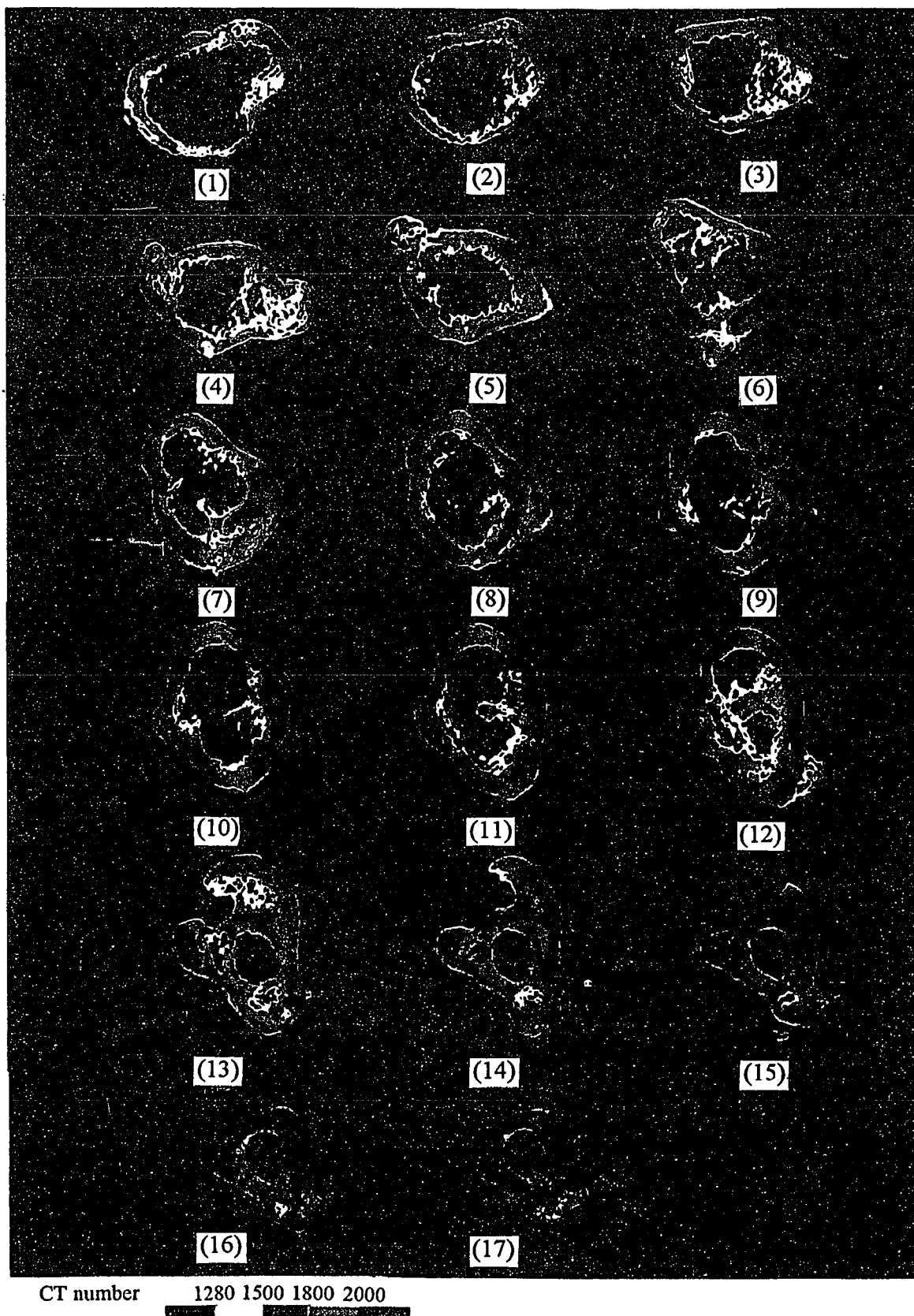


Figure 4.4 The reconstructed images of Case 3.

17 images of the scanned cross sections for Case 3. The scanned cross sections are shown at the same slice position for the three cases. In the color CT image, the different colors represent different CT number levels including: black (<1280) yellow (1280~1500), blue (1500~1800), orange (1800~2000), and brown (>2000). These ranges are selected according to the CT number distributions of the scanned cross sections. The minimum compact bone CT number is taken as 1280 (see Section 4.4.2). The black color represents the cancellous bone and soft tissue in the medullary area. The other colors represent the different CT number levels of the cortical bone. There are higher CT densities at the medial proximal end of the femur (calcar cortical bone), and there are lower CT densities and a thin cortex at the lateral proximal end of the femur. In the CT scans of each case, the first image is the proximal cross section of the scanned femur. The shape of the bone cross section is nearly elliptical at the proximal femoral side and is close to round at the distal side (midshaft). For Case 3 (the fractured femur subsequently reduced and healed), the bone has obvious changes in bone geometry and bone density.

4.4 The Design of Auxiliary Software for a Finite Element Program

4.4.1 Introduction

The development of pre- and postprocessing of finite element computer analysis is an important procedure for the stress analysis of the femur with prosthesis. Pre-processors perform such functions as geometry definition, geometry discretization (mesh generation), model display, model editing, node and element renumbering as well as load and boundary condition definition. Postprocessing may be concerned with stress and strain analysis and display.

Finite element program, ANSYS (Swanson Analysis Systems Inc.), utilizes mathematical procedures to generate a three-dimensional finite element model. The model generator allows the user to define the geometry of the model with points, lines, arcs, splines, edges, surface and volumes. The resultant continuous surfaces and volumes are

then subdivided by the mesh generator to create nodes and elements. The program is designed to run in batch, interactive, or a combination of both. The program default is the batch mode. An input data file is required for the batch run. The input data file consisting of a series of commands and variables is read by the program from the top of the file to the bottom of the file to define geometry, finite element meshes, boundary conditions and loading conditions.

In interactive programs like ADINA and IDEAS, the process of model definition comprises several stages. First, a mathematical definition of the geometry is determined, and then the discretization process may be carried out. In creating the geometrical model, mathematical methods for the representation of curves and surfaces in three dimensions typical to those used in computer aided design may be employed. The second stage of the mesh generation employs mathematical methods for the automatic subdivision of complex geometrical configurations. A typical example is the case of three-dimensional solid continuum, where a volume, bounded by continuous surfaces, may be subdivided into a number of brick-type elements.

In order to combine the finite element program with the CT scans, the batch mode of the finite element program is used. The model geometry of the femur is defined using the CT data. The high resolution data of the scanned bone carry radiographic density information (CT numbers) in addition to the geometric information. A special purpose mesh generator was developed as a part of the pre-processor to generate the finite element discrete mesh directly from the discrete image obtained from the reconstructed cross sectional pixel images. This procedure avoids the definition of continuous surfaces as a preliminary stage for the model boundaries definition and discrete-to-continuous and continuous-to-discrete conversion, which saves computation and increases the accuracy of the generated model.

The auxiliary software for the ANSYS finite element program includes the pre-processor which reads a CT data file, selects the bone prosthesis, and creates a three-

dimensional finite element model, used as an input data file for the finite element program.

The pre-processor consists of the major program sections as follows:

1. CT images display: The cross sectional images are reconstructed. The CT images redisplay on the color monitor using HOOPS software. The displayed cross sections are used to examine the scanned image.
2. Edge detector: The cortical (compact) bone boundaries of the scanned cross sections are detected and stored.
3. Nodes generation: The routine is to convert the node position from the pixel position defined by relative pixel number to the global Cartesian coordinate system.
4. The bone prosthesis simulation: The routine provides the prosthesis selection from the canal size of the scanned femoral bone. The prosthesis design satisfies the manufacture's size and the canal size also provides information to select the fitting prosthesis.
5. Mesh generator: This section includes the routines which create the three-dimensional finite element mesh of the scanned femur and bone prosthesis. The mesh consists of nodes and elements which are assigned with material elastic properties.
6. Model display: Two-dimensional plots of the model cross sections and three-dimensional display of the bone section model are produced for user examination of the model.

After the CT data is processed by the above computer routines, the mesh information of the three-dimensional model is formatted to create an input file which can be read by the selected finite element program (ANSYS) according to the program requirement.

4.4.2 Edge Detection

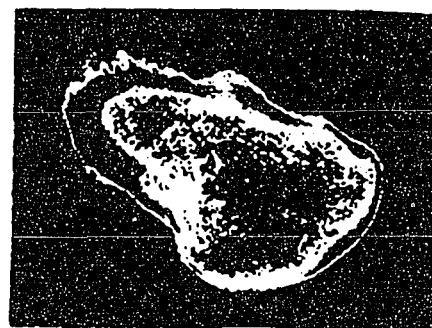
The CT data matrix contains the data of the cross sectional image. Because of the Cartesian nature of the image pixel line, an approach of consecutive pixels, first order edge detection routine is selected. For each cross section (Z direction), the pixels are tested consecutively in the X direction, then line by line in the Y direction, compared to a specific threshold value, a CT value of the selected minimum compact bone. The outside and inside borders of the compact bone zone in each cross section are detected and displayed by this routine. The minimum CT value of the compact bone which indicates the cross sectional borders is selected according to the range of the CT densities found in the scanned bone. The CT numbers of the reconstructed images may be displayed and examined for each pixel. The CT numbers of air and water are determined from the displayed reconstructed images. The characteristic water CT number is 1012 ± 12 , while the characteristic CT number of compact bone, which is not as homogeneous as water, is in the range of 1400 to 2000. The pixels which are on the border line between the water region and the compact tissue of the scanned image may carry any CT number in the range of 1000 to 2000 depending on the proportions of water and compact bone in the scanned pixel.

The minimum compact bone CT number is selected by the user. The suggested minimum compact bone CT number is taken as 1280 for the scanned femur. Figure 4.5 displays the first cross section in Case 1 for the different threshold values, the selected minimum compact bone CT numbers, 1100, 1200, 1280, and 1400. Compared to the original X-ray scan, the reconstructed image is close to the original X-ray scan when the threshold value is taken as 1280. The typical shape of the bone cross section consists of two concentric border loops, which bound the compact bone zone in between. The edge detection algorithm can be developed due to the characteristic of the bone shape.

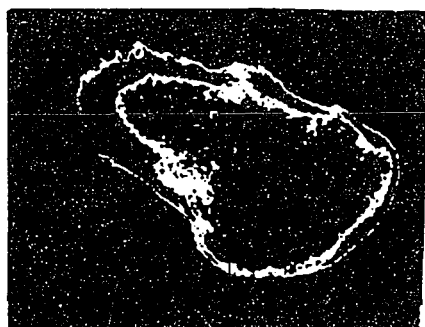
The border detection algorithm uses a sequential search procedures which are applied in four directions: $-x$, x , $-y$, and y , towards the center of the image. The detected



(a)



(b)



(c)



(d)

Figure 4.5 The CT scans generated by the different threshold values (a) 1100 (b) 1200 (c) 1280 (d) 1400 for the first cross section of Case 1.

border pixels are stored for later manipulations. The internal and external circumferential borders bound the compact bone in each detected cross section eliminating air, water, soft tissues and spongy bone in the scanned image. The border detector consists of a main procedure and four searching subroutines for detecting each pixel line in forward (+x) and backward (-x) direction, and for detecting the external and internal border pixels.

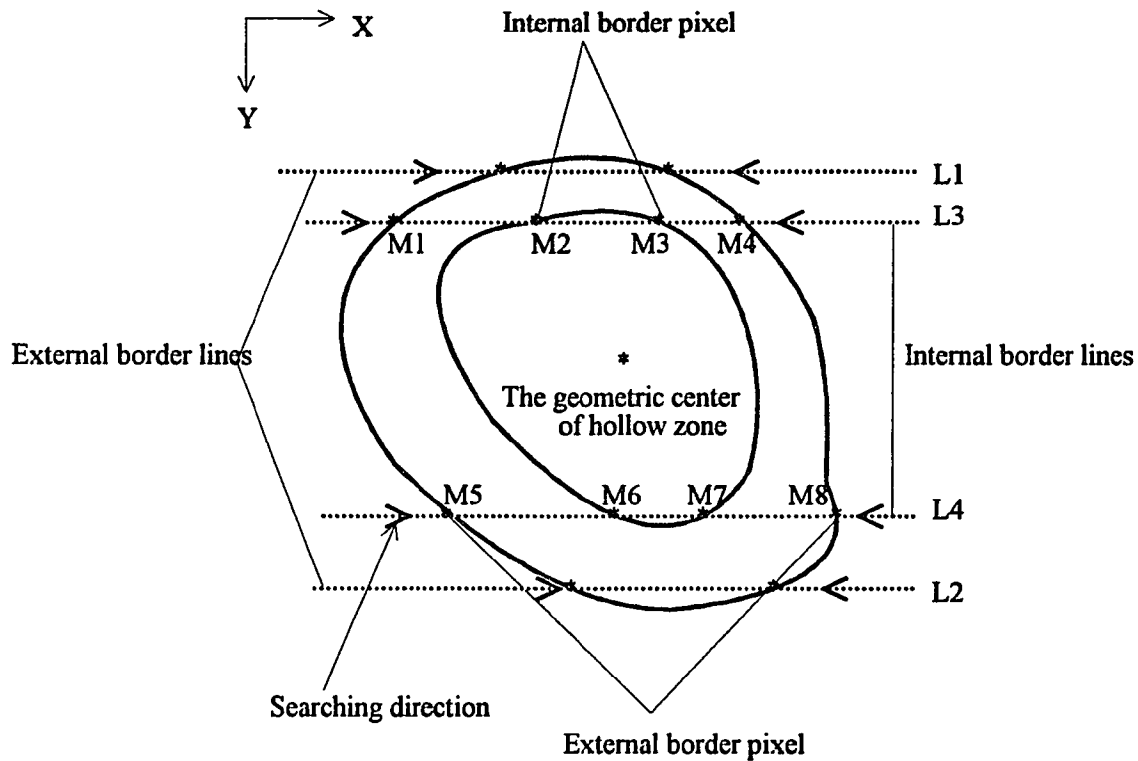


Figure 4.6 The cross section borders as defined in the edge detector.

When four internal and external border lines (L1 through L4) and eight internal and external border pixels (M1 through M8) are obtained by the detection algorithm, the geometric center of cancellous bone (hollow zone), which is determined by the average value of M2 and M7 coordinates (Figure 4.6). The relative pixel and line position represents X and Y coordinate respectively. The geometric center of cancellous bone will be used to search for the nodes as an important reference point, and the reference point is also the center point of the bone prosthesis. The node searching routine and prosthesis

designing routine are developed to display the selected finite element nodes of the three-dimensional model and will be explained next to the node selection routine and prosthesis designing procedures.

4.4.3 The Node Selection Methods

The node selection routine selects and stores a determined number of finite element nodes, which are represented by Cartesian coordinate system, in the cross sections. The selected nodes are pixels, defined by their relative location in the image. The origin of the coordinate system is determined to be the left upper corner of the previously reconstructed window.

The selected coordinate system origin is set for convenience since the window size and location are constant in all the cross sections. By this coordinate system, the image pixel lines are represented from top to bottom by the positive y coordinate, the line pixels from left to right by positive x coordinate, and the consecutive cross sections from first to the last, by positive z coordinate. Hence, the selected node can be represented (K, L, M) where K, L, M are slice, line, and pixel numbers respectively. Then the pixel data can be converted to the geometric position since the slice thickness and pixel size are known. For example, the reconstructed image of the scanned femur has a 10 mm slice thickness, and pixel size of 0.257 mm×0.257 mm, then (10, 10, 10) is at (90, 2.57, 2.57) for the mm units.

There are two methods to determine nodes; the straight search and radial search. The radial search combined with the edge detector is used to determine nodes in this study.

4.4.3.1 Straight Search. This straight search method was developed by S. A. Marom (1986). The edge detector routines which have been described in the previous section locate two external, upper and lower border lines (L1, L2) of the compact bone in each cross section. The edge detector routines also find two internal, upper and lower border

lines (L3, L4) of the compact bone image. The ranges of bone pixel lines (L3–L1), (L4–L3), and (L2–L4) are divided by a discrete division algorithm in such a manner that the divided line numbers are selected equidistant from each other. These lines are the selected node lines of a two-dimensional mesh generated for each cross section. For example, if the division number is:

the division number = 2 for the ranges of (L3–L1), and (L2–L4)

the division number = 3 for the ranges of (L3–L4)

and the external and internal, upper and lower, border lines found by the edge detector routines:

$L1 = 10, L2 = 250, L3 = 50, \text{ and } L4 = 200.$

The selected node lines are determined by the discrete division algorithm and the indices are computed to form the "LINES" array:

$LINES(1) = 10, LINES(2) = 30, LINES(3) = 50, LINES(4) = 100, LINES(5) = 150, LINES(6) = 200, LINES(7) = 225, \text{ and } LINES(8) = 250.$

Figure 4.7 shows the selected node lines. The internal and external border pixels which are regarded as the reference points of the selected nodes can be determined from the edge detector routines. Each external border line has two border pixels and then the nodes are selected in equidistant between the two border pixels. If the number of the nodes are three, the external border will have four selected nodes. Since each selected node line has the same selected node numbers, the four internal border should be the four selected nodes. The desired numbers of nodes and lines selected in each cross section can be adjusted by the user. If the number of nodes are 4 in the x direction and 8 in y direction, each cross section includes a total number of $4 \times 8 = 32$ selected nodes (Figure 4.8). When the above steps are applied on each selected cross section comprising the model to form a three-dimensional finite element model, twisted elements can occur. Therefore, a new radial method is developed and applied to create a femoral finite element model.

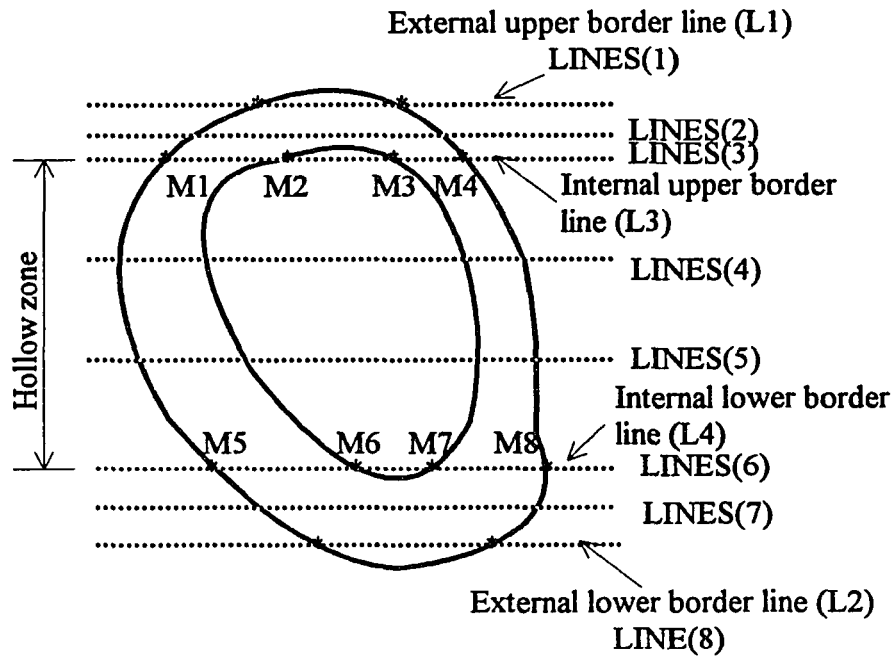


Figure 4.7 Definition of the selected lines in straight searching method.

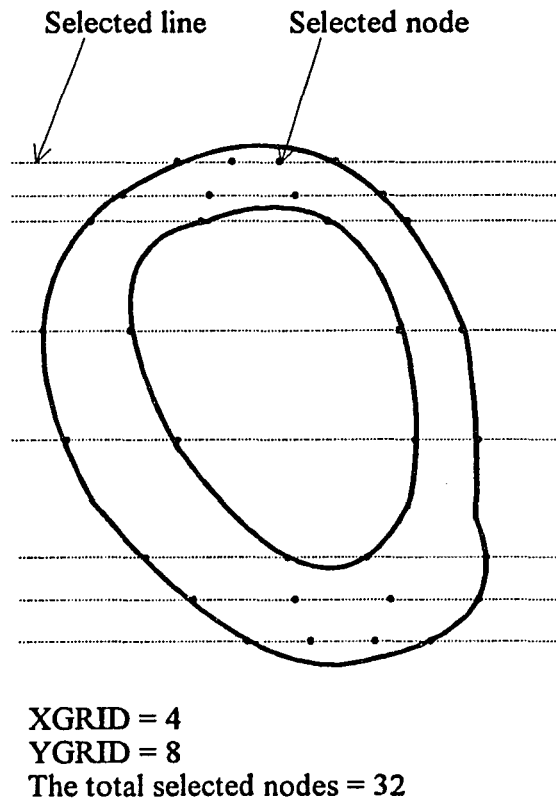


Figure 4.8 Display of selected nodes in straight searching method.

4.4.3.2 Radial Search. A brick element in ANSYS finite element program should not be distorted such that the included angle between two adjacent faces is outside the $90^\circ \pm 45^\circ$ range. Warping occurs when four nodes of a solid element face are not in the same plane. Warping is measured by the relative angle between the normals to the faces at a node. A warning message is printed if warping is beyond a small, but tolerable value. If warping is excessive, an error message is shown and the problem will abort. In order to avoid the warping, it is necessary to select the proper nodes. As mentioned previously, the straight search method may result in warping. Although a routine is developed to adjust the improper nodes and correct the twisted elements, it is necessary to develop a new effective algorithm to replace the straight search method. Therefore, the radial search method is developed and applied to the scanned femur. The details of the radial search method will be explained next.

When the geometric center is found in each cross section, the radial search method can be used to select the nodes in each cross section. Two external and two internal lines are determined by the detection algorithm. Then eight internal border pixels are searched from the two internal lines. The geometric center of hollow zone is determined by the average value of two internal border pixels (M2 and M7 shown in Figure 4.6). The relative line position represents Y coordinate and the relative pixel position is X coordinate. A radial search routine detects the border pixels in the radial direction from the center. The radial selective method is similar to the edge detection routine. The outside and inside borders of the compact bone zone in each cross section are detected and displayed by this routine. Since the compact bone zone is very thin and there is trabecular bone in the proximal end, one CT number is not enough to detect both the internal and external borders of each cross section. Some cross sections therefore need to use the different selected CT numbers in some radial directions. If too high or too low minimum CT numbers are selected, the internal and external borders of compact bone zone can not be detected accurately. Since the density of the compact bone gradually increases distally, the

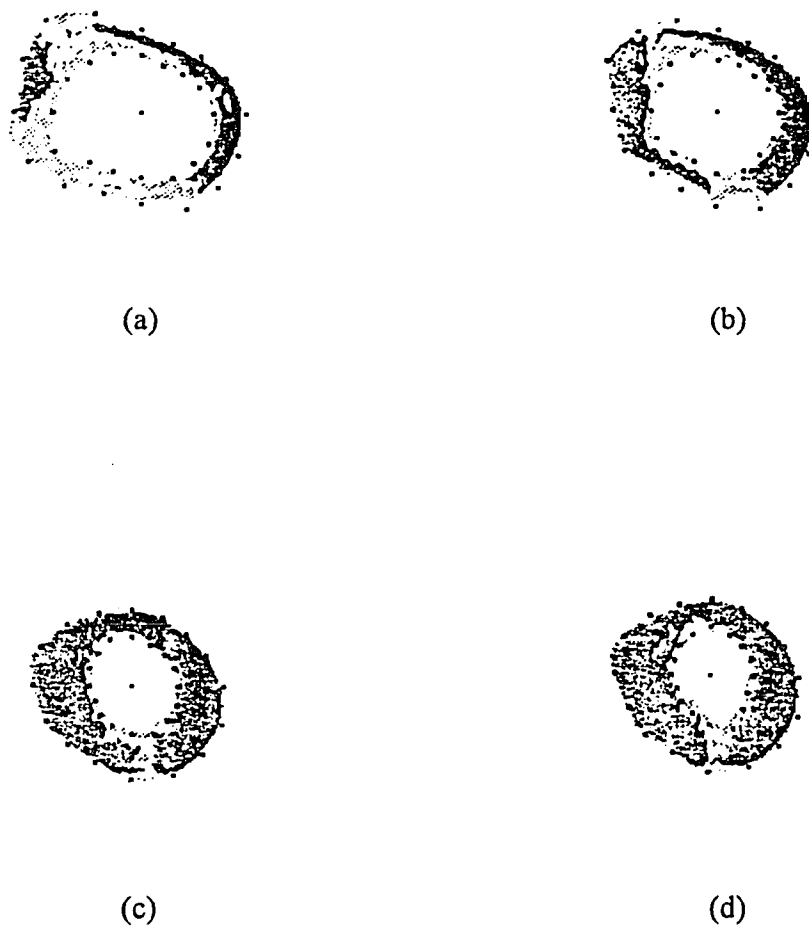


Figure 4.9 The scanned cross sections and the selected nodes in Case 1 for image number (a) 5, (b) 6, (c) 9, and (d) 10.

CT testing number of proximal end should be smaller than that of distal end. By trial and error, the CT number of 1280 to 1400 for proximal end and 1360 to 1500 for distal end was determined. Because of the difference of density between individuals, the CT number should not be the same for every person. The proper CT number can be found by trial and error.

Since the external and internal border pixels are obtained from the radial searching routine, these pixels are also the selected nodes. The other selected nodes can be found between the external border pixel and the internal border pixel. For example, if the dividing number is 2 in 16 radial directions, there are totally 48 selected nodes in the compact bone zone. Figure 4.9 displays the selected nodes in the CT cross sections. Although the more nodes selected can provide more accurate results, too many nodes increase the running time and cost. The number of nodes selected depends on the finite element software limitation and the CPU processing capacity. Due to the limitations in the finite element software and computer system, a total number of 65 selected nodes including compact bone, cancellous bone zones and prosthesis are used in each cross section. There are 17 femoral cross sections and total 1371 nodal points in the finite element model.

4.4.4 The Bone Prosthesis Simulation

Studies of femora reveal the difficulties of achieving anatomic placement with a straight stem design. To achieve long-term anatomic placement, femoral components must (1) fill the canal adequately, (2) preserve the calcar cortical bone (i.e. proximal-medial femoral neck), and (3) be centered in the intramedullary canal. From the manufactures' prosthetic templates and X-ray radiographs of femur-prosthesis, some characteristics can be found to simulate the prosthetic shape. The center axis of the prosthetic stem except proximal side is a straight line in the anterior-posterior (A/P) and medial-lateral (M/L) funnel of the femur, and the center axis of the prosthetic stem in the proximal side is an inclined line

(Figure 4.10). Therefore, a computer routine is developed to simulate the prosthetic stem according to the following procedures.

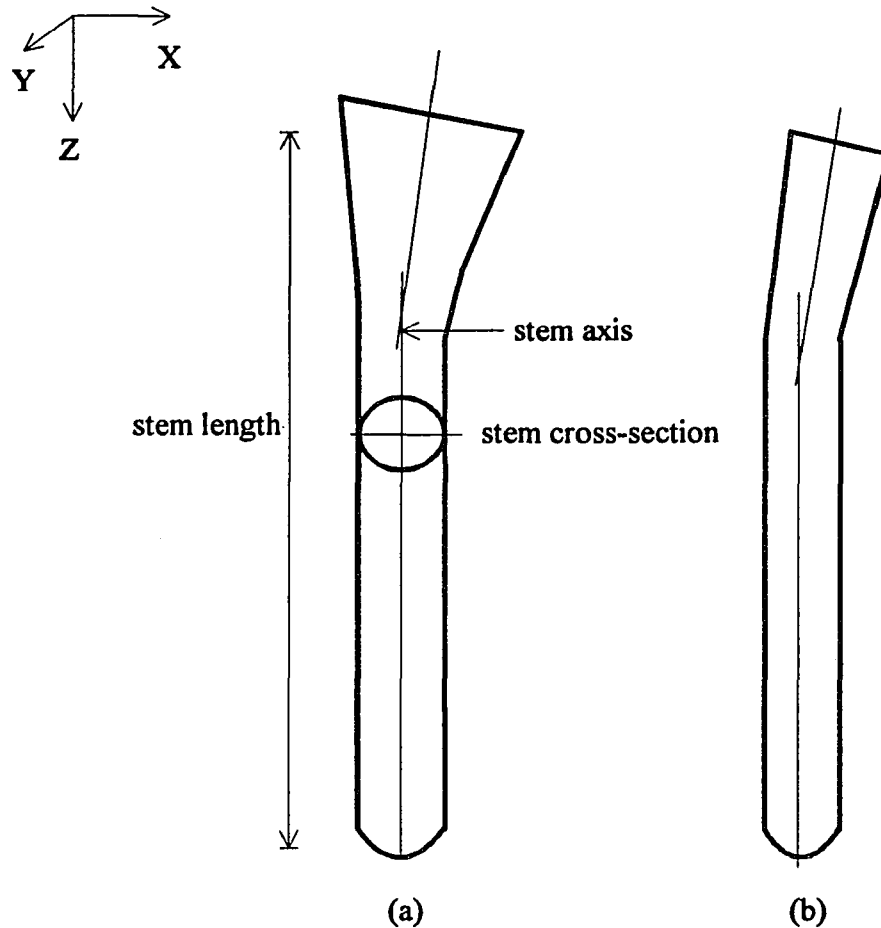


Figure 4.10 The simulated prosthetic hip stem in (a) anterior (b) lateral view.

1. The geometric center of each cross section is obtained by the previous routines. Since the center axis of the prosthetic stem is a straight line on frontal plane (X-Z plane) except for the proximal side, it is necessary to adjust X coordinate of the center point in each cross section with the fixed spacing thickness (fixed Z position). The average value of the center points in the four distal cross sections (cross section #10 through #13) are selected as the X coordinate value of the center axis, since the distal prosthetic stem has intimate contact with the femur at

this point. The X coordinate of the center point in each cross section (#5 through #17) is then adjusted to obtain an average value. The proximal cross sections (#1 and #4) are slightly moved toward the medial side, because the stem cross sections are slightly tapered in the proximal side with the lateral side wider than the medial side. Since the spacing thickness is fixed to represent the Z coordinate, the center axis of cross section #1 through #4 keep an inclined line on frontal plane (X-Z plane) after doing the least-square regression procedure on frontal plane (X-Z plane), and the center axis of cross section #5 through #17 keep a straight line on frontal plane.

2. For Y coordinate position of the center point in cross section, the search method is similar to step (1) to calculate the average Y coordinate of the distal cross sections determining the straight axis of the distal stem. The least-square regression procedure on sagittal plane (Y-Z plane) is used to obtain the regression line from cross section #1 through #4.
3. Since the center point of each cross section is adjusted, the nodes of the cortex are selected by the radial search method from the adjusted center point. The maximum prosthetic stem size can be determined by the distance between the adjusted center point and the cortex. The prosthetic stem can be selected according to the calculated canal size and manufactures' size.

For Case 1 and Case 2 with the same prosthetic stem in the total hip arthroplasty, the selected prosthetic stem sizes are the following (1) stem length: 140 mm, (2) stem thickness: 11 mm for cement model and 15 mm for porous coating model, (3) neck angle: 35°, (4) porous thickness: 1 mm for porous coating model, and (5) cement thickness: 2 mm for cemented model. Figure 4.11 displays the selected nodes of each cross section on which 65 nodes are selected.

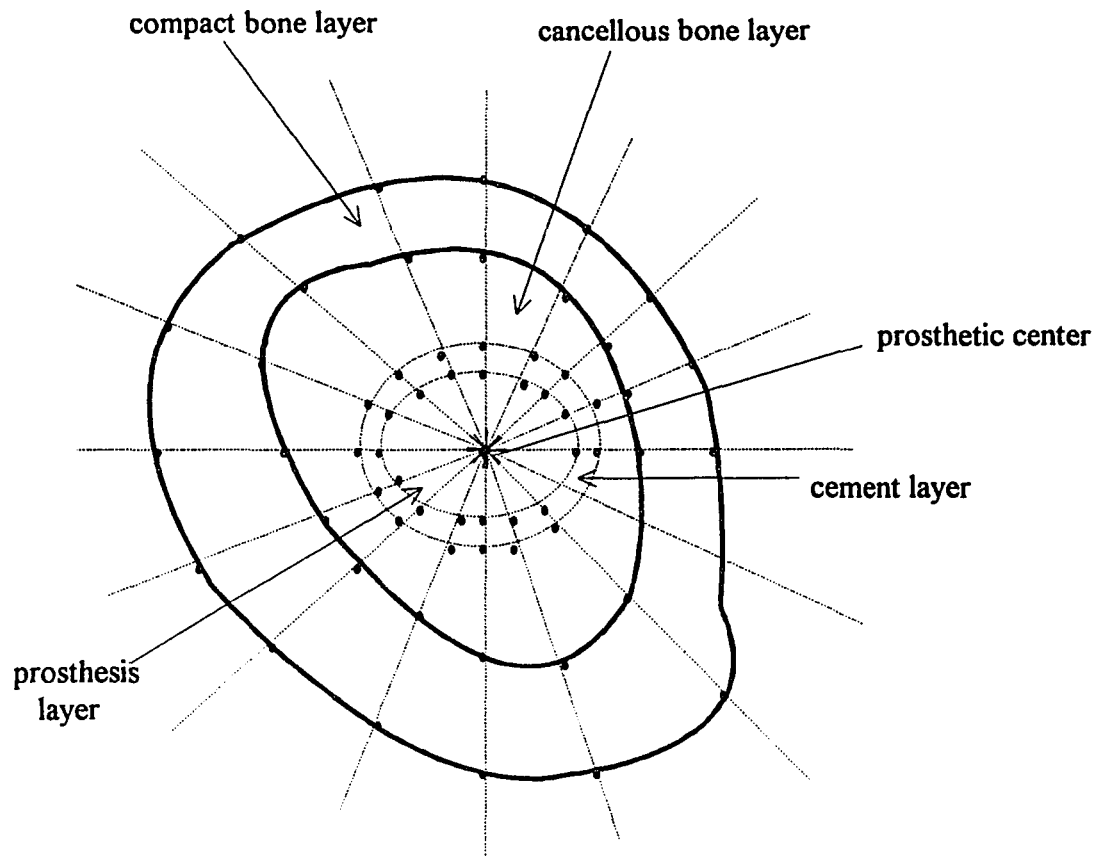


Figure 4.11 Display of selected nodes in each cross section of the femur with prosthesis model.

Because of the irregular shape of the femoral greater trochanter, it is difficult to select node positions and connect two dimensional boundaries constructing the three dimensional greater trochanter. Therefore a rotating routine which makes the selected node rotate 35° about y axis in the most medial node for the selected cross section, is developed to simulate the greater trochanter.

The mathematical expressions are calculated by the transformation matrices. Assuming that the coordinate of the most medial node is (a, b, c) , the transformation procedures are the following:

- (1) Translate to the origin $(0, 0, 0)$ from the position (a, b, c) .
- (2) Rotate θ (35°) about y axis in the origin.
- (3) Translate to the selected node position (a, b, c)

If the position of any selected node in the cross section is (x, y, z) , which is transformed by the composite transformation matrix, the new position (x', y', z') is

$$\begin{bmatrix} x' \\ y' \\ z' \\ 1 \end{bmatrix} = \begin{bmatrix} 1 & 0 & 0 & a \\ 0 & 1 & 0 & b \\ 0 & 0 & 1 & c \\ 0 & 0 & 0 & 1 \end{bmatrix} \begin{bmatrix} \cos \theta & 0 & \sin \theta & 0 \\ 0 & 1 & 0 & 0 \\ -\sin \theta & 0 & \cos \theta & 0 \\ 0 & 0 & 0 & 1 \end{bmatrix} \begin{bmatrix} 1 & 0 & 0 & -a \\ 0 & 1 & 0 & -b \\ 0 & 0 & 1 & -c \\ 0 & 0 & 0 & 1 \end{bmatrix} \begin{bmatrix} x \\ y \\ z \\ 1 \end{bmatrix}$$

$$= \begin{bmatrix} \cos \theta & 0 & \sin \theta & (-a \cos \theta - c \sin \theta + a) \\ 0 & 1 & 0 & 0 \\ -\sin \theta & 0 & \cos \theta & (a \sin \theta - c \cos \theta + c) \\ 0 & 0 & 0 & 1 \end{bmatrix} \begin{bmatrix} x \\ y \\ z \\ 1 \end{bmatrix}$$

$$= \begin{bmatrix} x \cos \theta + z \sin \theta - a \cos \theta - c \sin \theta + a \\ y \\ -x \sin \theta + z \cos \theta + a \sin \theta - c \cos \theta + c \\ 1 \end{bmatrix}$$

The simulated procedures of the greater trochanter layer and the prosthesis neck layer include the designated layer thickness and the applied transformation method. In order to reduce the running time and the complexity, the ball of the prosthesis will not be simulated in the finite element model. The designed model is shown in Figure 4.12.

4.4.5 Mesh Generation

A mesh generator is a set of computer procedures which discretize given object geometry into a finite element model. The mesh is generated in terms of nodes which are defined by their geometrical location in a global Cartesian coordinate system, and by elements which are directly defined by these nodes. The elastic properties needed for creating the stiffness

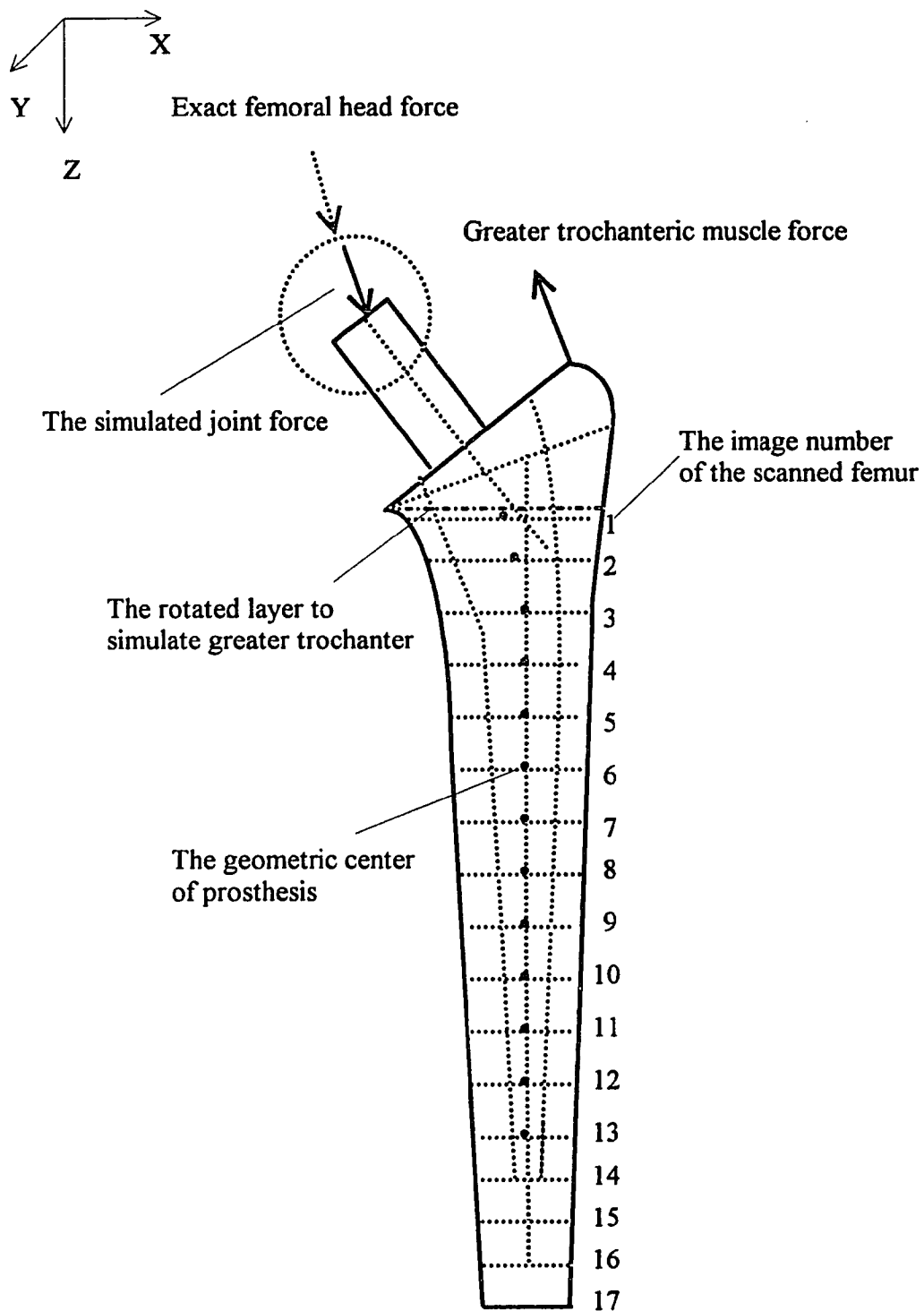


Figure 4.12 An analyzed model of a femur with prosthesis.

matrix in the finite element model are assigned to the model elements by the mesh generator.

The formation of the three-dimensional elements utilizing the two-dimensional mesh of the cross sections is coordinated with the node selection and numbering routine to define three-dimensional eight-node isoparametric elements according to the requirements of the selected finite element program for the stress analysis.

The method of forming the elements is inherent with the node selecting and numbering method described in the previous section, and is done automatically for each two adjacent cross sections. The node selection routine provides a constant number of nodes in each cross section, and therefore insures no free nodes in any cross section after the elements are formed. The element definition algorithm developed takes into account the intrinsic shape of the bone or prosthesis cross sections and the variations of boundary geometry in the adjacent cross sections in order to create a general procedure for the femur and prosthesis modeling.

The element definition routine starts a sequential procedure for the first cross section ($K=1$) to the last cross section ($K = K_{tot}$) in which each adjacent pair $K, K+1$ are utilized to define eight-node elements by the following procedures:

1. Four nodes of cross section K are $N(1)$, $N(2)$, $N(3)$, and $N(4)$ connected to the four nodes of the cross section $K+1$, which are $N(5)$, $N(6)$, $N(7)$ and $N(8)$.
2. The eight nodes of each element have eight different positions for the bone and cement parts in the radial selective routine. Since the element shape is triangular for the prosthesis part in the radial selective method, the $N(3)$ and $N(4)$ share the same point, and the $N(7)$ coincides with $N(8)$. The $N(1)$ is the geometric center point of the prosthesis, and $N(3)$, $N(4)$ are the boundary points for the prosthesis part. Figure 4.13 shows the general connecting element and the element connection of bone prosthesis for a radial selecting method.

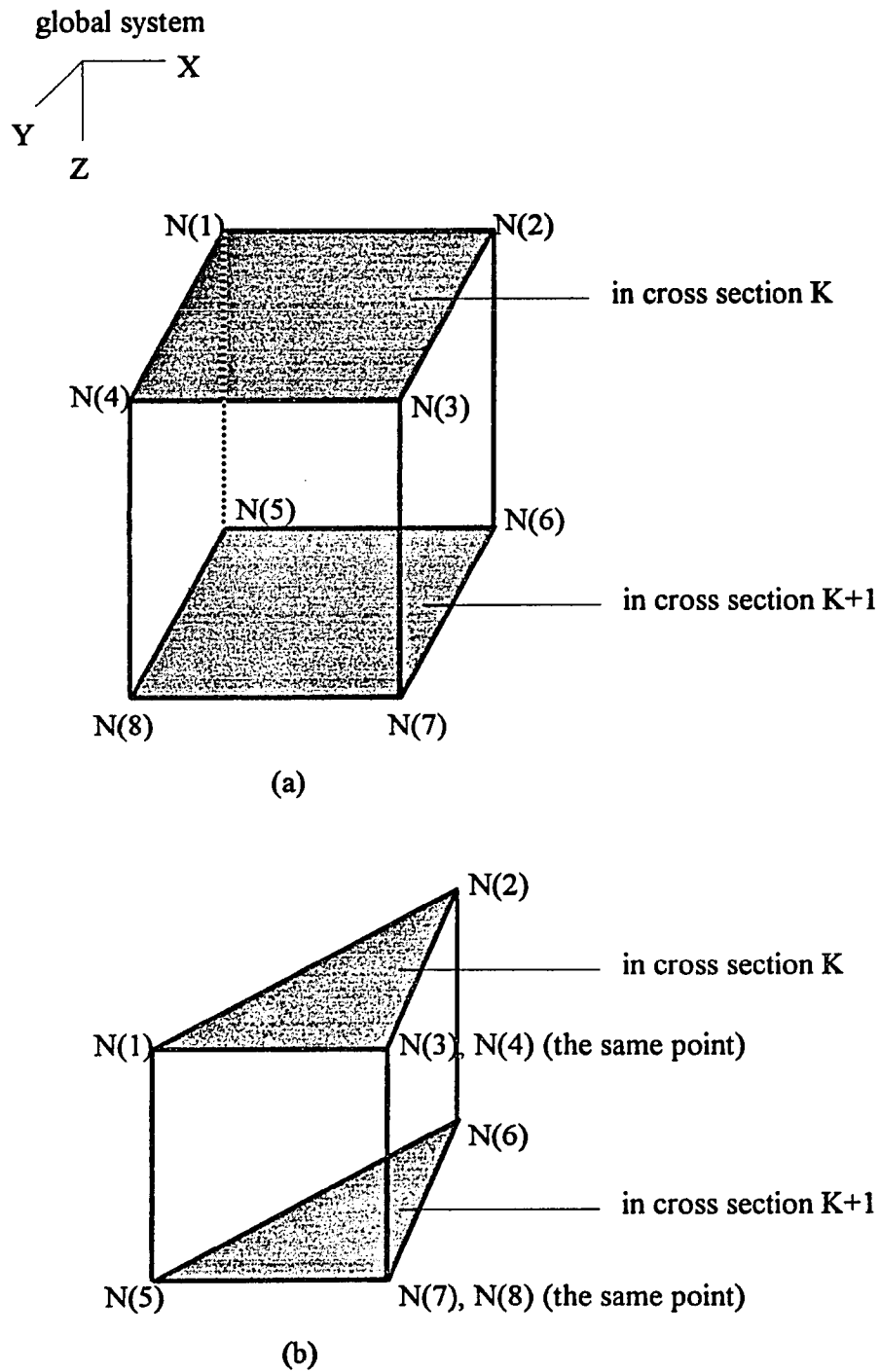


Figure 4.13 (a) The element definition of a brick-type element. (b) The element definition for the prosthesis part of radial node selecting routine.

3. NE represents the element numbers assigned sequentially to each element. The total numbers of NE are:

$$NE = (K_{tot}-1) (Y_{no}-1) (X_{no}-1)$$

where K_{tot} = the total cross section

X_{no} = the node numbers of each searching line

Y_{no} = the total search lines

4. The ordering of the elements and nodes is assigned according to the "one sweep" definition which will be explained in the next description.

To reduce the maximum wave front size, the elements must be ordered for the solution phase so that the element for which each node is mentioned first is as close in sequence to the element for which it is mentioned last. In geometric terms, the elements should be ordered so that the wave front sweeps through the model continuously from one end to the other in the direction which has the largest number of nodes. For example, consider a rectangular model having six nodes in one direction and 20 nodes in the other direction. The elements should be ordered along one six-node edge and progress toward the other twenty-node edge. In this way, equations will be deleted from the assembled matrix as soon as possible after they are added, thus minimizing the wave front size. All elements, including those of different types, should be included in the "one sweep" definition.

4.4.6 Elastic Properties Definition

Since the three-dimensional elements are defined, it is necessary to assign the elastic modulus and Poisson's ratio to each element in the model. Recent investigations provide an empirical relationship between the elastic modulus of the cortical bone in compression and the bone apparent density. Therefore the empirical formula can be used to determine the elastic modulus of the cortical bone from the mean CT number of each single element. Because the cancellous bone with a wide range density is more complicated than the

cortical bone, the empirical relationship is not very reliable for the cancellous bone. In this study, the elastic modulus of the cortical bone is determined by the empirical formula. All other elastic properties are obtained from the literature (Brown et al., 1988; Cowin, 1989; Ducheyne and Hasting, 1984; Huiskes and Boeklagen, 1989; Mann et al., 1991; Mihalko et al., 1992; Rohlmann et al., 1988; Weinans et al., 1990). Linear isotropy is assumed for all materials in the model. The material properties of the femoral bone and prosthesis are tabulated (Table 4.2). The average CT number obtained from the pixel data is used to determine the elastic modulus for each element of cortical bone. In order to determine the elastic modulus of each element, the relationship between the elastic modulus and apparent density is required.

Table 4.2 Material properties for each material region of the femur and prosthesis.

Material	Elastic Modulus (MPa)	Poisson's Ratio
Cortical bone	$E = 3790(\dot{\epsilon})^{0.06} \rho^3$	0.30
Cancellous bone	1,000	0.30
Cement (PMMA)	2,000	0.33
Prosthesis (Co-Cr alloy)	200,000	0.29
Prosthesis (Titanium)	100,000	0.29
Porous-coated layer	4,200	0.29

The literature contains a number of reports of experimental data on the relationship between apparent density and elastic modulus for bone tissue. The paper of Carter and Hayes (1977) reported the results of compression test on human and bovine bone specimens and, employing also the data of Wright and Hayes (1976), developed an empirical relationship for the dependence of the longitudinal elastic modulus upon apparent density. Carter and Hayes (1977) concluded that the axial elastic modulus E depend upon the apparent density to the third power and the strain rate $\dot{\epsilon}$ to the 0.06 power; thus, E in MPa was given by

$$E = 3790(\dot{\epsilon})^{0.06} \rho^3$$

where ρ is in g/cm^3 and $\dot{\epsilon}$ is in inverse seconds. The relationship is called the combined data relationship in this situation, because the data upon which it is based depend upon both bovine and human cancellous bone data and bovine and human cortical bone data. The inclusion of cortical bone as a datum in a relationship between cancellous bone and apparent density is based on the suggestion of Wolff that cortical or compact bone is simply more dense cancellous bone. The inclusion of the data for two species has the advantage of giving a wider data base for determining a relationship.

The empirical relationship is used in this study to obtain the elastic modulus of each element in the cortical bone when the average apparent density of each element in the cortical bone is calculated from the pixel data. The strain rate to which bone is normally subjected ranges from 0.001 s^{-1} for slow walking to 0.01 s^{-1} for vigorous activity (Cowin, 1989; Linde et al., 1991; Martens et al., 1983; Rohl et al., 1991). Therefore, 0.01 s^{-1} for the specific strain rate is selected to obtain the elastic modulus in this study. Since the strain rate is defined and apparent density is calculated from the pixel data, the elastic modulus of each element in the cortical bone is determined by the empirical relationship.

Each CT image of the scanned bone in each cross section is composed of pixels where the CT numbers can be used to determine densities. Since the mean CT number of each three-dimensional element can be obtained by calculation, a linear relationship will be used to determine the average apparent density of each element. Then an empirical formula developed by Carter et al. (1977) between the apparent density and the bone elastic modulus is used to determine the average elastic moduli of the elements for the cortical bone.

4.4.6.1 Radiographic Density-Apparent Density Relationship. The apparent density of a material is its mass per unit volume. The density of human cortical bone ranges from 1.7 to 2.0 g/cm^3 . Normal human cortical bone has a density of approximately 1.9 g/cm^3 . The

porous structure of cancellous bone presents a situation in which two different densities are in each pixel, the density of the trabecular bone material, and the density of the cancellous structure. The density of trabecular material is similar to that of cortical bone and ranges from 1.6 to 1.9 g/cm³, and the porosity of trabecular material affects the material density. The density of the cancellous structure ranges from 0.15 to 1.0 g/cm³ (Ashman et al., 1984; Bensusan et al., 1983; Cowin, 1989; Rice et al., 1988). Since the cancellous bone has a wide range of apparent density, it is difficult to find the correlation between radiographic density (CT number) and apparent density. The published literature does not contain much information about this topic.

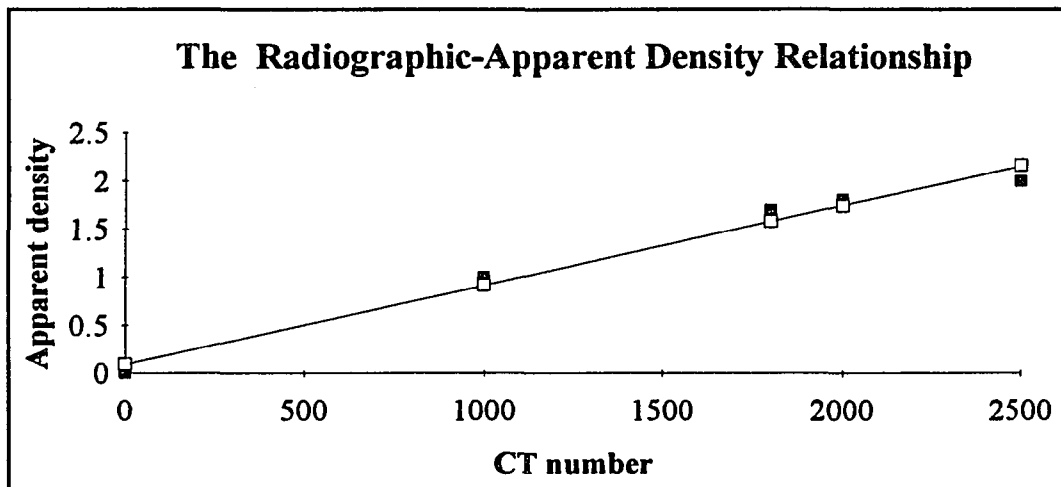


Figure 4.14 The correlation between radiographic density and apparent density.

Since different CT scanners have different CT scales, the relationship between the radiographic density and the apparent density is valid only for a specific CT file. In this study, each cross sectional image is examined individually to establish the radiographic-apparent density relationship. After examining the CT images and reviewing the literature (Brown et al., 1988; Cowin, 1989; Currey, 1988; Ducheyne and Hasting, 1984; Fung, 1981; Hvid et al., 1989; Huiskes and Boeklagen, 1989; Linde et al., 1991; Martens et al., 1986; Martin, 1991; Rice et al., 1988; Robertson and Huang, 1984; Schaffler et al., 1988),

five data points are taken as the reference points which have their corresponding elastic modulus at different bone positions. The empirical relationship is applied to determine the apparent densities and the relative CT numbers of these five data points are obtained by averaging the CT numbers of three hundred pixels at the corresponding bone positions. The coefficients of the desired linear relationship are obtained by applying a linear regression method on these data points. Figure 4.14 shows the correlation between radiographic density and apparent density.

The linear radiographic-apparent densities relationship which allows the calculation of the density for each pixel is:

$$\rho = (A) \cdot (CTD) + B$$

The coefficients of the relationship determined by the linear regression method are:

$$A = 8.272 \times 10^{-4} \quad B = 0.092$$

where ρ is the apparent density and CTD is the radiographic density.

4.4.6.2 Calculation of Elastic Modulus in The Cortical Bone Element. The average elastic modulus assigned to the model element in this study is derived from the radiographic densities of all the pixels bounded within the element's borders. The method of element generation is to connect two two-dimensional elements creating an eight-node three-dimensional element. The pixel information in these two-dimensional elements is used to calculate the average density of each three-dimensional element. The average elastic modulus is then calculated for each element using Carter and Hayes relationship.

For each 2D element, the mean value of radiographic density is determined by dividing the summation of the CT numbers of the pixels within each element by total pixel numbers. The applied procedures include the following:

1. An two-dimensional element (Figure 4.15) consists of two triangles and one trapezoid.

2. Each two-dimensional element consists of four nodes which are detected to determine the node order (N(1), N(2), N(3), and N(4)) according to the relative line number.
3. Two reference points are detected and their nodal position is determined from the position of N(2) and N(3). N(A) is located on the straight line of N(1) and N(3). N(B) is located on the straight line of N(2) and N(4).
4. Since each two-dimensional element is divided into two triangles and one trapezoid, the pixels are searched and calculated line by line within the triangular and trapezoid area. The total CT numbers and pixel numbers are obtained by summing the CT numbers and pixel numbers of the pixels within the triangular and trapezoid area.
5. The mean CT number of a two-dimensional element is determined by dividing the summation of the total CT numbers by the total pixel numbers.

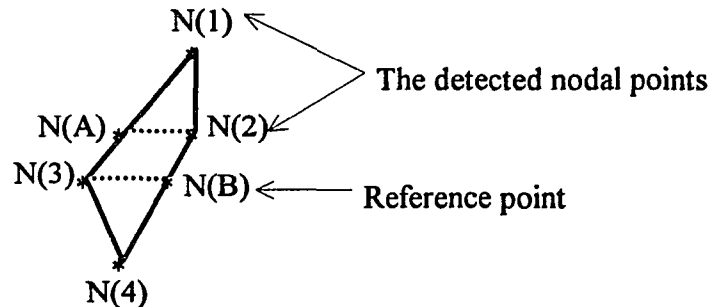


Figure 4.15 A two dimensional element consists of two triangles and one trapezoid.

In this Case 1, the calculated smallest average elastic modulus obtained for an element is 4939 MPa occurred in the most proximal-lateral side and the largest is 22683 MPa occurred in the most distal-lateral side. The calculated elastic modulus is close to the value in the published literature. Therefore, the developed method to determine the elastic modulus is valid for the stress analysis of the femur with a prosthesis.

4.4.7 Loading and Boundary Conditions

Published data (Burke et al., 1990; Davy et al., 1988) is used to define the joint contact forces, and the muscle forces during gait. Burke et al. (1990) used a telemeterized total hip prosthesis implanted in a patient and force-data were obtained by strain-gauges. The 1460 N compressive load, approximately 2.6 times body weight, on the prosthesis head in gait simulation has compressive forces of 500 N, 153 N, and 1346 N in the x, y, and z coordinates of the mesh, respectively. The 800 N tensile load on the greater trochanter has components of -382 N, -117 N, and -784 N in the x, y, and z coordinates of the mesh, respectively. The forces on the prosthesis head and greater trochanter were applied 20° medial of the central axis and 15° anterior of the mid-frontal plane (Figure 4.16). These loads are relevant to a patient weighing approximately 120 lbs.

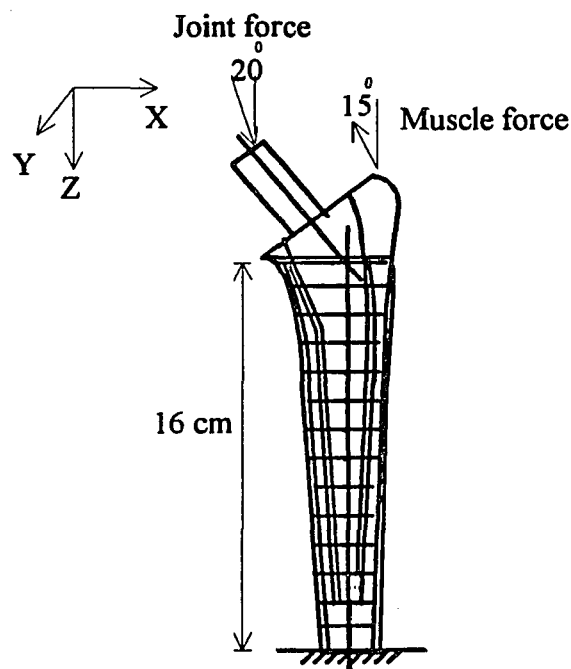


Figure 4.16 Coordinate system and loading conditions of the femur with prosthesis.

In this study the patient's weight is assumed to be 154 lbs and the joint force scales directly with body weight. Therefore, the 1874 N compressive load on the prosthesis head at a point 20° medial of the central axis generates components in the mesh coordinate system of 642 N, 196 N, and 1750 N in the x, y, and z directions, respectively. The muscle

forces, 15° anterior of the mid-frontal plane as one resultant load of 1026 N tensile load with components of -490 N, -150 N, and -1006 N in the x, y, and z coordinates of the mesh, applied at the greater trochanter are divided over six-node area. The boundary conditions consisted of prescribed zero displacements along the lower edge of the most distal row of elements (bone length: 160 mm).

4.4.8 Generating the Finite Element Model

4.4.8.1 The Uniform Cylinder Model. A geometrically uniform cylinder with prosthesis model consisting of 1264 eight-node brick elements and 1371 nodal points (4113 degrees of freedom) is created. A linear, homogeneous and isotropic model with an elliptic cross section, long axial diameter of 60 mm, short axial diameter of 40 mm, thickness of 6 mm and total length of 160 mm is used to simulate the femoral bone. The cross sectional dimensions of the uniform cylinder are determined according to the CT scan and radiograph examination, and published data (Rubin et al., 1992). The proximal part of the uniform cylinder is also modeled by the rotating routine mentioned in the previous section. The prosthetic stem is assumed to be the cross section of an elliptic shape with a 140 mm stem length and 44 mm neck length. The thickness of the cement layer is 2 mm. All prosthesis design parameters and the boundary conditions applied on the uniform cylinder model are the same as that of the model created by CT data except the bone shape and mechanical properties. The uniform cylinder model is assumed to be uniform and the mechanical properties in cortical bone ($E = 17000 \text{ MPa}$, $\nu = 0.3$) and in cancellous bone ($E = 1000 \text{ MPa}$, $\nu = 0.3$) are determined according to published data (Currey, 1988; 1984; Fung, 1981; Hvid et al., 1989; Huiskes and Boeklagen, 1989; Linde et al., 1991; Martens et al., 1986; Martin, 1991). The stress patterns of the uniform cylinder model are calculated to determine the influence of the bone geometry. Figure 4.17 displays the uniform cylinder three-dimensional finite element model.

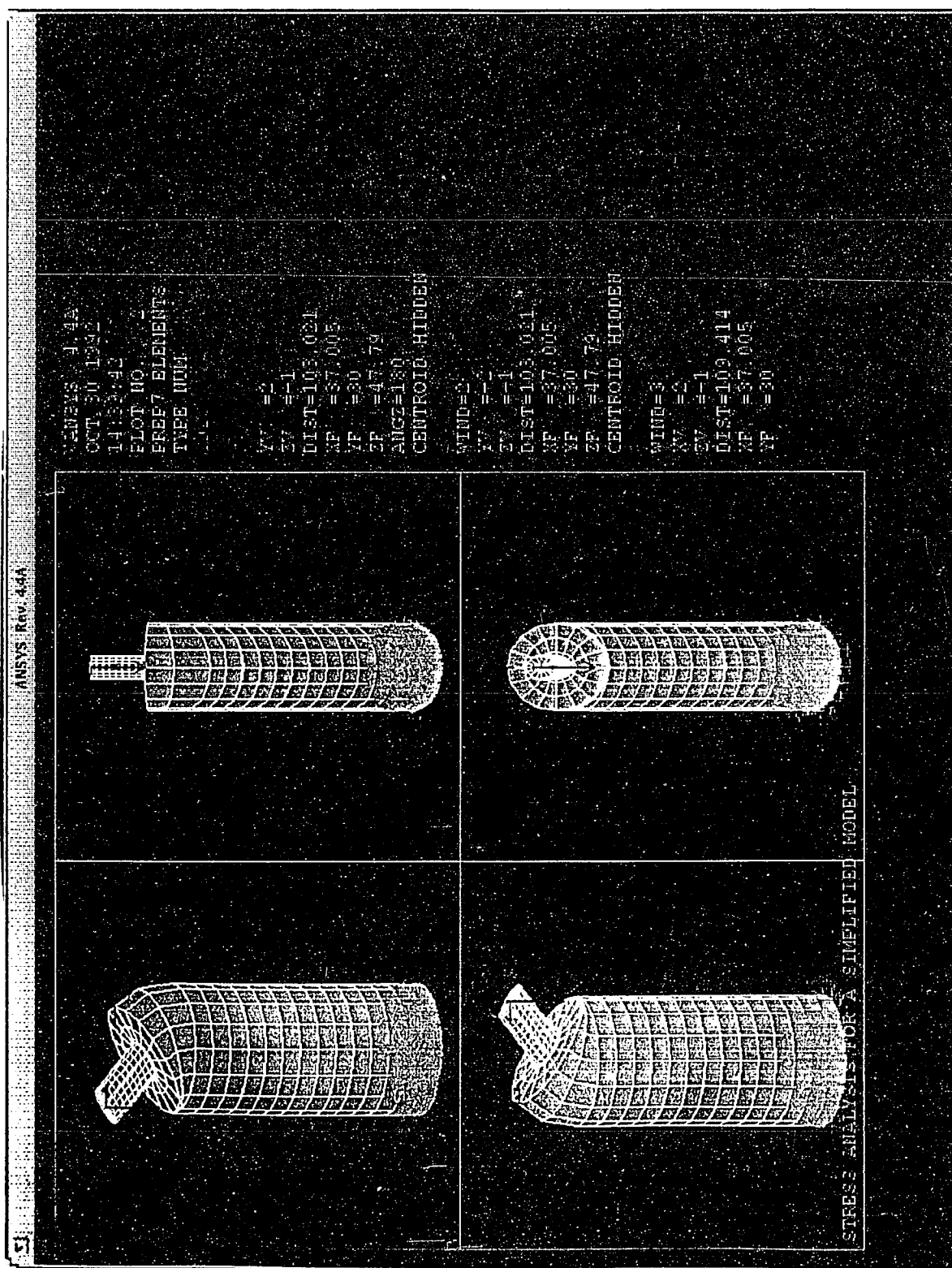


Figure 4.17 The 3-D finite element model of a uniform cylinder with prosthesis.

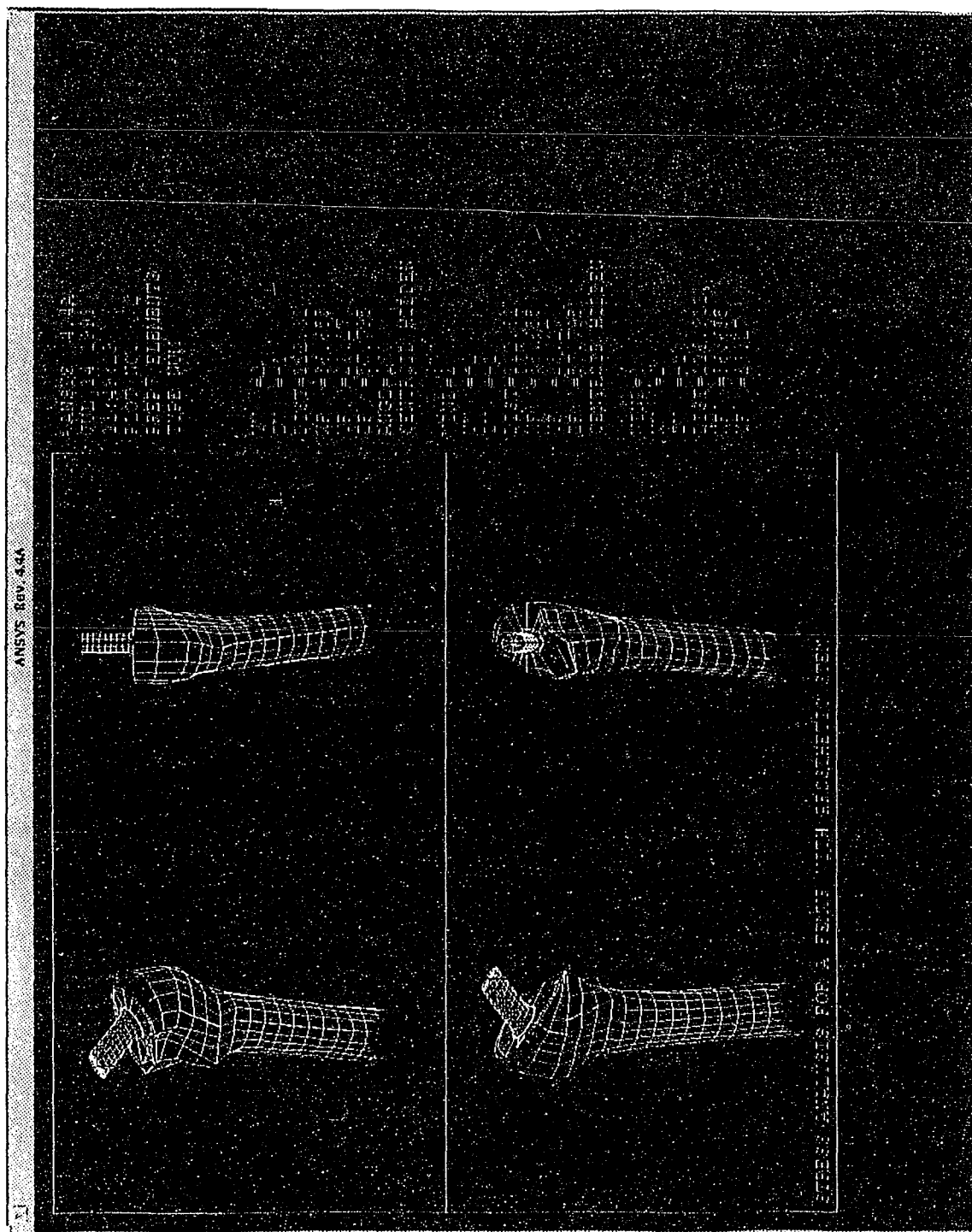


Figure 4.18 The 3-D finite element model of Case 1 with prosthesis generated by CT data.

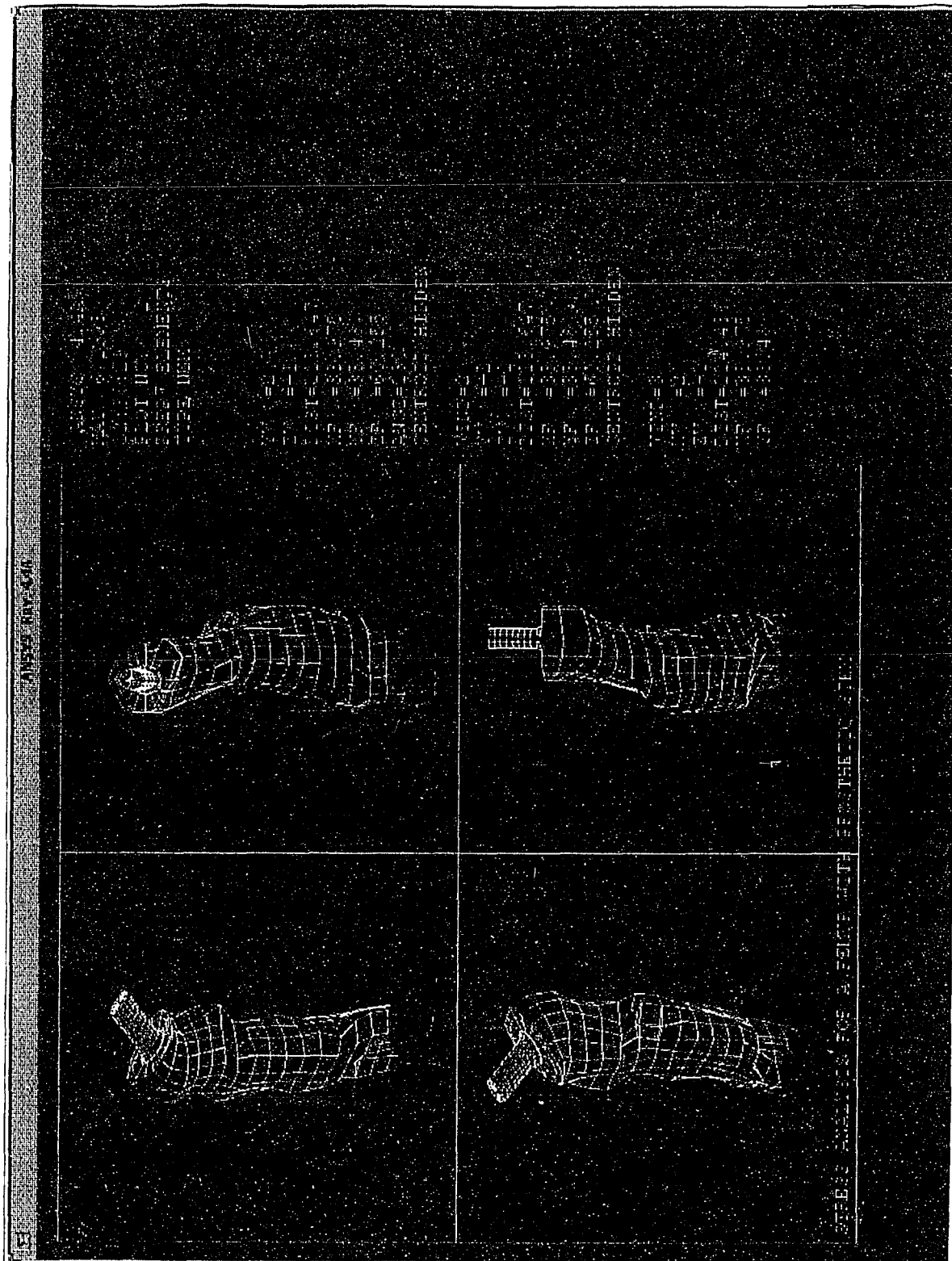


Figure 4.19 The 3-D finite element model of Case 3 with prosthesis generated by CT data.

4.4.8.2 The CT data Model. The finite element model generated in this study yields a 160 mm length of femoral bone starting 15 mm below the femoral head. The greater trochanter is modeled by the developed rotating routine. The prosthesis design parameters include: the neck length of 44 mm, the stem length of 140 mm, the neck angle of 35° and the cement layer of 2 mm. The cement layer could be replaced with the porous coating layer to simulate the porous coating prosthesis design. The finite element model (Figure 4.18) consists of 1264 eight-node brick elements and 1371 nodal points for the standard femoral shape (Case 1). The finite element model (Figure 4.19) is also generated for Case 3 (the fractured femoral shape) in order to study the stress patterns of this special case. The linear and isotropic model is created for the ANSYS finite element program executed on a SUN 4/300 color workstation. The typical CPU time required per run is approximately 2 hours.

4.5 Model Verification

In order to verify the results of the stress data generated in the CT finite element model, a sample calculation is performed. The femoral geometric dimensions and loading conditions (see Section 4.4.7) in the sample calculations are the same as that of the CT data model. The cross section of a femoral diaphysis is assumed as a round cross section and the geometric dimensions are determined according to the CT data. Figure 4.20 displays the geometric dimensions and loading conditions of the femoral model and the selected cross section of a femoral diaphysis. The material elastic properties of the prosthetic stem are taken as the cancellous bone properties to calculate the stress patterns of the normal intact femur. The stress patterns of the normal intact femur calculated by the finite element method shown in Appendix A3 and A6 are used to do the comparison with the calculation of the elastic theory.

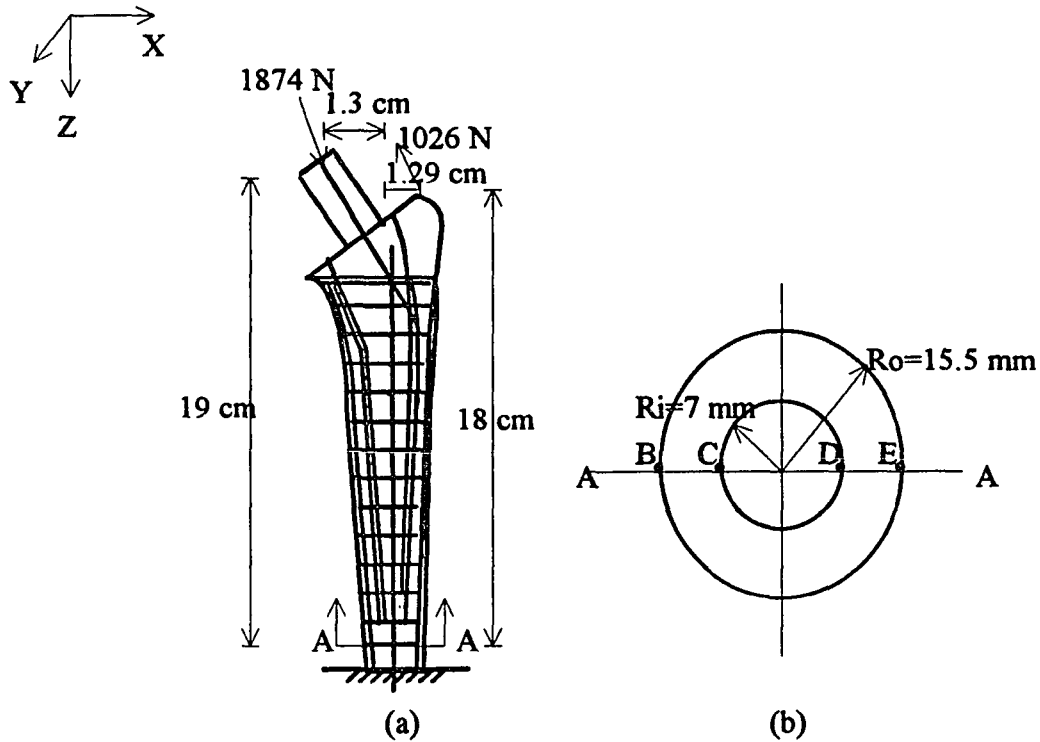


Figure 4.20 (a) External loads acting at the femur and the femoral geometric dimensions. (b) The geometric dimensions in a cross section of a femoral diaphysis.

For a specific cross section of the femoral diaphysis, the radii of the outside and inside boundaries are 15.5 mm and 7 mm respectively. The area and the moment of inertia of the cross section are calculated as follows:

$$A = \pi(R_o^2 - R_i^2) = \pi[(15.5)^2 - (7)^2] = 600.8 \text{ mm}^2$$

$$I = \frac{\pi}{4}(R_o^4 - R_i^4) = \frac{\pi}{4}[(15.5)^4 - (7)^4] = 43447.5 \text{ mm}^4$$

The sum of the bending moments can be calculated as follows:

$$M_y = (500 \times 190) - (382 \times 180) + (1346 \times 13) - (784 \times 12.9) = 33624.4 \text{ Nmm}$$

The sum of the axial forces in the longitudinal direction (Z axis) is as follows:

$$P = 1346 - 784 = 562 \text{ N (compressive)}$$

The axial direct stresses generated by the bending moments and the axial forces in the longitudinal direction (Z axis) at point B, C, D, and E are as follows:

$$\sigma_z = \frac{P}{A} + \frac{M_y x}{I}$$

$$\sigma_{z,B} = \left(\frac{562}{600.8}\right) + \left(\frac{33624.4}{43447.5}\right) \times 15.5 = 12.94 \text{ MPa (compressive)}$$

$$\sigma_{z,C} = \left(\frac{562}{600.8}\right) + \left(\frac{33624.4}{43447.5}\right) \times 7.0 = 6.35 \text{ MPa (compressive)}$$

$$\sigma_{z,D} = -\left(\frac{562}{600.8}\right) + \left(\frac{33624.4}{43447.5}\right) \times 7.0 = 4.48 \text{ MPa (tensile)}$$

$$\sigma_{z,E} = -\left(\frac{562}{600.8}\right) + \left(\frac{33624.4}{43447.5}\right) \times 15.5 = 11.06 \text{ MPa (tensile)}$$

Based on the results of elastic theory and finite element method, the error percentage is defined as follows:

$$\text{error}\% = ((\text{finite element method} - \text{elastic theory}) / (\text{elastic theory})) (100\%)$$

$$\text{error}\% (\text{point B}) = 13.68\% \quad \text{error}\% (\text{point C}) = 8.34\%$$

$$\text{error}\% (\text{point D}) = 20.01\% \quad \text{error}\% (\text{point E}) = 8.50\%$$

Table 4.3 The comparison of calculated results between the elastic theory and the finite element method.

	Theory	Finite element	error %
$\sigma_{z,B}$ (MPa)	-12.94	-11.17	13.68%
$\sigma_{z,C}$ (MPa)	-6.35	-5.82	8.34%
$\sigma_{z,D}$ (MPa)	4.48	5.38	20.01%
$\sigma_{z,E}$ (MPa)	11.06	12.00	8.50%

Since a specific cross section of the femoral diaphysis assumed to be circular in the calculation of the elastic theory differs from the exact cross section, precise agreement of specific stress component magnitudes is not to be expected. The results for the elastic theory and for the finite element method are tabulated (Table 4.3). The comparison of the stresses which are calculated for the same model by the elastic theory and by the finite element method shows reasonable agreement.

CHAPTER 5

RESULTS AND DISCUSSION

5.1 Stress Analysis of the femur with a Prosthesis at Preoperation

In this study analysis of the stress in a femur with a prosthesis interface involved (1) load transfer in the cemented and porous coating femur-prosthesis, (2) the difference between a CT generated model and a simplified cylinder model for a cemented femur-prosthesis, (3) the difference due to stem material (cobalt-chromium alloy versus titanium), (4) the effect of stiffness (elastic modulus) and Poisson's ratio of the porous coating layer, (5) the difference due to stress patterns between normal shape femur (Case 1, 2) and fractured femur (Case 3), (6) the comparison of stress patterns between a male femur (Case 1) and a female femur (Case 2), and (7) the changes after postoperative bone remodeling. The interface stresses between the cement, metal and bone are of particular interest because of the problem of clinical loosening of the femoral component. In order to analyze the above conditions the detailed stress distributions are plotted along the interface between the cement and bone, at the prosthetic stem surface and at the femoral surface (Appendix A). The calculated stresses σ_x , σ_y , and σ_z and the shear stresses τ_{xy} , τ_{yz} , τ_{zx} depend upon the position of the femur with respect to the prosthetic stem to the coordinate system chosen (Figure 5.1). Three mutually perpendicular principal stresses (s_1 , s_2 , s_3) can be calculated from the normal and shear stresses. The principal stress is independent of the orientation of the coordinate system. The maximum shear stress ($=0.5 \times (s_1 - s_3)$), and the von Mises stress ($=\sqrt{0.5 \times [(s_1 - s_2)^2 + (s_2 - s_3)^2 + (s_3 - s_1)^2]}$) can also be calculated from the three principal stresses. In the graphic presentation (Appendix A), the longitudinal normal stress, maximum shear stress and von Mises stress are plotted to show the stress distributions at the interface and femoral surface.

A cylinder model of bone with cemented metal prosthetic stem is used to enhance the understanding of stress analysis for the femur with prosthesis. Two loading cases are

considered. Direction and magnitudes are taken from standard single legged stance study. The loading conditions are hip joint force only (case 1), and the combination of hip joint force and muscle force (case 2) respectively. For case 1, the force which produces the bending moments and the axial force generates axial direct stress in the longitudinal direction (Z axis). Figure 5.2 shows the stress of the uniform cylinder with cemented stem in loading case 1. The predominant effect of the load is bending, generating compressive stresses on the medial surfaces, and tensile stresses on the lateral surfaces in the longitudinal direction. The higher interface stresses between stem and cylinder on the proximal and distal sides are similar to the stress patterns along the cylinder surface. The stem is also loaded predominantly in bending, with longitudinal compression along its medial faces and tension along its lateral face. The medial compressive stress values decrease distally. The tensile bending stress pattern on the lateral side is similar, with the maximum tensile stress about 24 MPa, which is lower than the compression (70 MPa) on the medial side.

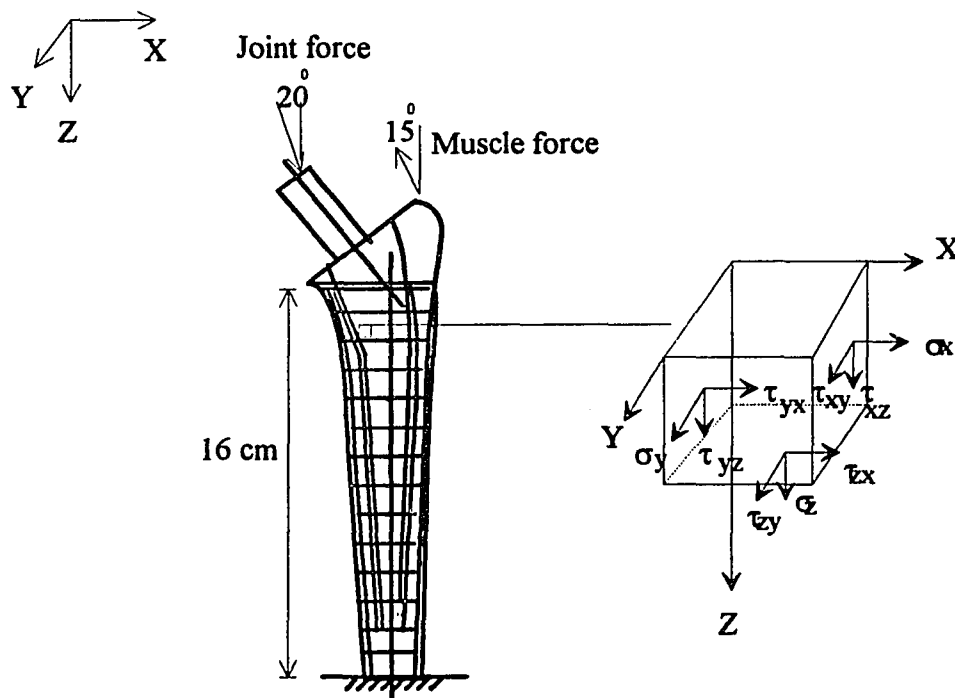


Figure 5.1 Characterization of 3-D stress state at a geometric point of the femur with prosthesis model.

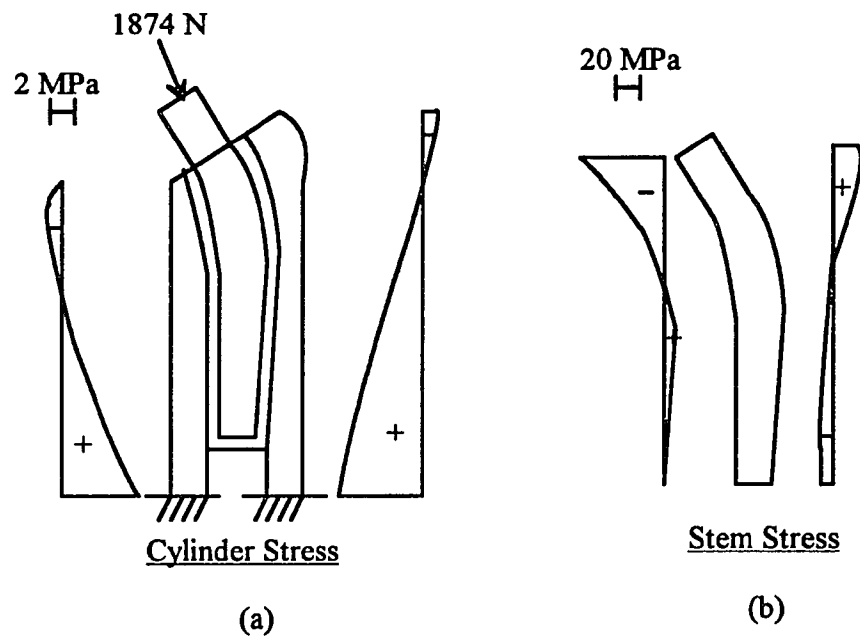


Figure 5.2 The hip joint force acting on an uniform cylinder with cemented stem. (a) The longitudinal stress distribution along the cylinder surface. (b) The longitudinal stress distribution along the metal stem.

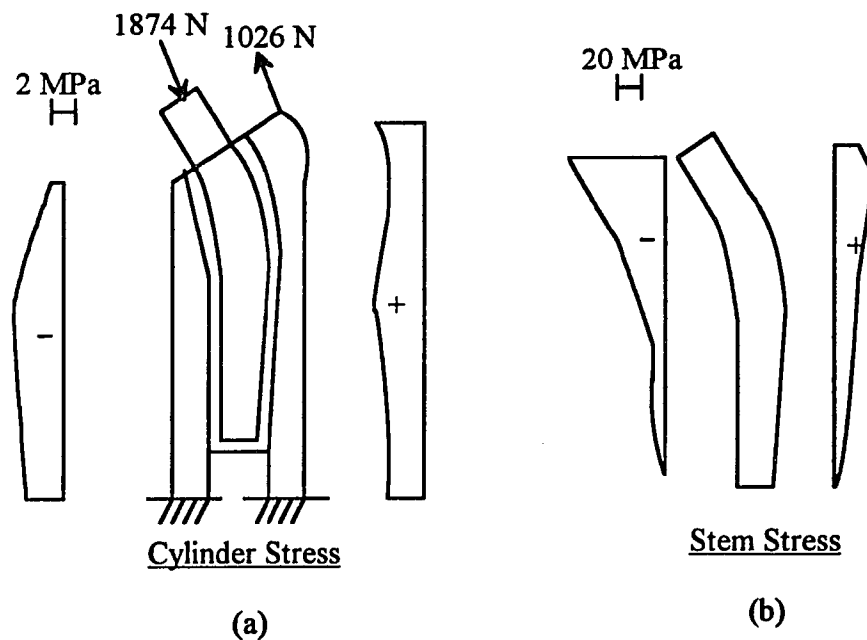


Figure 5.3 The hip joint force and the muscle force acting on an uniform cylinder with cemented stem. (a) The longitudinal stress distribution along the cylinder surface. (b) The longitudinal stress distribution along the metal stem.

When the external forces are a combination of hip joint force and muscle force, the bending effect increases. Figure 5.3 shows the stress patterns of the uniform cylinder with cemented stem in loading case 2. Almost all stress values increase. The maximum medial compressive stress in the stem due to bending increases from 70 MPa to 87 MPa, and the maximum lateral tensile stress increase from 24 MPa to 38 MPa. Proximal interface stresses increase by factors of two to four. Due to the metal stem, higher stresses between stem and cylinder occur both proximally and distally. From the stress patterns, it can be seen that the metal stem carries most of the load and the cylinder is subjected to reduced stress. The muscle force indicates an increased stress of about 40%.

Case 1 (a male femur) is analyzed to determine the effect of the prosthetic material and fixation. Material chosen was cobalt-chromium alloy and titanium alloy. The prosthetic fixation chosen was cemented and porous-coated fixation. Appendix A1 and Appendix A4 display the corresponding stress distributions on the surface of the prosthetic stem. Failure of the interface between prosthesis and bone is a common clinical problem. The maximum compressive stress on the surface of prosthetic stem occurs at the proximal-medial side. The maximum compressive stress of cemented (54.48 MPa) and porous coating (47.51 MPa) models are lower than that of the simplified cylinder model (87.63 MPa). The titanium alloy stem has an average interface stress which is approximately 60% of Co-Cr alloy stem, but the maximum compressive stress is almost the same in the proximal medial region. The stress distribution of the simplified cylinder model gradually increases proximally along the medial side of the prosthetic stem, but the stress distributions of the cemented and porous coating models show the stress increased irregularly. Due to more distal load transfer, the porous coating model indicated a reduced proximal stem compressive stress of about 20%.

The stress distribution within the prosthetic stem laterally is tensile and increases proximally. The magnitude of this stress is 70% of the medial compressive stress along the prosthetic stem. The average stress of the simplified cylinder model is about 40% lower

than the CT generated model, and the stress distributions appear to be very regular. Therefore, it can be concluded that the model geometry and material properties significantly influence the results. The titanium alloy stem, with a Young's modulus one half that of Co-Cr alloy, reduced stem stress about 30%. From the stress patterns it can be seen that the higher stresses in the stem always occur in the distal one third and the proximal side.

The bond between metal and cement is of interest because failure of the bond may result in failure of the total hip replacement (Hampton et al., 1980; Harrigan et al., 1992; Huiskes, 1990; Mann et al., 1991; Rubin et al., 1993; Weinans et al., 1990). From the results of the stress distributions, the tensile stresses on the lateral interface of the distal one third and the lateral-proximal side are more likely to result in rupture of the bond. The normal tensile stress, maximum shear stress and von Mises stress of the proximal side of lateral boundary are 23.44, 18.70, and 35.11 MPa respectively. These are high when compared to the failure stresses of the bone and cement (see Table 5.3).

It is generally considered that loosening occurs most commonly between the cement and the bone (Brown et al., 1988; Hampton et al., 1980; Harrigan et al., 1992; Rubbin et al., 1993). This is critical because the cement has lower fatigue limit, in the range of 60 MPa. The higher tensile stress occurs on the lateral interface adjacent to the proximal side of the prosthesis and the distal stem. The stress result of the simplified cylinder model also shows the same pattern. The simplified cylinder model and the titanium alloy prosthesis have lower normal tensile stress than the cemented model with Co-Cr alloy prosthesis along the interface of cancellous bone and cement in the lateral side. For the compressive stress of the medial side, the stresses range from 4.2 MPa to 0.2 MPa. The magnitude of the shear stresses is approximately 80% of the normal longitudinal stresses. However, the distribution of the shear stress is important in indicating the manner in which the stem is supported by the cement. The titanium prosthesis has about half the elastic modulus of the Co-Cr alloy prosthesis. Due to this there is a decrease in the interface stress of bone and

cement distally and increase in the proximal-medial region. The magnitude of the lateral tensile stress is significantly higher than the medial compressive stress. Therefore, the lateral interface between bone and cement should play an important role for prosthesis failure.

The stress at the femoral surface on the medial side increases distally, and the maximum stress occurs at the region near the distal tip of the prosthetic stem. The stress distribution of the lateral distal side keeps in a smooth range along the femoral surface, but the proximal side has significantly higher stresses. From the graphs of stress, it is seen that the longitudinal stress along the femoral surface of medial side is compressive and on the lateral side it is tensile. The corresponding von Mises stress along the femoral surface of medial side increases distally from 1.38 to 15.48 MPa. The maximum von Mises stress occurs at the proximal lateral side and the maximum value is 13.60 MPa. Comparing the Co-Cr alloy stem with the titanium alloy stem, the Co-Cr alloy stem will unload the calcar cortical bone (i.e. proximal-medial femoral neck). Therefore, the proximal load transfer with a cemented titanium alloy stem will endanger the most proximal PMMA, which will lead to failure.

The porous coating layer of the prosthetic stem provides better load transference, but it also unloads the calcar cortical bone. The effect of stiffness and compressibility of the porous coating layer will be examined from the stress patterns. It can be shown that a porous coating layer with lower mechanical modulus will slightly reduce the stem stress and slightly increase femoral bone stress. The lower Poisson's ratio will slightly increase the stem stress and slightly reduce femoral bone stress. Appendix A7 and Appendix A8 show that lower modulus and Poisson's ratio will also reduce the interface stress between cancellous bone and porous coating layer.

Peak stress affects the expected lifespan of the prosthesis. The maximum value of the stress of interest is listed as follows and is tabulated in Table 5.1:

Table 5.1 The maximum stress quantities along the interfaces and femoral surface.

	Co-Cr alloy Cemented	Porous coating	Simplified	Titanium
The maximum tensile stress along the lateral prosthesis boundary	30.81 MPa Proximal side	29.84 MPa Proximal side	41.98 MPa Proximal side	22.75 MPa Proximal side
The maximum tensile stress between the cement and the bone at the lateral interface	18.60 MPa Distal side	None	24.88 MPa Proximal side	13.42 MPa Proximal side
The maximum shear stress between the cement and the bone at the medial interface	2.136 MPa Proximal side	None	2.531 MPa Proximal side	2.50 MPa Proximal side
The maximum shear stress between the cement and the bone at the lateral interface	18.70 MPa Proximal side	None	16.55 MPa Proximal side	18.00 MPa Proximal side
The maximum von Mises stress along the medial femoral surface	15.39 MPa Distal side	14.31 MPa Distal side	8.642 MPa Distal side	17.28 MPa Distal side
The maximum von Mises stress along the lateral femoral surface	30.59 MPa Proximal side	28.85 MPa Proximal side	31.12 MPa Proximal side	30.71 MPa Proximal side

From the table, it is shown that the maximum stress of the cemented prosthesis is higher than that of porous coated prosthesis. The maximum stresses of the simplified cylinder model appear to be significantly lower. The use of a titanium with its lower elastic modulus results in substantial reduction of some critical stress except proximal-medial cement stress. The average tensile stresses in the prosthesis is reduced by 20%, the tensile stresses at the interface of cement and bone by 29%.

Table 5.2 Failure criteria for metal alloys used in total joint replacement.

Material	Yield	Fatigue
Co-Cr alloy	470 MPa	270 MPa
Titanium alloy	780 MPa	550 MPa

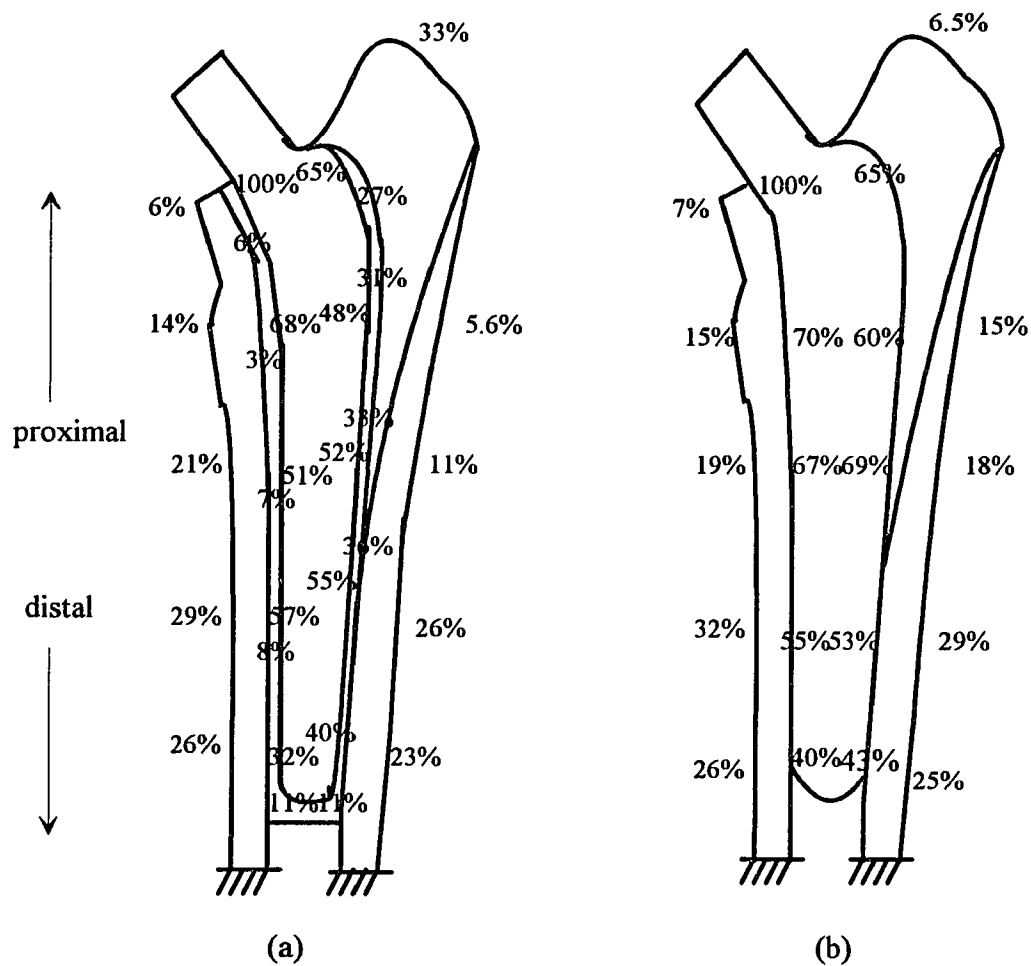


Figure 5.4 The percentage of load transfer in (a) cemented (b) porous-coated structure. The stress values of proximal prosthetic stem serve as the reference values, which are (a) 54.6 MPa (b) 44.7 MPa.

Table 5.3 Failure criteria for bone and acrylic cement.

Material	Tension	Compression
Acrylic cement	30 MPa	90 MPa
Cortical bone	90 MPa	140 MPa
Cancellous bone	15 MPa	30 MPa

Failure stress for stem alloy, cement, and bone are listed in the Table 5.2 and Table 5.3 (Cowin, 1989; Fung, 1981; Martens et al., 1983; Martine, 1991; Reilly et al., 1975; Schaffler and Burr, 1988; Schmid-Schonbein et al., 1985). Thus for the highest predicted stem stresses (Co-Cr alloy) the metal is only about 12% of its fatigue limit. Titanium alloy stem stresses are about 4% of the fatigue limit. However, cement stress is up to about 21% of the failure limit. Therefore, the interface of bone and cement will be a key region for the femur with prosthesis. Figure 5.4 depicts the percentage of load transfer in cemented and porous-coated structure. The stress values of proximal prosthetic stem which serve as the reference values, are 54.6 MPa and 44.7 MPa respectively. The load of the femur with prosthesis is transferred from the prosthetic stem to the bone. The stress values of the prosthetic stem increase proximally and that of the femoral bone increase distally. A porous-coated structure has better load transfer and more uniformly distributed stresses to the surrounding bony tissue in comparison to the cemented structure.

5.2 Comparison of Stress Pattern with Previous Works

Stress pattern validity is facilitated by comparing the results with those of other finite element results available in the literature. Figure 5.5 through Figure 5.8 depict the longitudinal variation of prosthesis and femoral surface stress for the cemented prosthesis, compared to similar data from Rohlmann et al. (1983), of Hampton et al. (1980) and Svensson et al. (1977). Rohlmann et al. (1983) used the anteroposterior and lateral radiographs of a cadaveric femur to create the finite element model. The elastic modulus of the prosthesis was taken to be 200,000 MPa; the cement elastic modulus used was

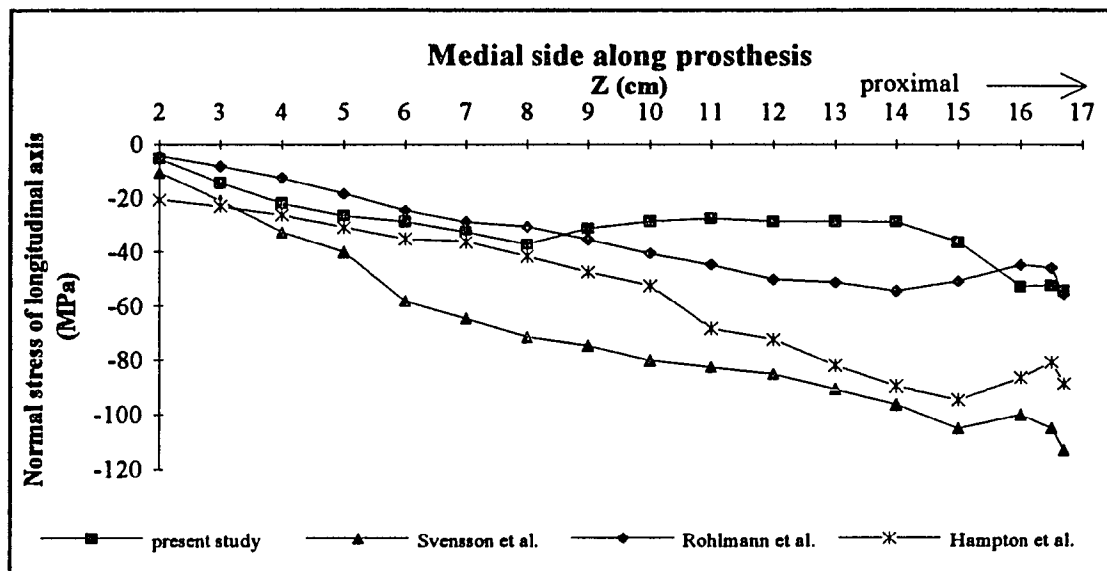


Figure 5.5 Comparison of the longitudinal stress distribution of medial side along prosthetic stem with previous stress analyses for the cemented femur-prosthesis.

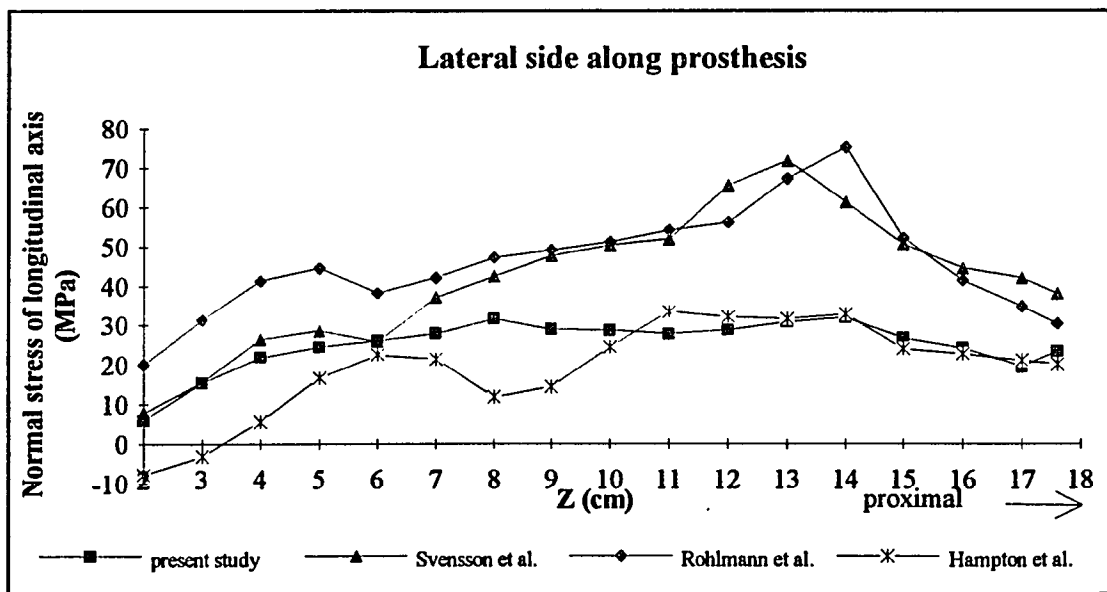


Figure 5.6 Comparison of the longitudinal stress distribution of lateral side along prosthetic stem with previous stress analyses for the cemented femur-prosthesis.

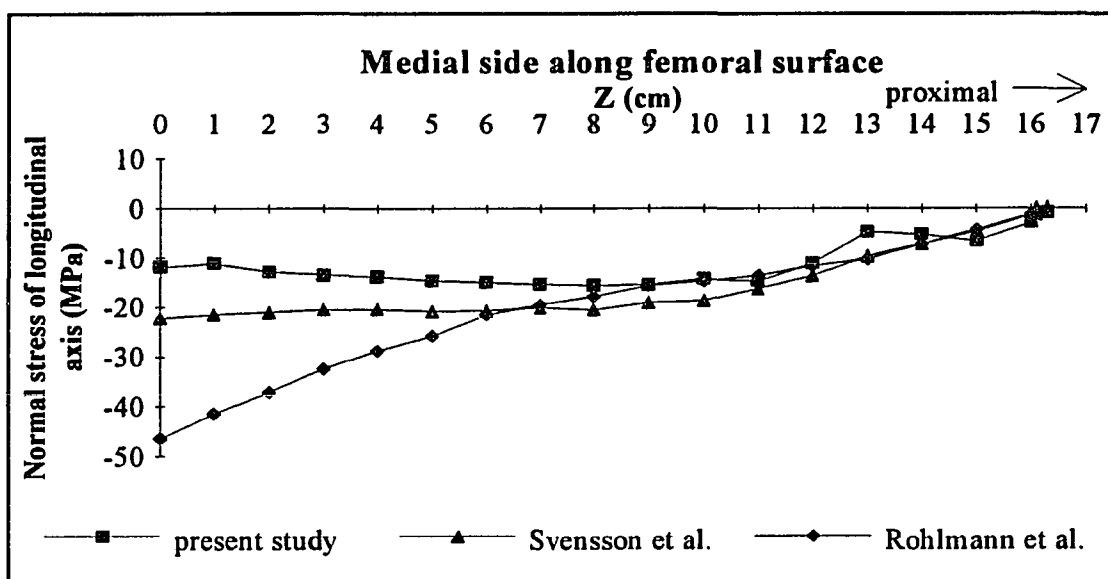


Figure 5.7 Comparison of the longitudinal stress distribution of medial side along femoral surface with previous stress analyses for the cemented femur-prosthesis.

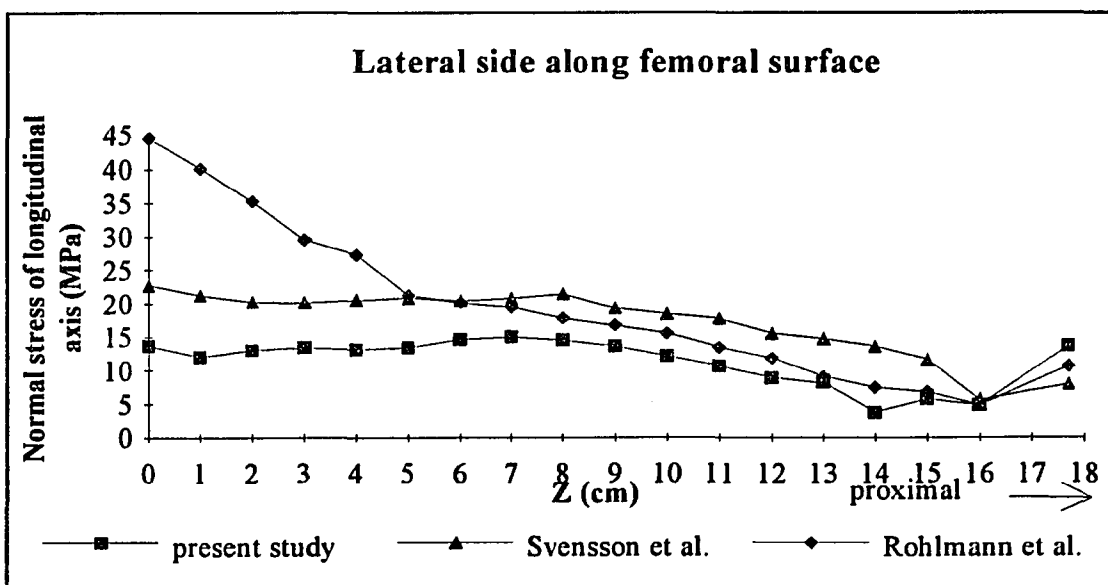


Figure 5.8 Comparison of the longitudinal stress distribution of lateral side along femoral surface with previous stress analyses for the cemented femur-prosthesis.

2,300 MPa, the cancellous bone elastic modulus was 1,800 MPa, and the cortical bone elastic modulus was 18,000 MPa. Poisson's ratios for prosthesis, cement, cortical and cancellous bone were taken as 0.33. In this finite element model, a higher loading condition was used. The forces on the prosthesis head and greater trochanter were applied 20° medial of the central axis and 15° anterior of the mid-frontal plane.

Table 5.4 Comparison of the finite element model with previous studies.

	Bone geometry	Joint force and direction (Ratio load)	Muscle force and direction (Ratio load)	Patient's age
Present study	3-D CT model	1874 N (20°) (1)	1027 N (15°) (1)	30
Rohlmann et al.	3-D Radiographs	2670 N (16°) (1.424)	1973 N (20°) (1.921)	
Hampton et al.	3-D Simplified model	2000 N (25°) (1.067)	0	
Svensson et al.	2-D Radiographs	1620 N (24.3°) (0.864)	1062 N (29.5°) (1.034)	78

Hampton et al. (1980) created geometrically 3D simplified model and used only the hip joint force as the loading condition. The force on the prosthesis head was applied 25° medial of the central axis. The elastic modulus of the prosthesis was taken to be 196,000 MPa; the cement elastic modulus used was 2,300 MPa, the cancellous bone elastic modulus was 2,800 MPa, and the cortical bone elastic modulus was 17,600 MPa. Poisson's ratios for cortical and cancellous bone were taken as 0.3, 0.29 for prosthesis, and 0.33 for cement. Svensson et al. (1977) created a two dimensional model which used side plate elements (2D shell elements) and loading conditions similar to the present work. The force in this paper on the prosthesis head and greater trochanter were 24.3° medial of the central axis and 29.5° anterior of the mid-frontal plane. The elastic modulus of the

prosthesis was taken to be 196,100 MPa; the cement elastic modulus used was 900 MPa, the cancellous bone elastic modulus was 325 MPa, and the cortical bone elastic modulus was 17,260 MPa. Poisson's ratios for cortical and cancellous bone were taken as 0.29, 0.30 for prosthesis, and 0.19 for cement. Table 5.4 shows the information concerning these finite element models.

Load can be nondimensionalized by dividing each by the maximum load. In this way they can be compared. Since Rohlmann et al. (1983) used higher forces higher stress patterns were generated in the finite element model. The magnitude of the applied loads is about 1.7 times that of the present work. It is found that the generated stresses at the prosthesis and bone surfaces of the proximal lateral side are about 1.6 times that of the present work and about 2.5 times at the distal lateral side. The stresses at the prosthesis surface of the proximal medial side are about 1.8 times that of the present work and 0.9 times at the distal medial side. The stresses at the bone surface of the proximal medial side are almost equal to that of the present work and 3.5 times at the distal medial side. Therefore, the expected stresses occur at the proximal lateral side. The other regions have higher or lower stresses than the expected stresses. Hampton et al. (1980) used the simple geometry model and simulated the hip joint force only. It is found that the stresses at the prosthesis surface of the proximal medial side are 3 times that of the present and 1.3 times at the distal medial side. The stresses at the prosthesis surface of the proximal medial side are almost equal to that of the present work and half at the distal medial side. The relatively higher stresses were generated in this finite element model. Svensson et al. (1977) used loading conditions similar to the present work, but the higher stress patterns were created. The magnitude of the applied loads is about 0.95 times that of the present work. The stresses at the prosthesis and bone surfaces are about 1.6 times that of the present work.

If the average value of the joint force and muscle force is used as the average applied load, the stress divided by the average applied load can be normalized to a unit load to the

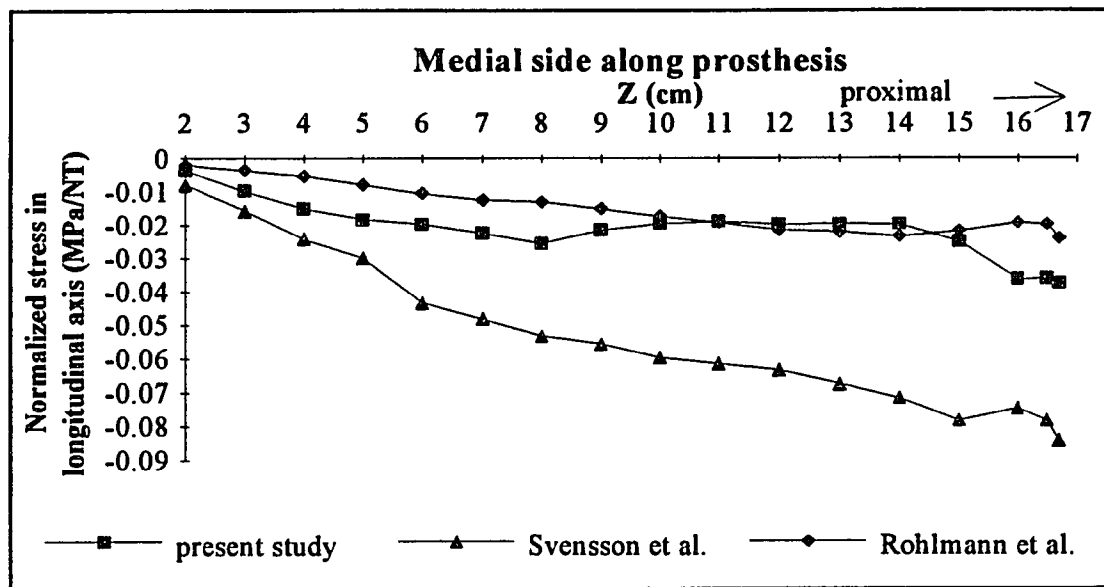


Figure 5.9 Comparison of the normalized longitudinal stress distributions on the medial prosthetic stem with previous stress analyses.

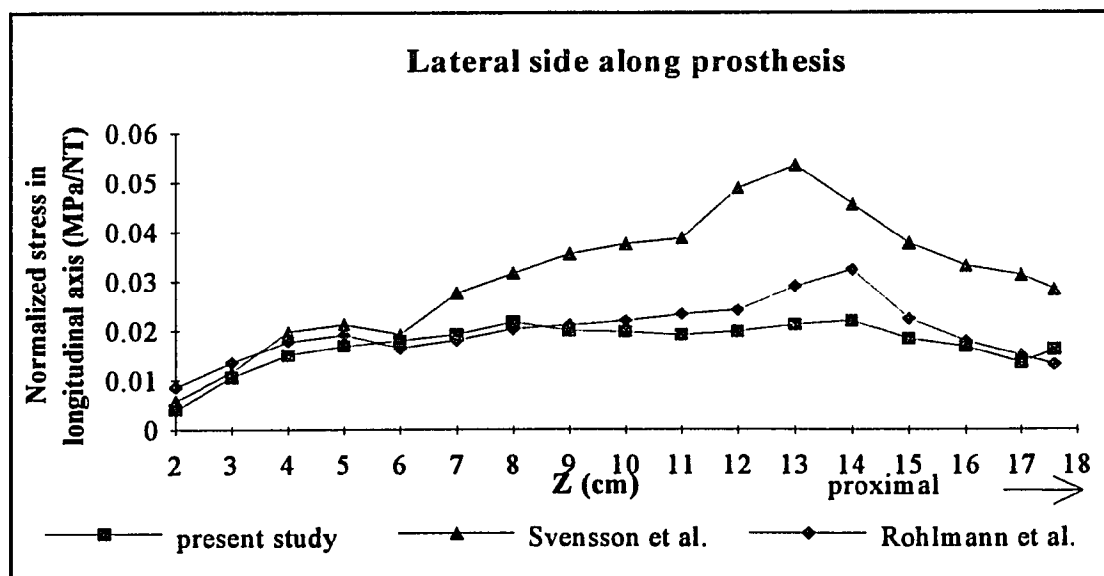


Figure 5.10 Comparison of the normalized longitudinal stress distributions on the lateral prosthetic stem with previous stress analyses.

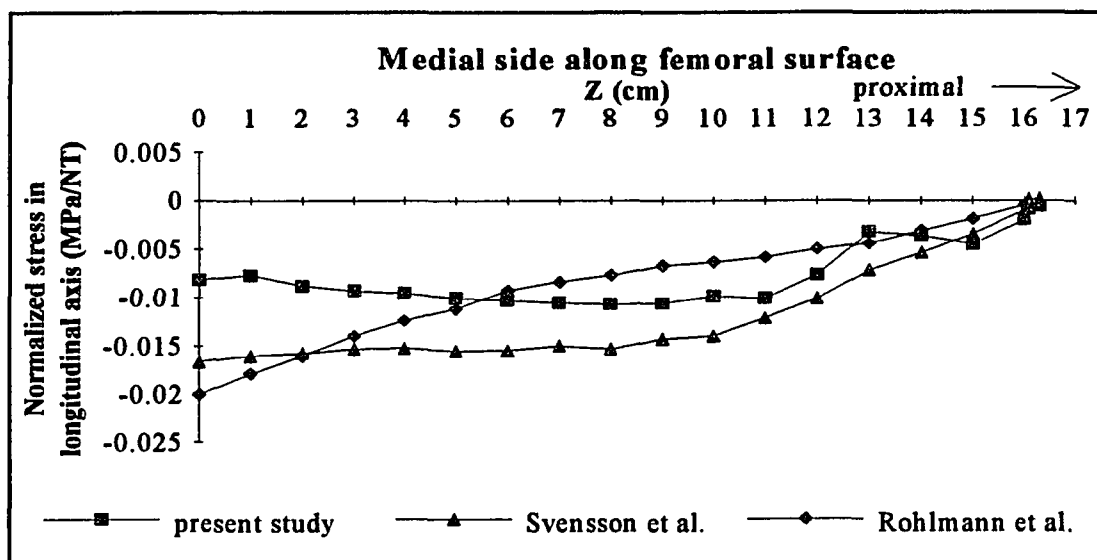


Figure 5.11 Comparison of the normalized longitudinal stress distributions on the medial femoral surface with previous stress analyses.

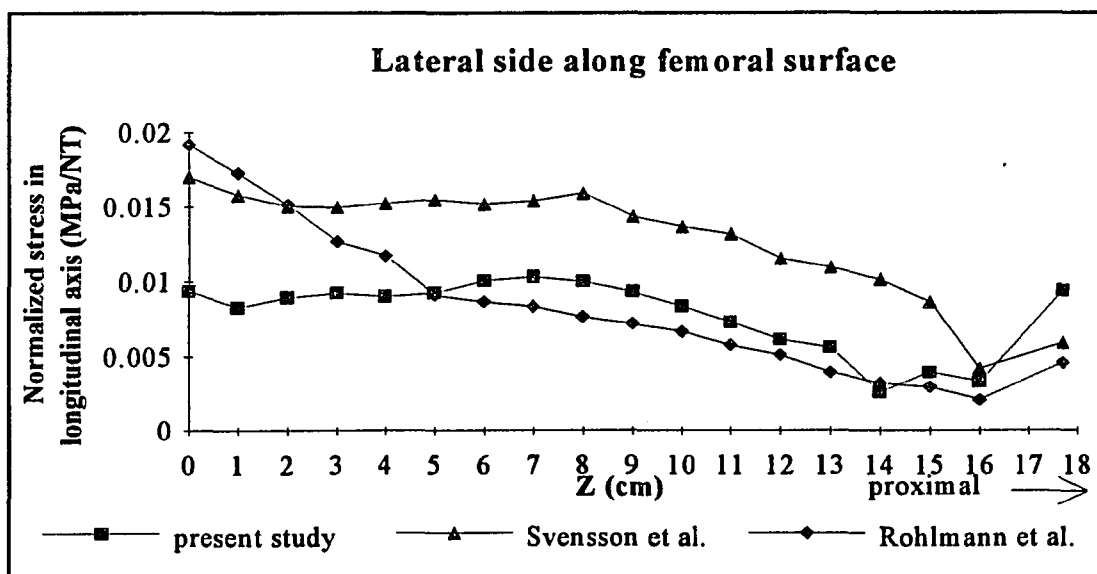


Figure 5.12 Comparison of the normalized longitudinal stress distributions on the lateral femoral surface with previous stress analyses.

femoral head and greater trochanter. Figure 5.9 through Figure 5.12 show the normalized stress distributions in the longitudinal axis for three different finite element works. The normalized stress distributions of Rohlmann et al. (1983) at the prosthesis surface are very close to the present work. The normalized stress at the proximal femoral surface is slightly less than the present work, but the normalized stress at the distal femoral surface is found to be 1.6 times larger than the present work. The normalized stress of Svensson et al. (1977) at the proximal-medial prosthesis surface is about three times that of the present work, and double at the distal side. The normalized stress at the proximal-lateral prosthesis surface are double that of the present work, and is slightly larger than the present work at the distal side. The normalized stress at the femoral surface is found to be about 1.5 times larger than the present work.

Precise agreement of specific stress component magnitudes is not to be expected, since the geometry, material property assumptions and specific loading conditions differ somewhat among these studies. From the stress patterns, it can be shown that the predominant effect of the applied loads is bending, generating compressive stresses on the medial surfaces, and tensile stresses on the lateral surfaces in the longitudinal direction. Due to the geometry of the prosthesis and the direction of the applied forces, most of the load is transferred to the distal portion of the bone, reducing the stresses in the proximal bone. This reduction in bone stress is referred to as stress shielding and may lead to subsequent resorption of the bone. Compared to these studies, the present stress patterns have good agreement. Therefore, it is clear that the present stress results correlate reasonably well with these previous finite element results.

5.3 Evaluation of Three Cases

Case 3 (fractured femur) had deformation in bone geometry and also had obvious changes in bone density. From the calculated stress patterns a fractured femur with a prosthesis has complex stress distributions in comparison to the normal shape femur with prosthesis.

Appendix A9 through Appendix A12 are the corresponding stress distributions for normal shape femora (Case 1 and Case 2) and fractured femur. The average stress of the fractured femur is about double that of the normal shape femur in the medial side along prosthetic stem and femoral surface. The fractured femur with prosthesis increases the average stress about 40% and double in the proximal and distal side of the prosthetic stem. But the midregion of the fractured femur has about 30% reduction on the midregion of the prosthetic stem. The average stress of the lateral femoral surface has about 20% and 30% reduction in the proximal and midregion respectively. The average stress of the lateral-proximal femoral surface is about 2.5 times as large as that of the normal femur. From the stress patterns, it can be understood that the fractured femur with prosthesis would have much more risk than the normal shape femur with prosthesis because of the bone deformity and bone density.

In this study, a male femur (Case 1) and a female femur (Case 2) with the same size prosthesis are provided to compare the stress patterns. Comparing the male and female femora, the stress distributions are not significantly different. The average stress of the male femur with prosthesis is about 4% lower than the female femur with prosthesis. Because of the differences of bone geometry and bone density, there are different stress patterns in each individual. However, the normal shape femora with prostheses would have similar stress distributions.

5.4 Bone Remodeling

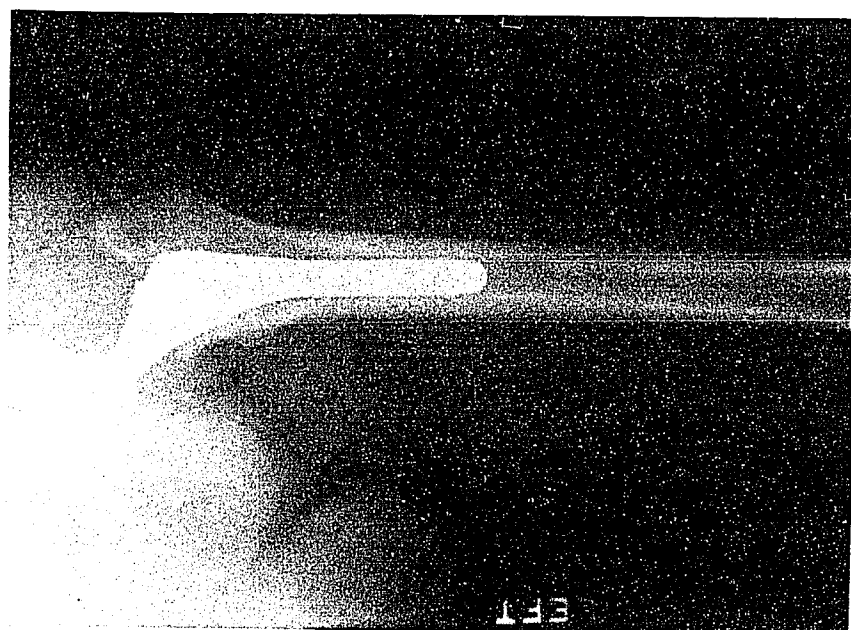
One effect of total joint replacement is that it changes the normal stress pattern in the bone. Remodeling can then occur. The local bone mass is adapted to the new functional requirements. Such a process could endanger the long-term success of the replacement since, a prosthetic component will not remain well-fixed when its bone bed disappears. On the other hand, remodeling may also have a beneficial effect, when it strengthens the bone/prosthesis composite as a whole.

The typical pattern of femoral remodeling in a hip with stable prostheses is resorption of the cortex around the proximal end of the component and hypertrophy around the distal end of the component. Resorption in the proximal-medial cortex including loss of cortical density, rounding of the medial aspect of the femoral neck, and longitudinal cortical loss (Brown et al., 1985; Engh et al., 1988; Huiskes et al., 1992; Martell et al., 1993; Pilkington et al., 1993 Rietbergen et al., 1993).

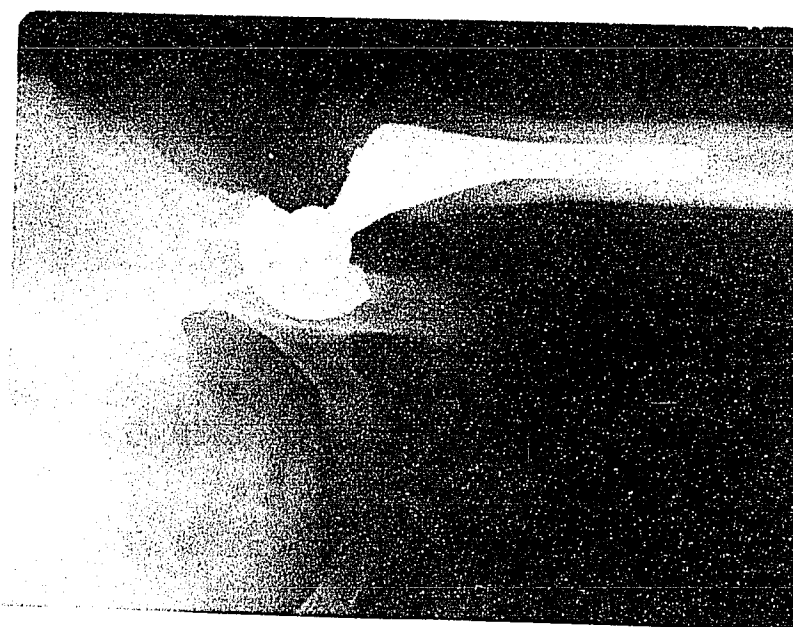
A radiographic follow-up study was carried out for Case 1 (male femur) at 14 months postoperation and for Case 2 (female femur) at 12 months postoperation. These two patients had total hip arthroplasties in which a porous coated cobalt-chromium alloy prosthesis was inserted. Anteroposterior and lateral radiographs of the femur are evaluated for cortical remodeling, and changes at the bone-prosthesis interface. Figure 5.13 through Figure 5.14 show the immediate and 14 months postoperative radiographs of the Case 1 (male femur). Figure 5.15 depicts the immediate and 12 months postoperative radiographs of the Case 2 (female femur). From the postoperative films, it can be observed that these two femora have typical bone remodeling which is resorption of the cortex around the proximal end of the prosthesis and hypertrophy around the distal end of the prosthesis and lesser trochanter. The geometric changes in bone diameter are shown in Figure 5.16.

Quantitative analysis is made from the anteroposterior radiograph of the femur. The diameter of the prosthetic stem is used as the standard for correction for bone magnification. In this study the average duration of follow-up is 13 months. Because the duration of follow-up is not long enough compared to the general follow-up (Maistrelli et al., 1991; Matell et al., 1993), there are only slight changes in bone geometry.

A mathematical description of the bone-remodeling process is used to analyze the development of the morphological changes in a quantitative manner. Several quantitative bone-remodeling theories can be found in the literature (Cowin, 1984; Huiskes et al., 1987; Rietbergen et al., 1993; Weinans et al., 1993). The adaptive process is usually described as occurring relative to the internal morphology, density (internal remodeling) or

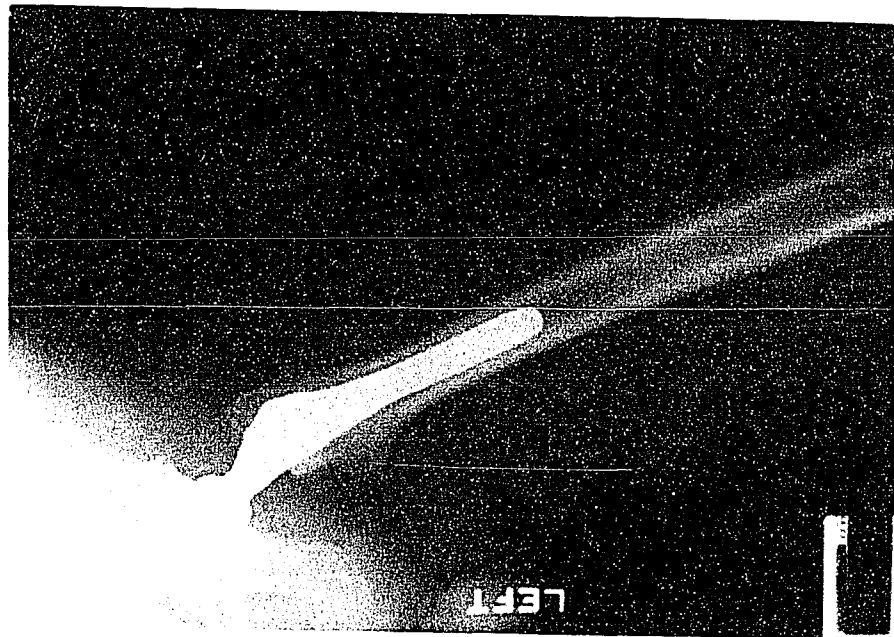


(a)

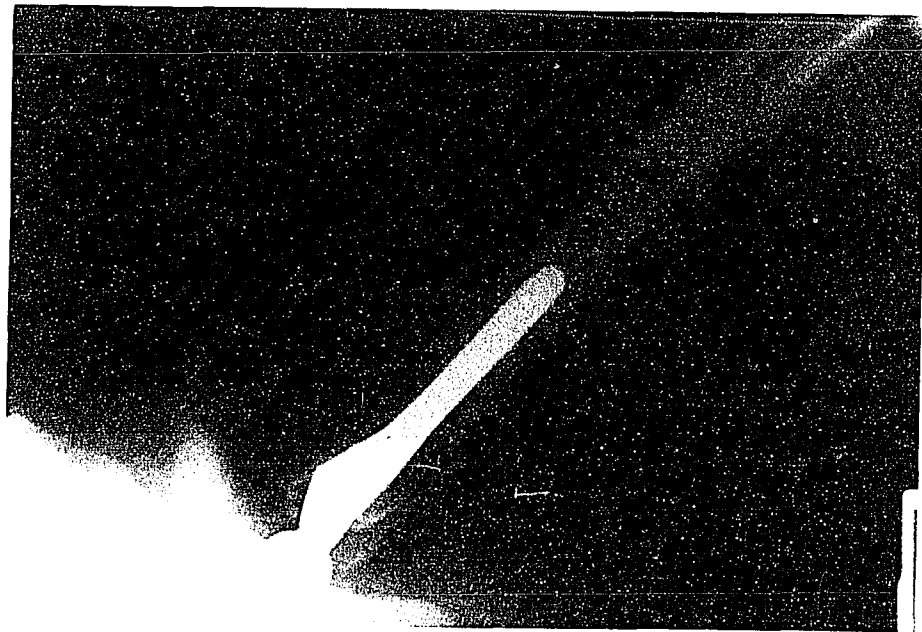


(b)

Figure 5.13 Anteroposterior radiographs showing the pattern of femoral remodeling in Case 1. (a) Immediate postoperative radiograph. (b) 14 months postoperative radiograph.



(a)



(b)

Figure 5.14 Lateral radiographs showing the pattern of femoral remodeling in Case 1. (a) Immediate postoperative radiograph. (b) 14 months postoperative radiograph.



(a)



(b)

Figure 5.15 Anteroposterior radiographs showing the pattern of femoral remodeling in Case 2. (a) Immediate postoperative radiograph. (b) 12 months postoperation for left femur and 1 month postoperation for right femur.

the bone diameter (external remodeling or surface modeling). Internal remodeling can be expressed as a change of porosity, which is one of the most important parameters characterizing the internal morphology. External remodeling can be expressed as a displacement of the subperiosteal surface, which redefines the external geometry.

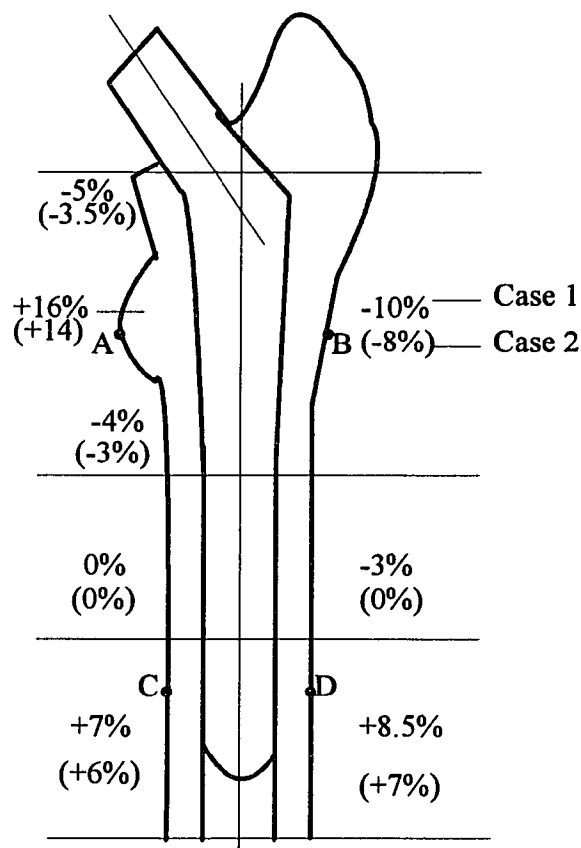


Figure 5.16 Illustration showing the geometric changes in bone diameter for Case 1 and Case 2 measured on the anteroposterior radiograph of the femur.

The hypothetical adaptive remodeling process can be explained as follows (Weinans et al., 1993). A bone is loaded by external forces that cause internal loads and deformation, represented by stresses and strains, in the bone material. These stresses or strains can be considered to be local mechanical stimuli that can be sensed by the bone. If the stimulus is abnormal, due to altered loading patterns or placement of a prosthesis, the mechanical signal is transduced to a biochemical one and subsequently integrated with

several other factors to cause a remodeling potential. The potential will affect the turnover rate of the bone by activating osteoblasts or osteoclasts. This will result in adaptation of the geometry (external remodeling) and the density (internal remodeling). As a result, the stresses and strains in the bone also will change, affecting the remodeling potential again. This process will continue until the mechanical stimulus is normalized.

The bone-remodeling theory is based on a site-specific (conservative) formulation (Huiskes et al., 1987; Rietbergen et al., 1993; Weinans et al., 1993). The actual local remodeling stimulus S (J/g), the strain energy per unit of bone mass can be determined from the strain-energy density $U = (\epsilon \times \sigma)/2$ (with ϵ the strain tensor and σ the stress tensor) and apparent density ρ , according to

$$S = \frac{U}{\rho} \quad (5.1)$$

The local bone in the operated femur strives for equalization of its remodeling signal S to the corresponding local value S_{ref} in the nonoperated one for the same external loads, by removing or adding bone. The theory assumes a threshold level for the remodeling response. Hence, when $|S - S_{\text{ref}}|$ is smaller than the threshold value, no remodeling response occurs. The adaptive remodeling process can then be described by

$$(1 - T)S_{\text{ref}} \leq S \leq (1 + T)S_{\text{ref}} \quad (5.2)$$

with T a constant. The region between $(1 - T)S_{\text{ref}}$ and $(1 + T)S_{\text{ref}}$ represents the nonresponsive area or dead zone. In accordance with the previous study (Weinans et al., 1993), T is set to 0.35, or 35%.

A periosteal nodal point displacement (Δx) and the change of apparent density ($\Delta \rho$) in a time step Δt (months) can be expressed as:

$$\Delta x = \frac{\beta}{\rho} [S - (1 \pm T)S_{\text{ref}}] \Delta t \quad (5.3)$$

$$\Delta \rho = \beta \alpha(\rho) [S - (1 \pm T)S_{\text{ref}}] \Delta t \quad (5.4)$$

$$\text{if } S \leq (1 - T)S_{\text{ref}} \text{ or } S \geq (1 + T)S_{\text{ref}}$$

where the time constant β is empirically determined in the previous study (Weinans et al., 1993) by comparing the two-year animal and simulation results for bonded prostheses. It is found that the value of β should be set to $\beta = 130 \text{ g}^2/\text{mm}^2\text{J}$ per month to have the time t given in units of one month. $a(\rho)$ represents the internal free surface area per unit volume of whole bone.

Since the stresses and strains of the operated and nonoperated femora can be calculated from the present finite element model, the bone-remodeling theory can be applied to predict the external remodeling. The simulation results of the geometric adaptations at the periosteal surface can be compared with the measurement from the postoperative radiographs. For the internal remodeling, postoperative CT scans are needed to measure the bone densities and are not available in this study. Therefore, only external remodeling is studied.

Four nodal points of Case 1 shown in Figure 5.16 at point A, B, C, and D with obvious geometric changes are selected to calculate the external remodeling. The strain-energy density of the operated (U) and nonoperated (U_{ref}) femora at these points are as follows:

$$U = \frac{1}{2}(\sigma_x \varepsilon_x + \sigma_y \varepsilon_y + \sigma_z \varepsilon_z + \tau_{xy} \gamma_{xy} + \tau_{yz} \gamma_{yz} + \tau_{xz} \gamma_{xz})$$

$U_A = 4.607 \times 10^{-3} \text{ MPa}$	$U_{\text{ref},A} = 1.242 \times 10^{-3} \text{ MPa}$
$U_B = 1.021 \times 10^{-3} \text{ MPa}$	$U_{\text{ref},B} = 3.821 \times 10^{-3} \text{ MPa}$
$U_C = 3.824 \times 10^{-3} \text{ MPa}$	$U_{\text{ref},C} = 2.446 \times 10^{-3} \text{ MPa}$
$U_D = 3.615 \times 10^{-3} \text{ MPa}$	$U_{\text{ref},D} = 1.955 \times 10^{-3} \text{ MPa}$

The nonoperated femur and the immediate postoperative femur are assumed to have the same apparent densities, the apparent density term (ρ) in Equation 5.3 can then be eliminated and the equation becomes

$$\Delta x = \beta[U - (1 \pm T)U_{\text{ref}}]\Delta t \quad (5.5)$$

β and T are set to 130 and 0.35 respectively according to the previous study (Weinans et al., 1993). The periosteal nodal point displacement (Δx) can be obtained by applying Equation 5.5.

$$\Delta x_A = 3.19 \text{ mm}$$

$$\Delta x_B = -2.66 \text{ mm}$$

$$\Delta x_C = 0.95 \text{ mm}$$

$$\Delta x_D = 1.59 \text{ mm}$$

The results for the bone-remodeling theory and for the real measurement are tabulated (Table 5.5). Since the applied bone-remodeling theory is based on canine study and different prosthesis test, precise agreement of specific periosteal nodal displacement magnitudes is not be expected. A comparison of the predicted periosteal nodal point displacement with data from in vivo measurement shows reasonable agreement.

Table 5.5 The comparison of the external modeling between the bone-remodeling theory and the measurement from radiographs.

	Δx Theoretical	Δx Measured	Error %
Δx_A (mm)	3.19	4.1	22.20%
Δx_B (mm)	-2.66	-3.3	19.39%
Δx_C (mm)	0.95	0.8	18.75%
Δx_D (mm)	1.59	1.25	27.20%

The second important issue in bone remodeling is postoperative stress changes. A postoperative finite element model is created by the preoperative CT scans and the films. The following is the method used to create a finite element models of the postoperative femur with a prosthesis. The cortical bone boundaries of the scanned cross sections of the preoperative femur are detected by the preprocessor. The nodes can be selected on the bone boundaries. Since the bone remodeling can be measured from the postoperative radiographs, the finite element models of the postoperative femora (Case 1 and Case 2) can be generated by moving the node positions of the preoperative CT scans according to the geometric changes. Because the shape of the bone cross section is close to round at

the distal side and there is similar cortical hypertrophy at the distal-medial and distal-lateral sides, the changes of the node positions on the outside boundary of the distal cross sections (cross section #13 through #17) are equivalent. The node positions of the proximal cross sections (cross section #1 through #5) are changed according to the measurement of postoperative radiographs.

Since the finite element models of the postoperative femora with prostheses can be generated by the preoperative CT scans and the measured geometric changes in the postoperative radiographs, the stress pattern can be obtained by stress calculation of this postoperative model. From the stress patterns (Appendix A13 through A16), it can be observed that the average stress is increased about 1% in the proximal prosthetic stem, decreased about 10% in the midregion of the prosthetic stem, and decreased about 35% in the distal prosthetic stem after bone remodeling. The average stress along femoral surface is increased 8% in the proximal side, decreased 3% in the midregion, and decreased 30% in the distal side. Therefore, bone resorption of the cortex around the proximal prosthesis would increase the stresses at the proximal prosthetic stem and the femoral surface. In the meantime, the stresses of the midregion are decreased along the prosthetic stem and the femoral surface. Bone hypertrophy around the distal prosthesis would decrease the stresses up to 35% at the distal prosthetic stem and femoral surface.

Most bone adaptations around prostheses, as seen in the orthopedic clinics, are effects of abnormal bone stress (Cheal et al., 1992; Engh et al., 1988; Huiskes et al., 1991; Martell et al., 1993; Rietbergen et al., 1993). It is generally assumed that the resorptive phenomena are a result of stress shielding and adaptive bone remodeling in accordance with Wolff's law. The prosthetic stem shields the bone from stress because it shares the load which is normally taken by the bone alone. As a result, the bone stress is reduced and with bone remodeling, mass is reduced accordingly. Because bone stress and stress-shielding patterns depend on the material, geometrical and bonding characteristics of the prosthesis, the bone resorption patterns must also depend on these characteristics. The

changes of the stress patterns in the femur with prosthesis are affected by the bone remodeling patterns. Because of the relationship between prosthesis characteristics and stress patterns, prosthetic designs can be optimized to produce as little bone loss as possible and expand prosthetic lifespan.

5.5 Discussion

The three dimensional stress analysis of the femoral stem implanted with cement or porous coating in bone is a complex problem. Although the finite element model provides a viable approach to the solution of this problem, use of this method requires careful consideration of all aspects of the model formulation. Accurate analysis of the structure of the reconstructed hip is difficult because of complexities of geometric form, material properties, and loading conditions. By using computed tomography (CT) technique, the geometry and material distribution of the bone and prosthesis can be described more accurately. The number of elements is limited by the storage capacity of the finite element program and the computer. However, finite element stress analysis, particularly when it is three-dimensional, is useful for predicting the changes in stress distribution that result from variations in design parameters.

Finite element stress analysis assumes that nodal points at the boundaries between different materials in the structure have displacements that are compatible with the material elements on both sides of the boundary. This implies that the material boundaries in the analysis are ideally bonded surfaces that transmit tension, compression, and shear. Although such ideal bonding is not likely to occur in vivo, the assumption should be practical.

The loads are assumed to be applied on the prosthetic stem and greater trochanter. The three-dimensional and variable nature of the in vivo stem loads and of the various muscle loads would produce significantly variable patterns of stress distribution. The

loading situation chosen in this study is perhaps one of the most demanding situations during prosthetic function.

The materials comprising the prosthetic components as well as the femur are assumed to be linear elastic and isotropic. Although this is a realistic assumption for the materials in the prosthetic component and cement, it represents a considerable simplification of the properties of bone. However, the representation of the anisotropic nature of bone structure would greatly complicate the mathematical process and would have made the study impractical.

The analysis of the stress distribution resulting from the load of gait simulation leads to several interesting observations. The load applied to the greater trochanter and the prosthesis produces tensile stresses along the lateral part of the prosthetic stem, the cement interface and femoral surface. Tensile stress can initiate cracks. Examination of failed femoral stems indicates that when the geometry of the fracture surface can be reconstructed, the origin of the crack often appears to be located at the anteriolateral corner of the stem (Hampton, 1979; Harrigan et al., 1992; Huiskes, 1990). This observation agrees with the stress patterns of the present femur-prosthesis finite element model.

High tensile stresses of the medial side and high shear stresses of lateral side exist at cement-bone interface. This seems to represent the failure of bone-cement interface occurring at the interface regions of the high stress. Higher stress components along femoral surface occur at the most proximal corner on the lateral side and the point adjacent to the prosthetic stem tip on the medial side. Bone fracture most likely occurs at these high stress regions.

Though the accuracy of bone geometry influences the stress pattern, the stress distributions of the simplified cylinder model are useful in judging the maximum stress regions and providing preliminary analysis for different prosthetic design. Therefore, the simplified model is useful for finding the effects of variations in prosthetic design. The

stress values of the porous coating prosthesis are lower than that of the cemented and the porous coating prosthesis produces less stress along the interface of bone and porous coating layer. Due to the lower stress and the good interlock feature, the porous coating prosthesis is more popular.

Two major problem areas associated with the success or failure of porous coating systems are (1) achieving bone ingrowth rather than fibrous tissue ingrowth, and (2) avoiding adverse bone remodeling associated with the change in bone stress fields after ingrowth is achieved. It is clear that the mechanical and material design of the prostheses plays a major role in these two problem areas. Two important prerequisites to obtain bone ingrowth are intimate contact and adequate immobilization; and that the most important of these two requirements is probably immobilization. This requirement is to prevent excessive relative motion between the prosthesis and the bone while ingrowth occurs. From a mechanical perspective, to achieve initial ingrowth one could probably like to provide prosthesis stability over a range of loading conditions, and avoid shear and tensile loading at prosthesis/bone interfaces. The evaluation of these parameters requires a rigorous mechanical examination. Such examinations are an important feature for future studies.

With the trend toward the use of total hip arthroplasty in younger patients, the greater life expectancy of the aged population, and the difficulty of revisions, the limitation of prosthesis longevity is becoming an increasing problem. The knowledge gained from the computational studies of prostheses and bone remodeling may contribute to the use of new prosthesis materials and designs for the development of longer lasting prostheses. Such prostheses would make hip arthroplasty more feasible for younger patients and would greatly increase the quality of life for all hip prosthesis recipients. Much work is needed to advance the development of quantitative bone remodeling, experimental verification, and the numerical simulation. Although the important research is always time

consuming, the future presents some exciting challenges and opportunities in the study of prosthetic design and bone remodeling.

5.6 CT Data Applied in CAD/CAM System

The development of preprocessor provides some important procedures for the creation of a finite element model such as geometric definition, mesh generation, model display, node and element numbering as well as load and boundary condition definition. In order to provide a prosthetic design process in future studies, a practical method is developed to transfer the CT data to the CAD system creating a three dimensional plastic bone geometry. Then send this CAD geometry file to Stereolithography Apparatus (SLA) creating a three dimensional plastic model.

5.6.1 Creating 3D Bone Geometry in CAD System

The following is a summary of the methods used to create a three dimensional bone geometry in a CAD system (I-DEAS V6.0).

1. Computed Tomography (CT) provides data files from which to develop the CAD system model. These CT data files are reconstructed into the suitable image size, then the CT data files are run through a geometric edge detection algorithm mentioned previously.
2. A computer program is contained in the preprocessor providing a means of manipulating the digitized data into an acceptable format for the solid modeling program (I-DEAS).
3. The solid modeling program (I-DEAS GEOMOD) provides a user friendly means of constructing solid geometry. Its menu driven formats could easily be accessed to construct a model of the femoral bone and store the resulting model.
4. The program file produced by the preprocessor contains outside and inside boundary profiles of 17 femoral cross sectional slices. A skinning operation is

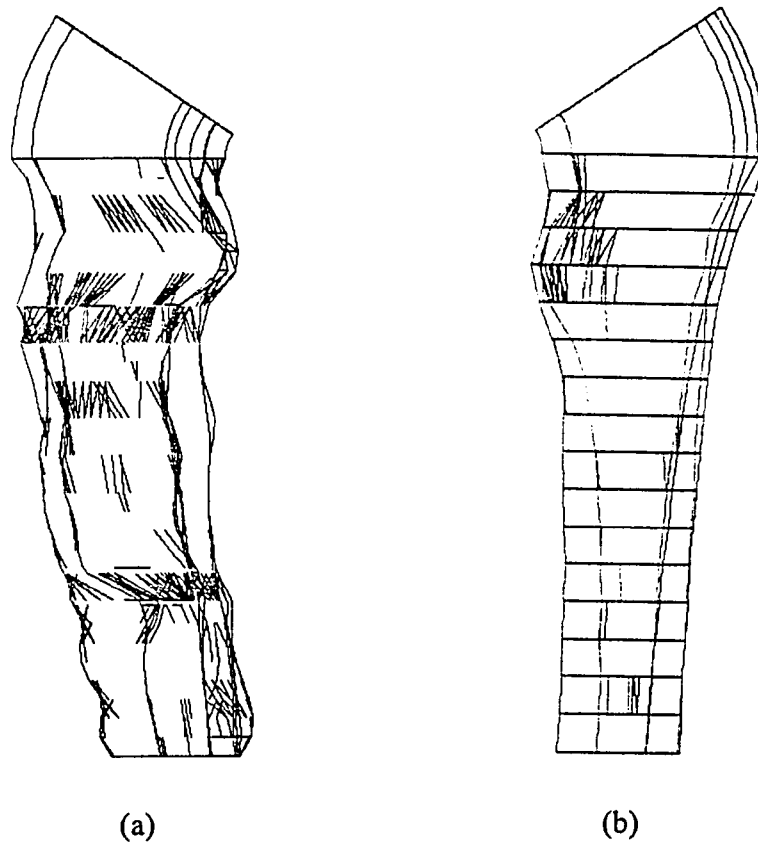


Figure 5.17 Three-dimensional femoral models for (a) a fractured femur, and (b) a normal shape femur are constructed in CAD system.

performed on the object whose outside and inside dimensions are computer interpolated to best approximate the three dimensional geometry.

Figure 5.17 displays the constructed femoral model in CAD system. The three dimensional femoral model provides a model for designing hip prostheses. This method establishes a quick and efficient way to create a bone model in the CAD system for the orthopedic research.

5.6.2 Creating a 3D Bone Model in SLA Machine

Stereolithography is a process which produces copies of solid or surface models in plastic. The process uses a moving laser beam, directed by a computer, to print or draw cross sections of the model onto the surface of photo-curable liquid plastic.

Using a Stereolithography Apparatus (SLA), solid or surface data is sliced by software into very thin cross sections. A Helium Cadmium (HeCd) laser then generates a small intense spot of ultraviolet (UV) light, which is moved across the top of a vat of liquid photopolymer by a computer controlled optical scanning system. The laser changes the liquid photopolymer into a solid where it is touched, precisely printing each cross section. A vertical elevator system lowers the newly formed layer, while a recoating and leveling system establishes the next layer's thickness. Successive cross sections, each of which adheres to the one below it, are built one on top of another to form the part from the bottom up. After the last layer is made, the part is removed from the SLA and flooded with high intensity ultraviolet light to complete the polymerization process. The part can then be finished by sanding, sand blasting or dyeing.

The stereolithography process is composed of ten major steps. The first three steps structure the object data for use on the SLA. The next six steps process the object and support data and control the part building process. The last step uses the Post Curing Apparatus.

1. The process begins with a design created on a surface or solid modeling CAD/CAM/CAE system. The data must represent a clearly defined enclosed volume.
2. The model is oriented in three dimensional space for optimum building. A support structure is then added to hold the part in place while the layers are being built to maintain layer registration and the structural integrity of the part. (Thin vertical webs usually comprise the supports.)
3. The design model and support data are converted to a stereolithography format through an interface supplied by the CAD/CAM/CAE system vendor. This format is similar to a finite element model consisting of triangular surface elements or patches. The users controls how accurately these triangles define the original surface. The output from this process is a stereolithography (.STL) file.
4. Using a sophisticated, proprietary algorithm, each file is sliced into cross sections, typically between 0.005 to 0.020 inches (0.12 to 0.50 mm). The user can select the layer thickness and vary it throughout the part. In addition, the user controls the creation of an internal crosshatch structure between the inner and outer surface boundaries (vertical walls). This serves to support the vertical walls and entrap liquid which will later be solidified with a flood of UV light.
5. After slicing, each database is transferred to the controlled computer using a local area network.
6. All the objects (support and part) are combined into one built part database. In this process, the data is reformatted into SLA machine code contained in four separate files: Vector file (.V), Range file (.R), Layer file (.L), Machine Parameter file (.PRM).
7. The laser power is measured and the SLA is initialized and set up to build parts. A platform is attached and lowered into the vat filled with liquid resin.

8. The user sets building parameters, including the amount of adhesion between layers, and the number and location of parts to be built as well as recoating parameters based on the model's geometry and end use. Each phase of the part building can be customized by varying building parameters within vertical ranges.
9. The resin level is adjusted by adding photopolymer. The user activates the "Build" software to control the part building process which creates one layer at a time by moving a focused layer beam across the surface of photo curable resin, and solidifying the liquid where it strikes. The laser draws the first cross section, which adheres to the platform. When creating each cross section, the inside and exterior boundaries are solidified along with the internal crosshatch. Resin is then trapped between the solid areas, as the object builds up. The elevator dips below the surface, coating the cross section with resin, and a recoater system maintains the correct amount of liquid on top of the previous cross section. The second layer is drawn and becomes firmly attached to the first. The process is repeated until all layers have been drawn to form the 3D object. When the part has been completed, the trapped liquid still requires UV exposure to become solid.
10. The part, after building has been completed, requires final ultraviolet curing. First the part is raised out of the vat and excess liquid is drained off the part. Next, the remaining excess liquid is removed with solvents, ultrasonics or wicking. The part is then placed, by the user, into the PCA (Post Curing Apparatus) to undergo several exposures. The part is later removed from the platform and the support structure is clipped from the part. Finishing techniques, such as sanding, sandblasting, painting, or dyeing, can then be applied.

The benefit of stereolithography is the fast turn around time for conceptual model — hours instead of the conventional weeks or months. Design review cycles can also be reduced by evaluating the 3D design instead of studying engineering drawings. Form, fit and function tests can be performed much earlier in the design cycle with a physical model.

With conceptual 3D model, designs can be finalized much faster. Producibility requirements can be brought into the design process before a commitment to one design is made, reducing manufacturing costs. Utilizing the plastic parts, production tooling design times can also be reduced.

CHAPTER 6

CONCLUSION

The three-dimensional finite element model of the femur with a prosthesis was developed and analyzed in this study. This is a useful method of modeling a biomechanical system and evaluating the effects of gait simulation. The stress pattern of the femur with a prosthesis also showed the following

1. study of stress due to fixation methods for hip implant,
2. study of stress resulting from orthopedic devices,
3. study of stress due to bone remodeling,
4. improving design of prostheses or fixation devices,
5. designing new orthopedic implants, and
6. evaluation of failed implants.

The detailed stress distributions are plotted in Appendix A. The following is a summary of the results found in this analysis:

1. The maximum interface stress occurs on the proximal side. The stress distribution within the prosthetic stem medially is compressive and increases proximally. The stress distribution within the prosthetic stem laterally is tensile and increases proximally. The magnitude of the lateral tensile stress is 70% of the medial compressive stress along the prosthetic stem.
2. The stress at femoral surface of the medial side is compressive and on the lateral side it is tensile. The stress at femoral surfaces of the medial and lateral side increases distally.
3. The simplified cylinder model has a lower stress value than the CT generated model. The average stress of the simplified cylinder model is about 40% lower than the generated CT model, and the stress distributions appear to be mostly regular.

4. Comparing the Co-Cr alloy prosthesis with the titanium alloy prosthesis, the Co-Cr alloy will unload the calcar cortical bone (i.e. proximal-medial femoral neck).
5. The titanium alloy prosthesis decreases the stress at the prosthetic stem except for the medial proximal side and increases the bone stress. The proximal load transfer with a cemented titanium alloy stem may endanger the most proximal bone cement, leading to failure.
6. The highest calculated stress is only about 12% of the fatigue limit for Co-Cr alloy prosthesis, and about 4% for titanium alloy. The cement/bone interface stress is up to 21% of the failure limit. Because the cement has lower fatigue limit, the interface of bone and cement will be a key region for hip-implant.
7. Comparing the porous coating model with the cemented model, the porous coating model will lead to decreased stresses and more uniformly distributed stress to the surrounding bone tissue.
8. For the effect of stiffness and Poisson's ratio of the porous coating layer, lower elastic modulus and Poisson's ratio will reduce the interface stresses between cancellous bone and porous coating layer.
9. Case 3 (a fractured femur) indicates a 50% increase in stress within the prosthesis compared to similar prosthesis in normal shape femora.
10. Case 1 (a male femur) and Case 2 (a female femur) with the same size prosthesis are provided to compare the stress patterns. Comparing the male and female femora, the stress distributions are not significantly different.
11. The bone-remodeling theory is applied to predict the external remodeling. A comparison of the predicted periosteal nodal point displacement with data from radiographic measurement shows reasonable agreement.
12. Radiographs for Case 1 and 2 at 14 and 12 months postoperation were observed and measured, it was found that these two cases had typical bone remodeling

which was resorption of the cortex around the proximal end of the prosthesis and hypertrophy around the distal end of the prosthesis.

13. Due to the geometric changes of the bone remodeling, the average stress is increased 1% in the proximal prosthetic stem, decreased 10% in the midregion of the prosthetic stem, and decreased 35% in the distal prosthetic stem at average 13 months postoperation. The average stress along the femoral surface is increased 8% in the proximal side, decreased 3% in the midregion, and decreased about 30% in the distal side.

In this analysis method a preprocessor was developed to process a CT data file of a scanned femur, to simulate a fitting prosthesis and to create a formatted input file for the stress calculation by the finite element program. A summary of the preprocessor developed in this study is as follows:

1. The preprocessor reads a scanned femur data file which contains the header information and radiographic density information of femoral cross section. The scanned image cross sections are reconstructed to create a three-dimensional finite element model.
2. A first order edge detection routine defines the outside and inside borders of the compact bone in the bone cross sections. The geometric centers of cross sections are obtained by the positions of the outside and inside borders.
3. The node selection defines a constant number of nodes in each cross section by using an edge detector in radial direction. An algorithm is designed to select nodes for the detected cortical bone.
4. The prosthesis is selected according to the femoral canal size. The nodes are also selected within the borders of the designed prosthesis and at the interface.
5. The element definition routine defines three dimensional isoparametric eight-node elements from each two adjacent cross sectional images. The method of

automatic generation of the elements is inherent with the node numbering method.

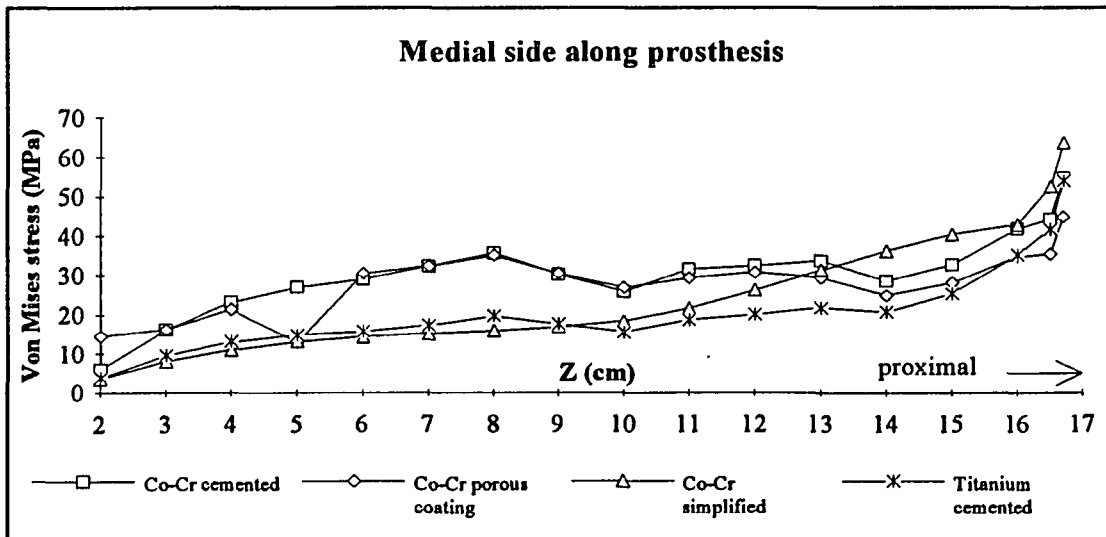
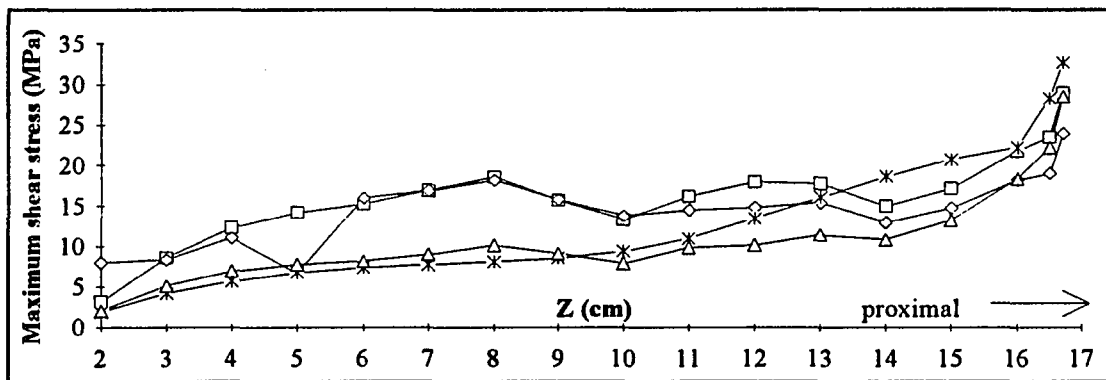
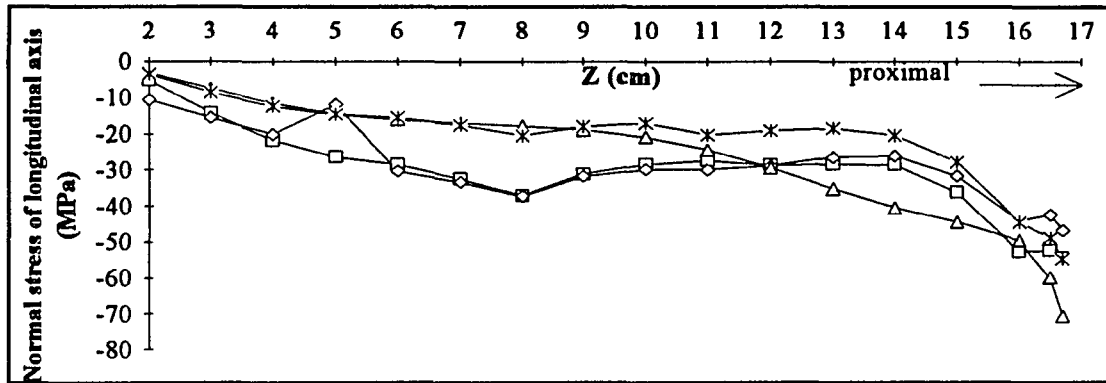
6. A routine assigns elastic modulus and Poisson's ratio for each element in the model. The loading conditions of gait simulation are applied on the three-dimensional finite element model.

The general path of data analysis from scan to prosthetic simulation and finite element mesh has been established with this study. CT scan data provides information on bone properties, including bone density and mineral content. The more accurate bone geometry produced by CT scan data supports the creation of a more accurate and reliable finite element model. The three-dimensional femur-prosthesis model also provides a good object for future studies, such as prosthetic slipping problem, bone fracture fixation, and the optimization of prosthetic design.

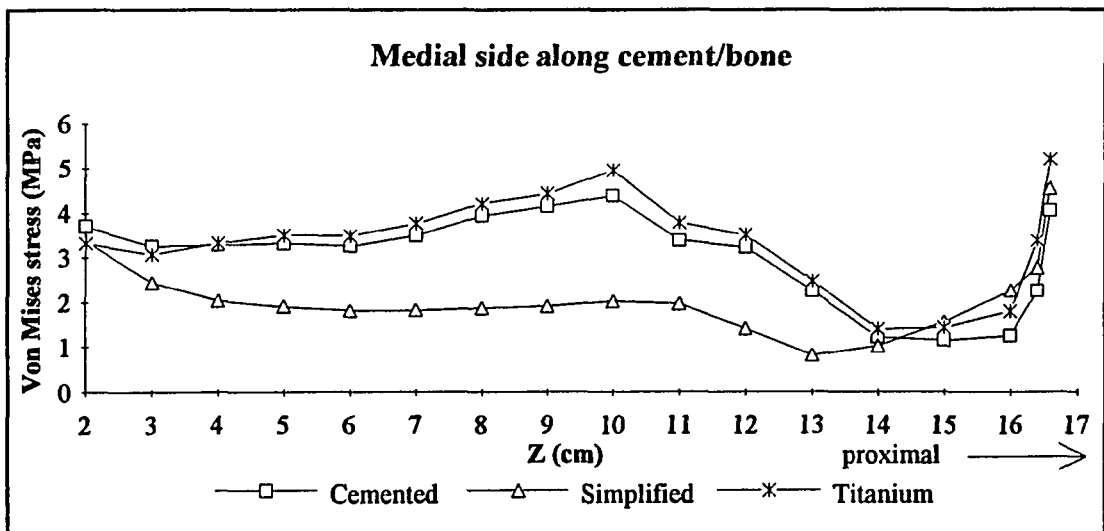
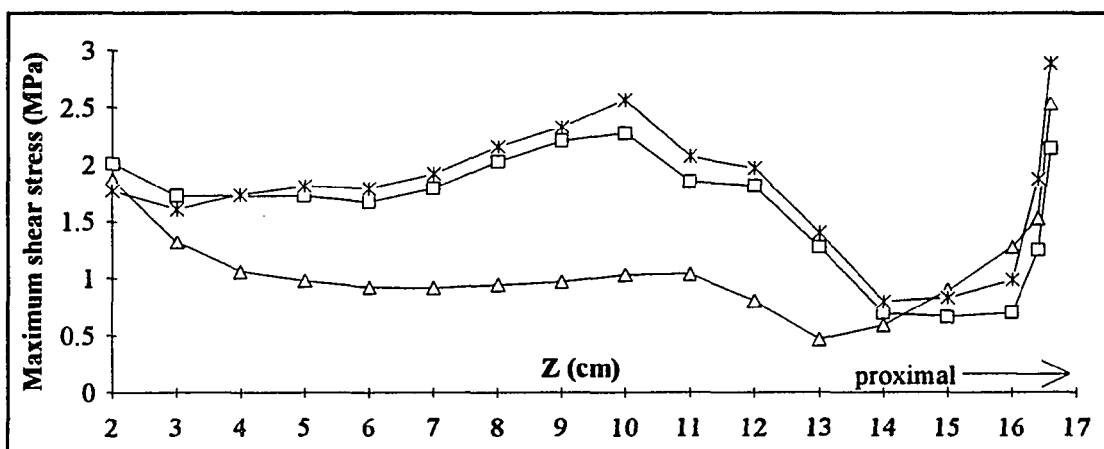
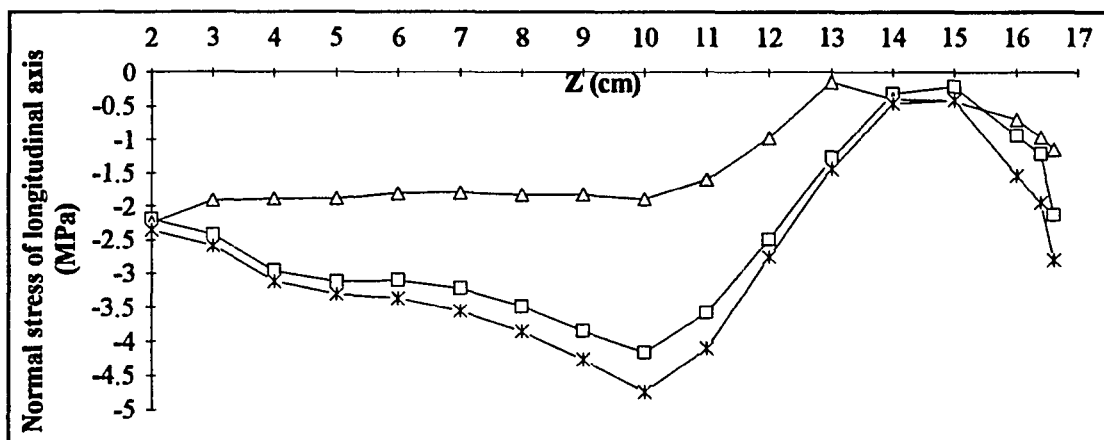
In summary, this study provides an engineering, noninvasive, versatile and relatively accurate tool for understanding the stress pattern of the femur with a prosthesis and improving the prosthetic design utilizing CT data.

APPENDIX A

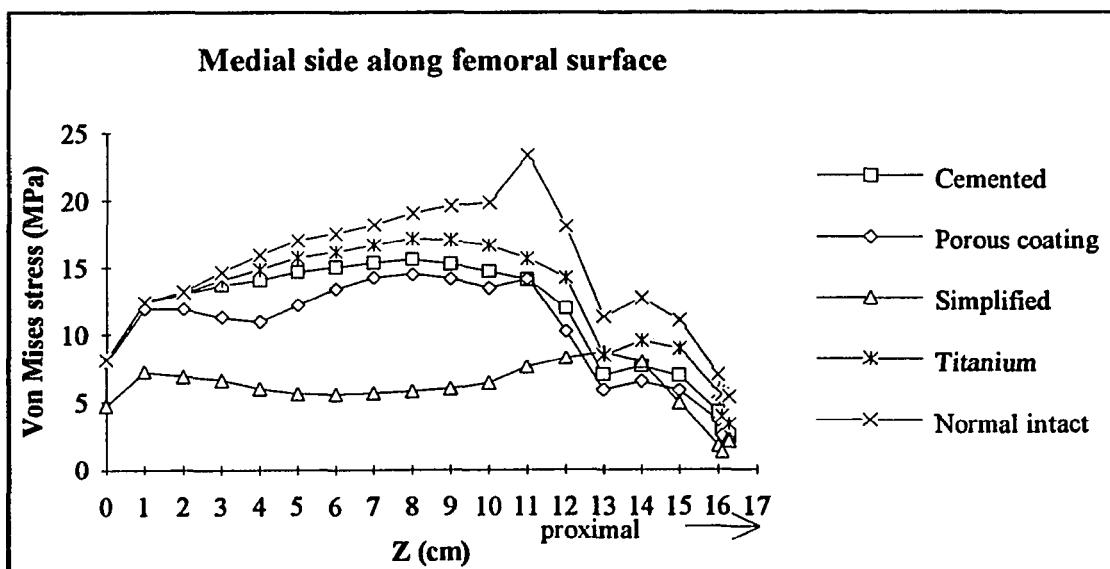
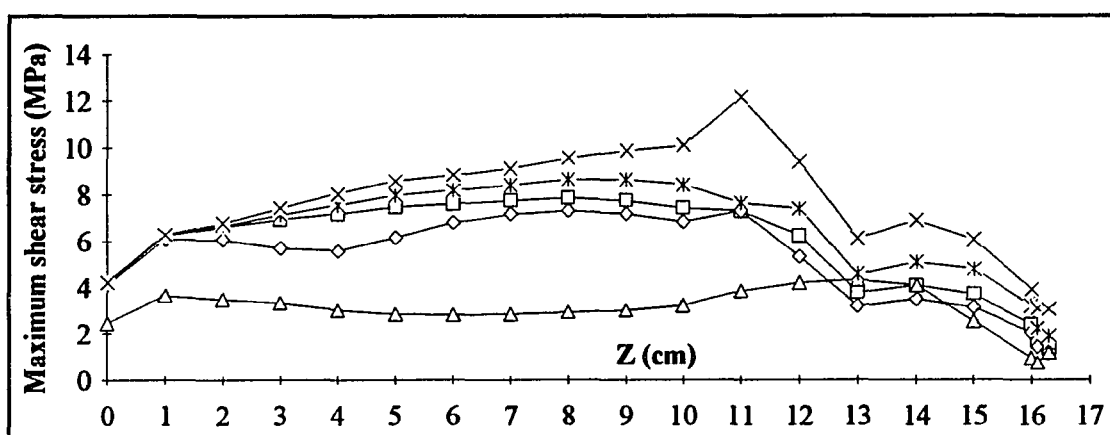
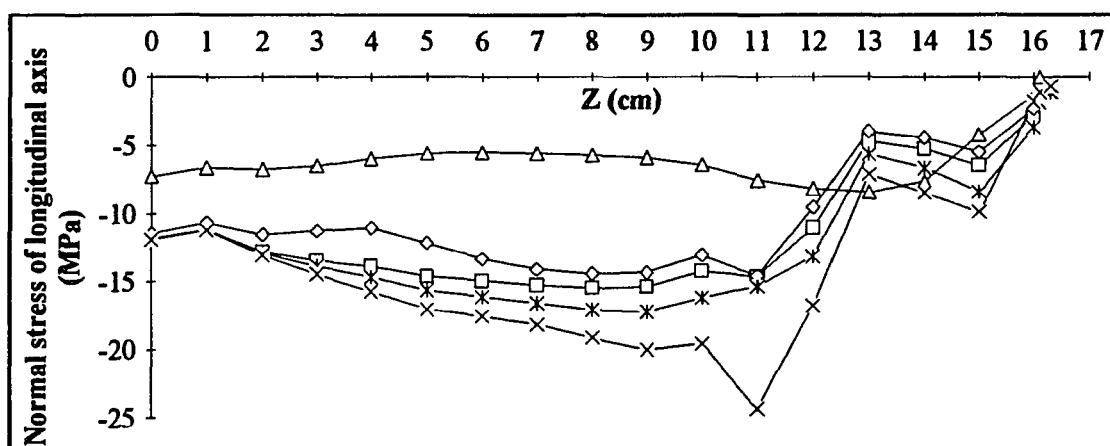
STRESS PATTERNS OF THE FEMUR WITH PROSTHESIS



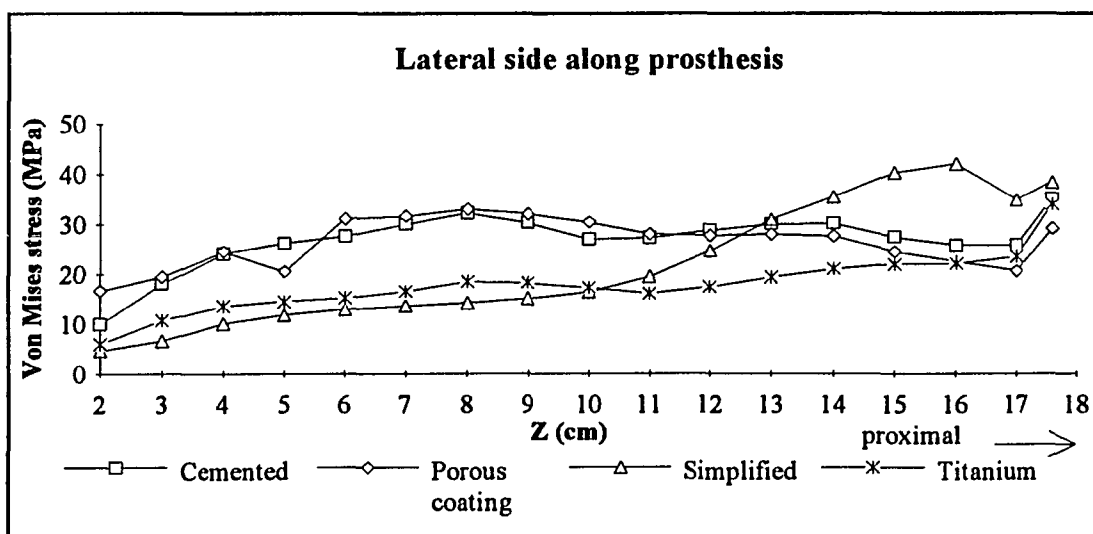
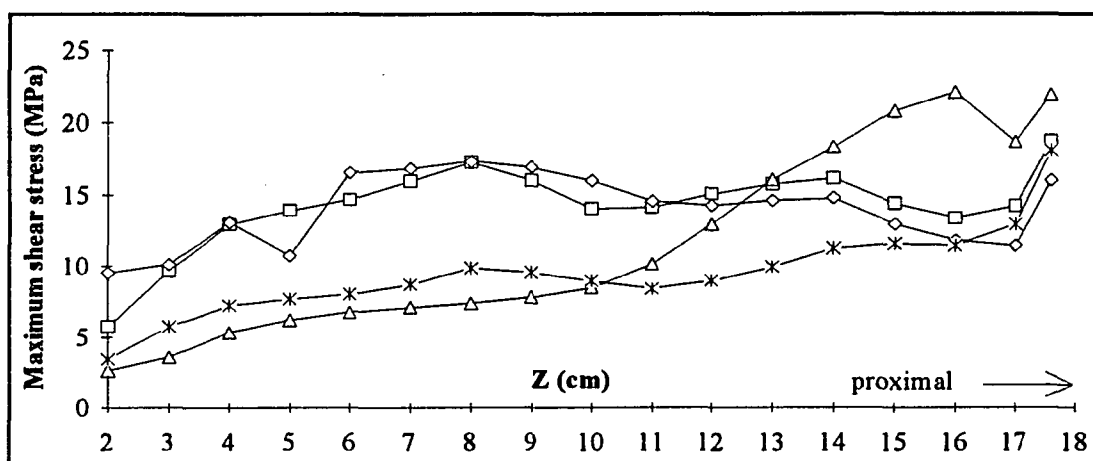
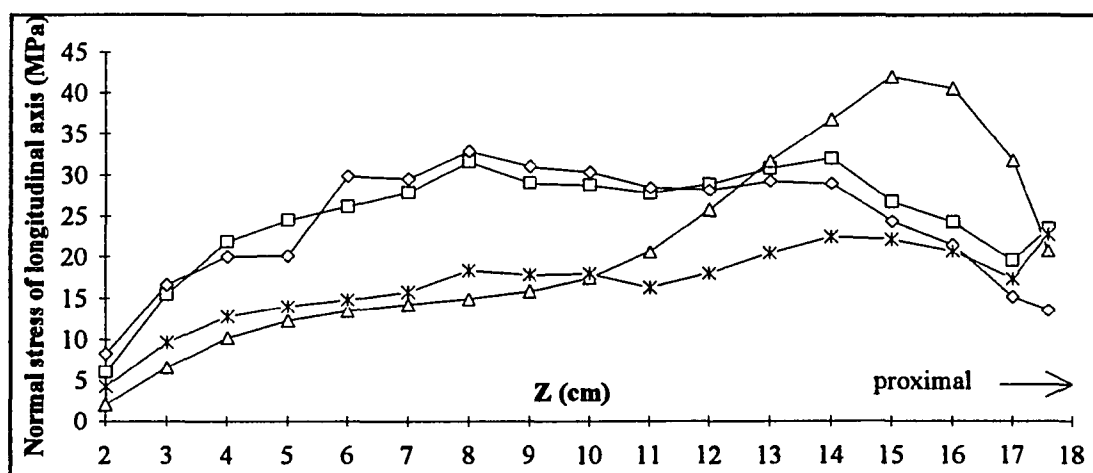
Appendix A1 The stress distributions of medial side along prosthetic stem surface.



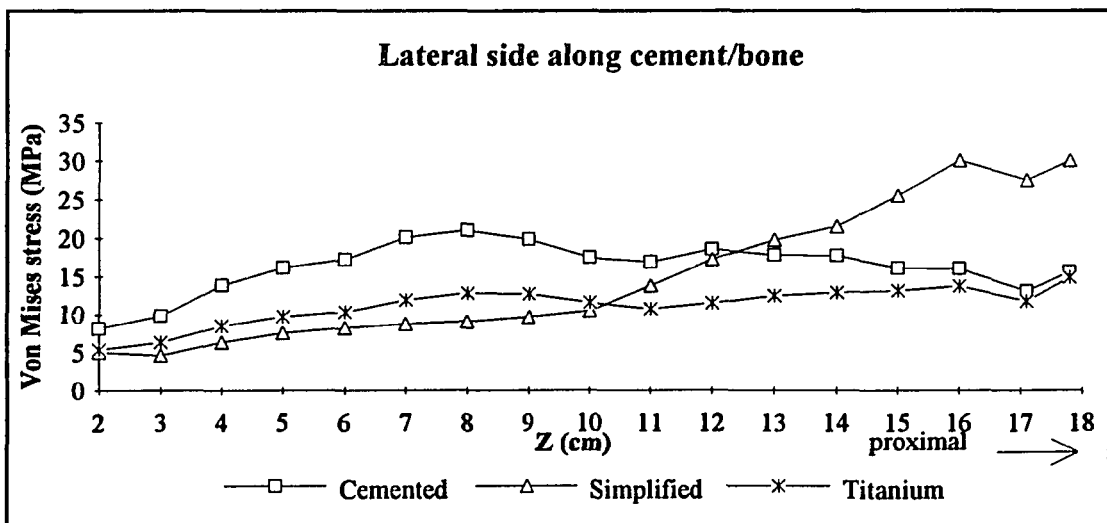
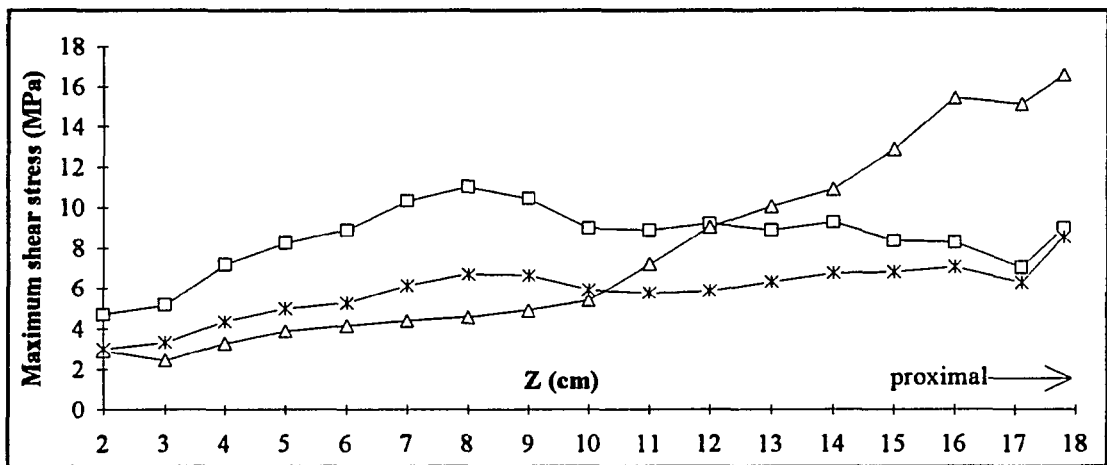
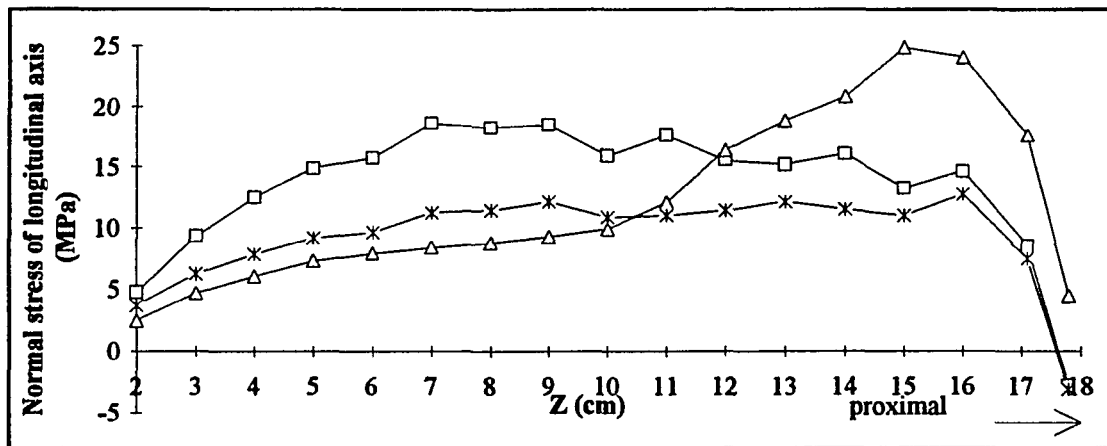
Appendix A2 The stress distributions of medial side along the interface between cement and bone.



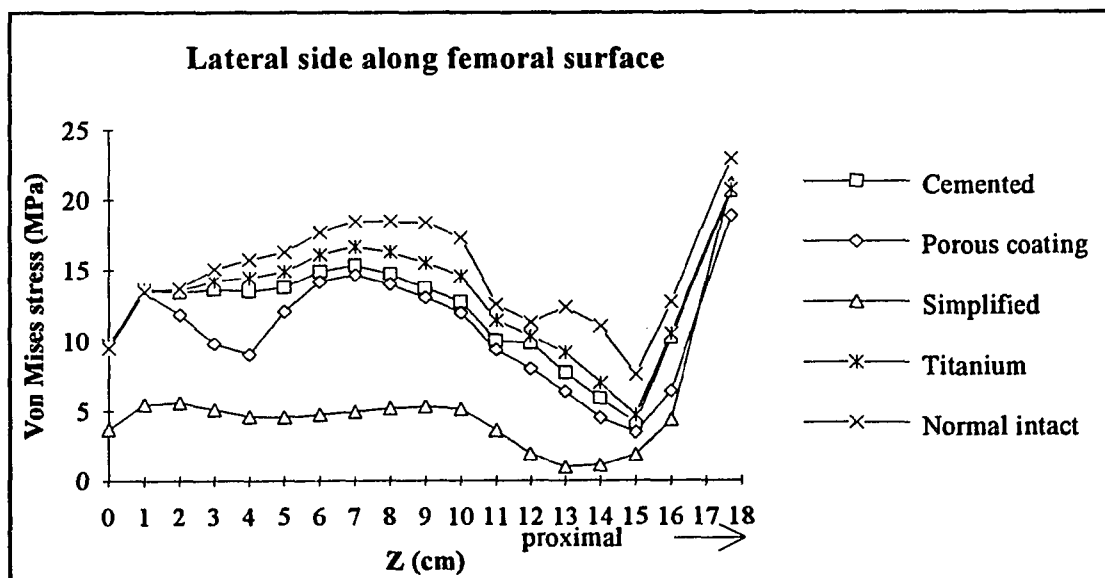
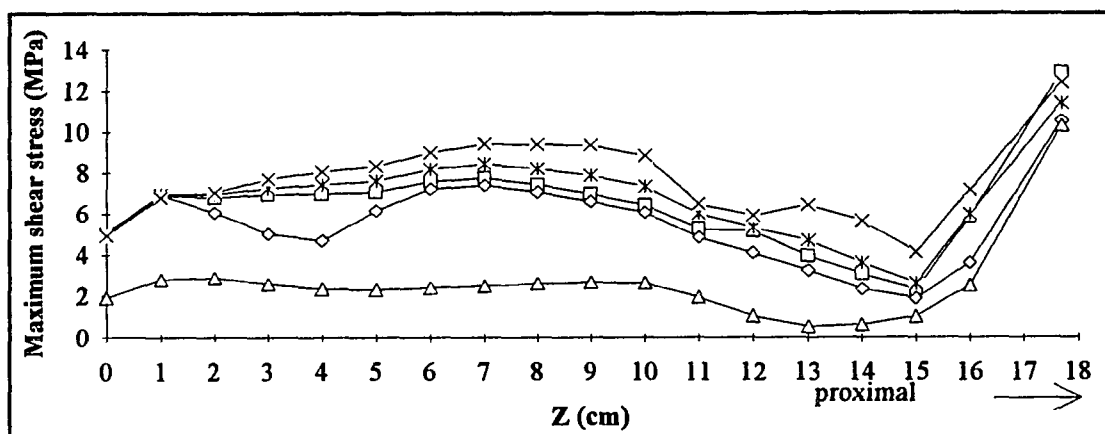
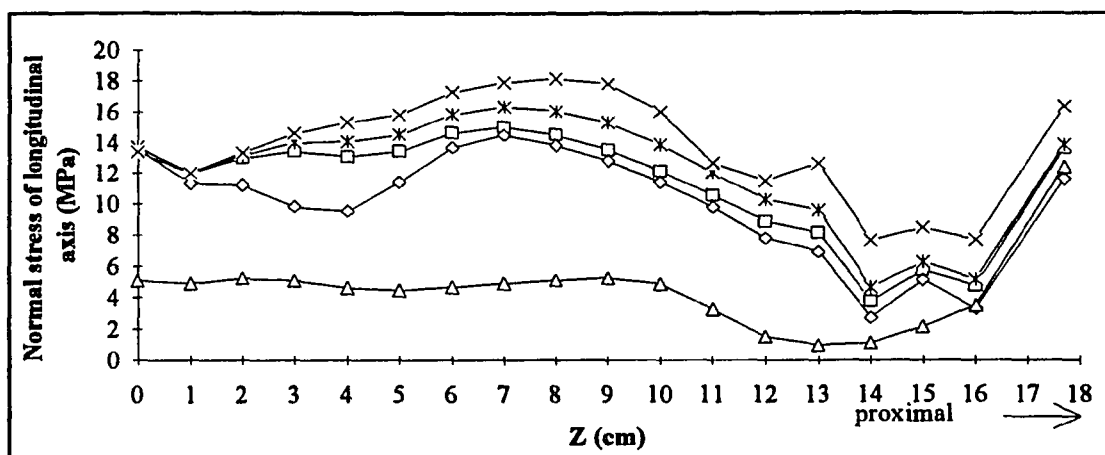
Appendix A3 The stress distributions of medial side along femoral surface.



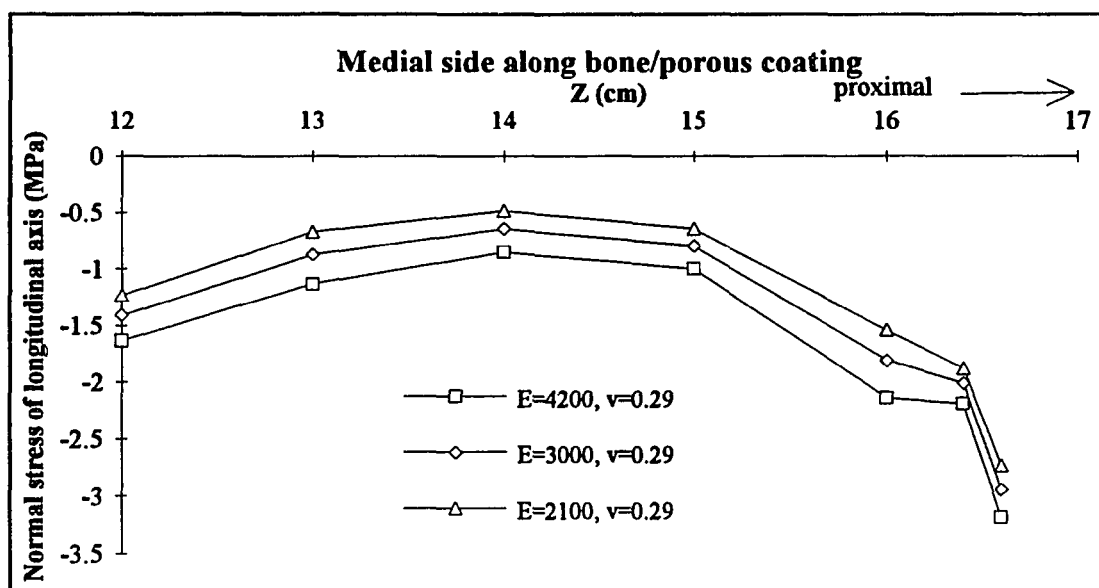
Appendix A4 The stress distributions of lateral side along prosthetic stem surface.



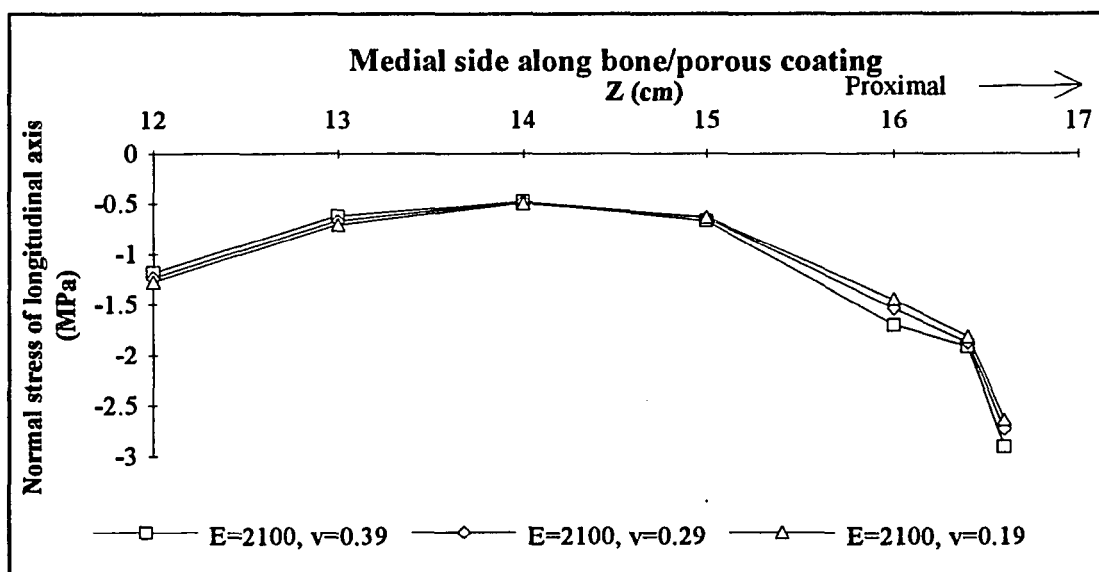
Appendix A5 The stress distributions of lateral side along the interface between cement and bone.



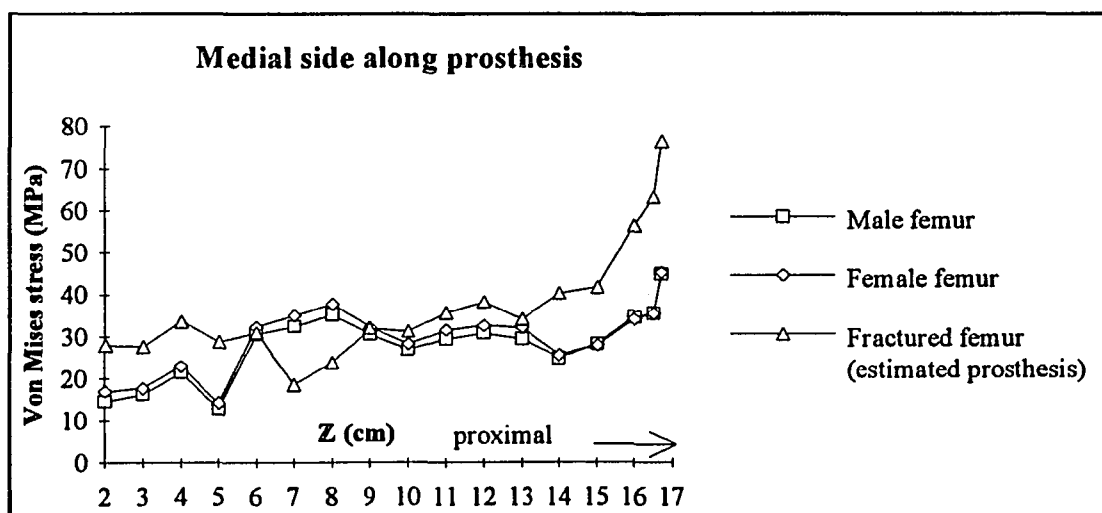
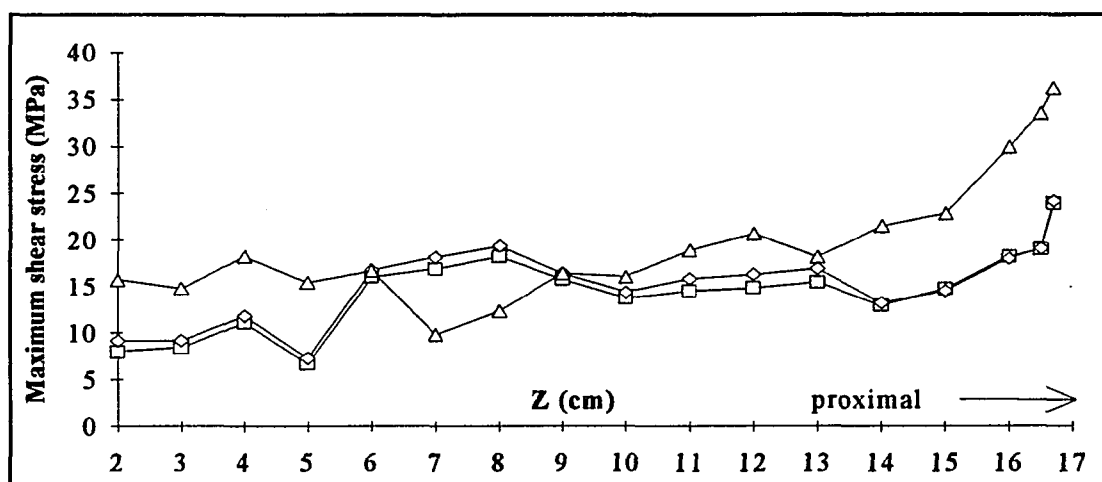
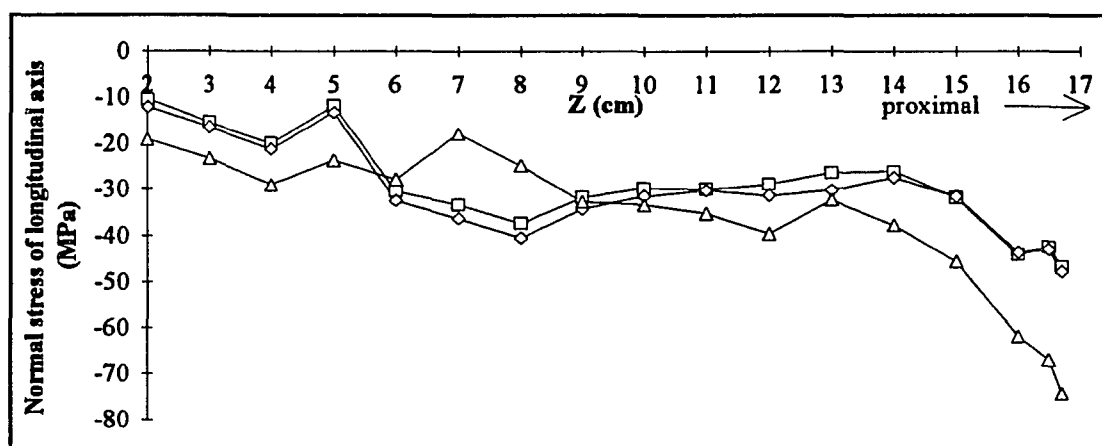
Appendix A6 The stress distributions of lateral side along femoral surface.



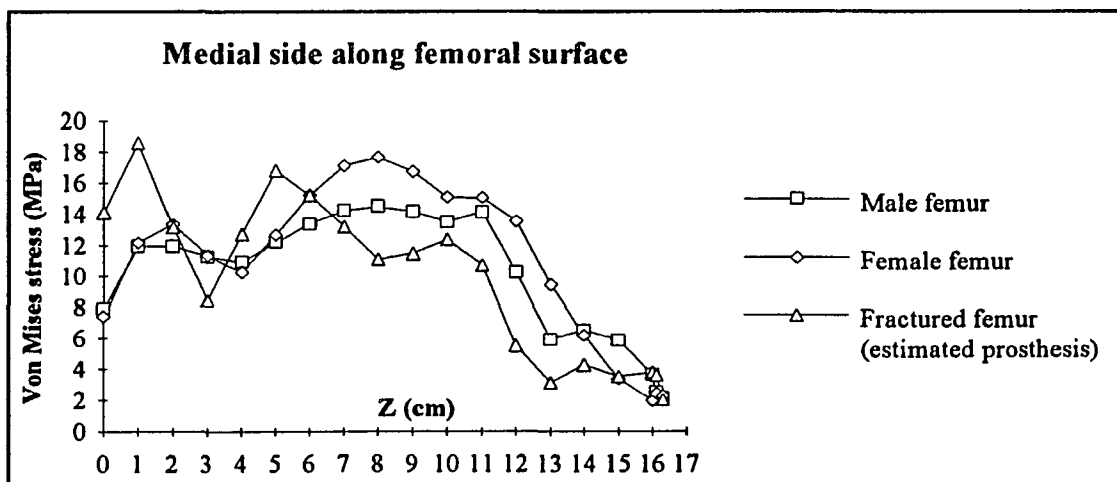
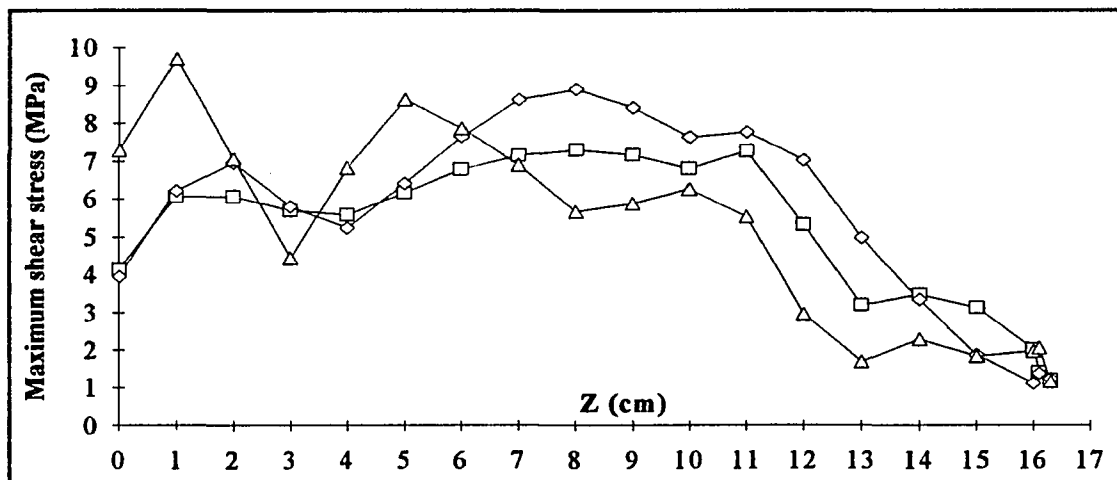
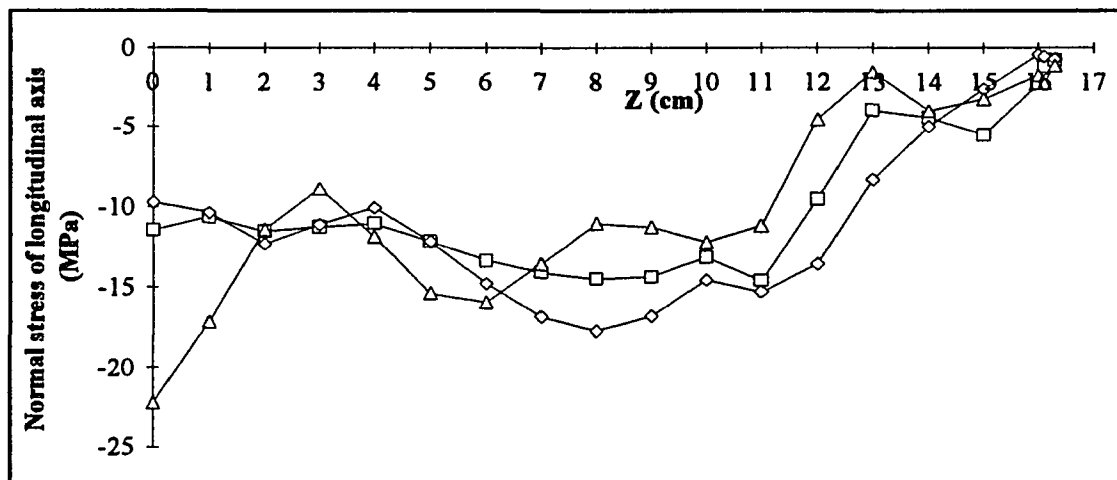
Appendix A7 The effects of porous coating modulus decreases on longitudinal normal stress developed in the neighboring proximal-medial cancellous bone.



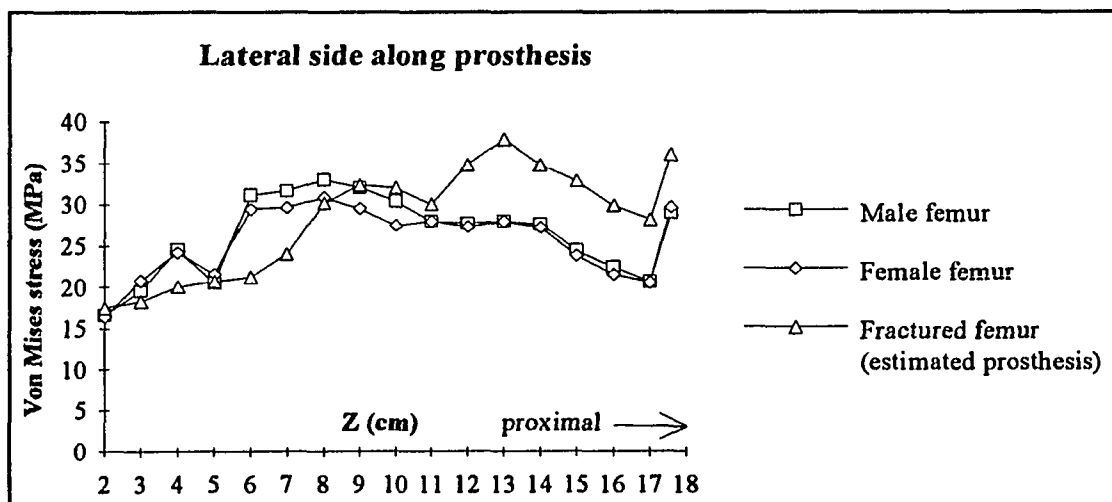
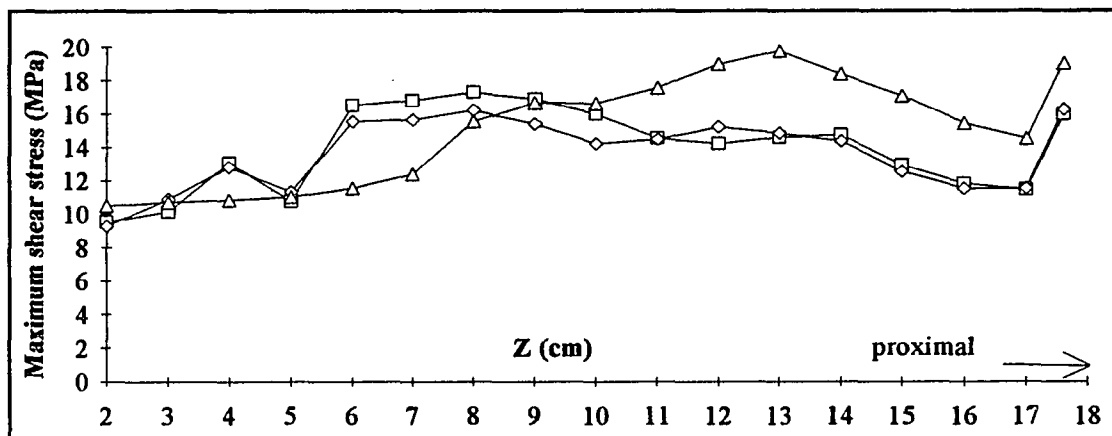
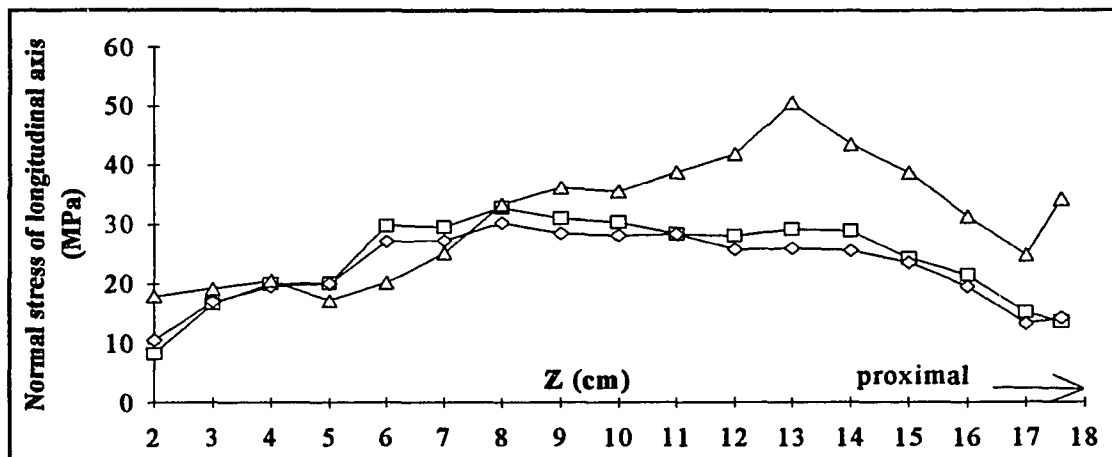
Appendix A8 The effects of porous coating layer compressibility on longitudinal normal stress developed in the neighboring proximal-medial cancellous bone.



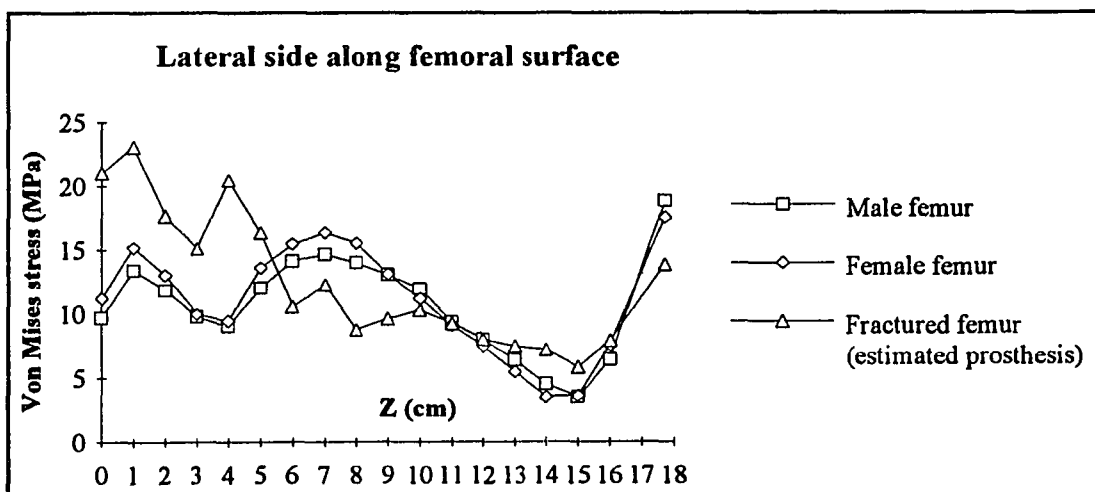
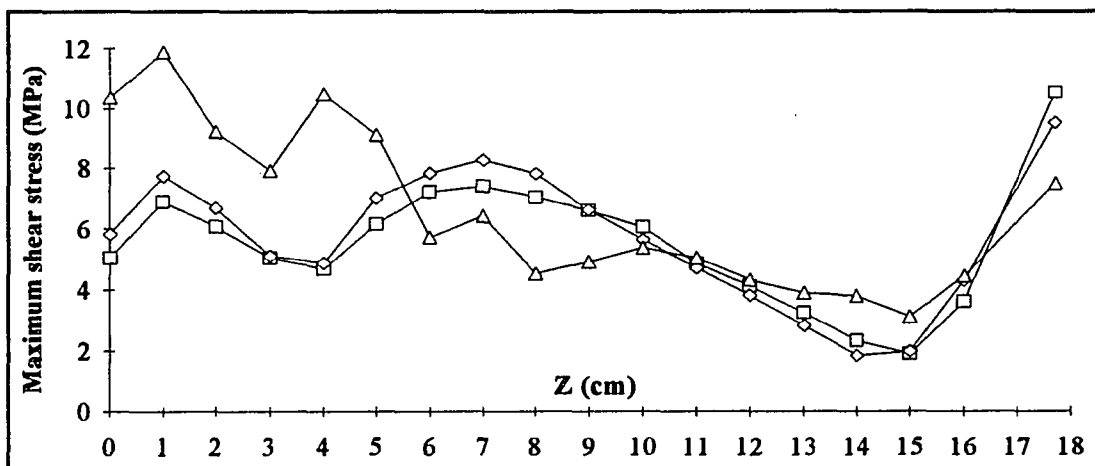
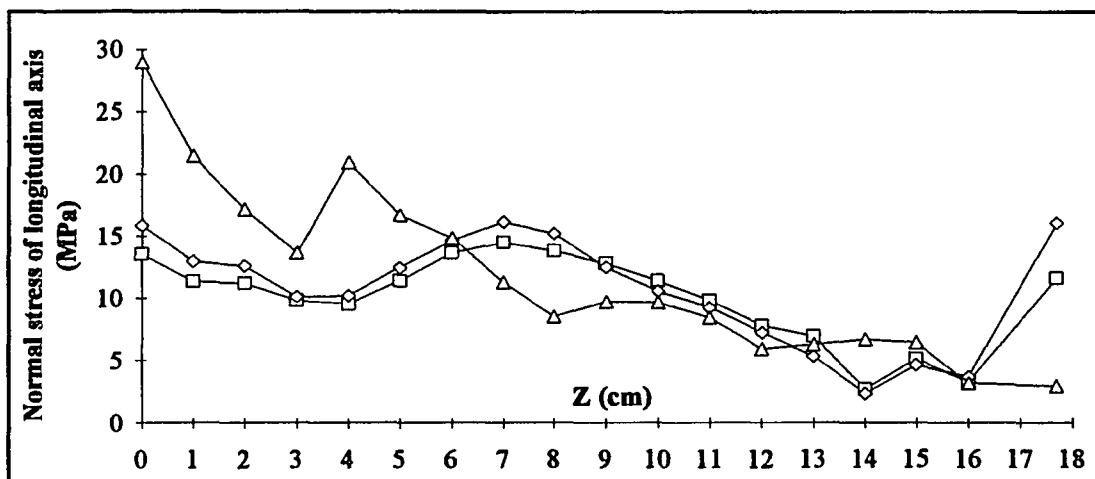
Appendix A9 The stress distributions for normal shape femora (Case 1, 2) and fractured femur (Case 3) along medial prosthetic stem surface.



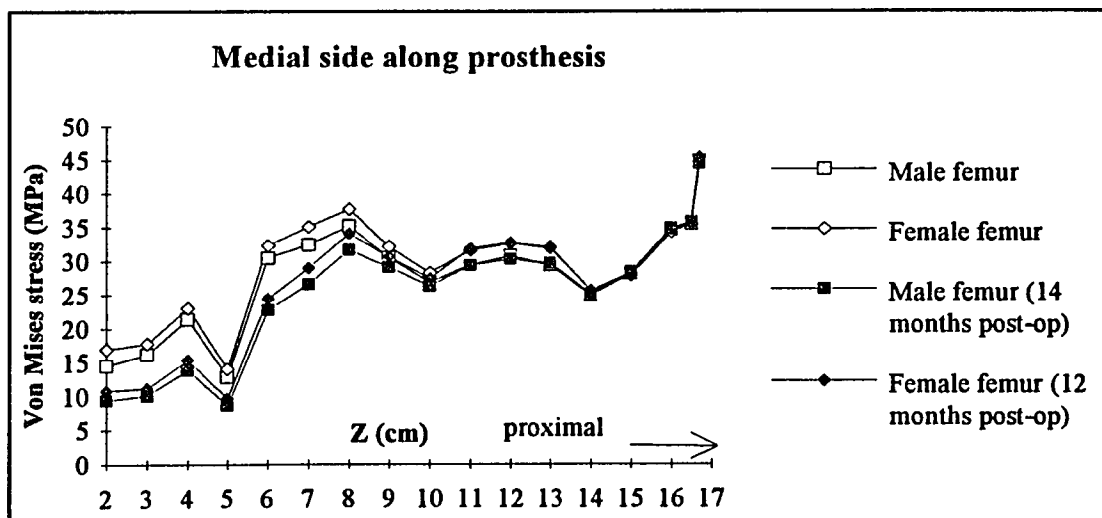
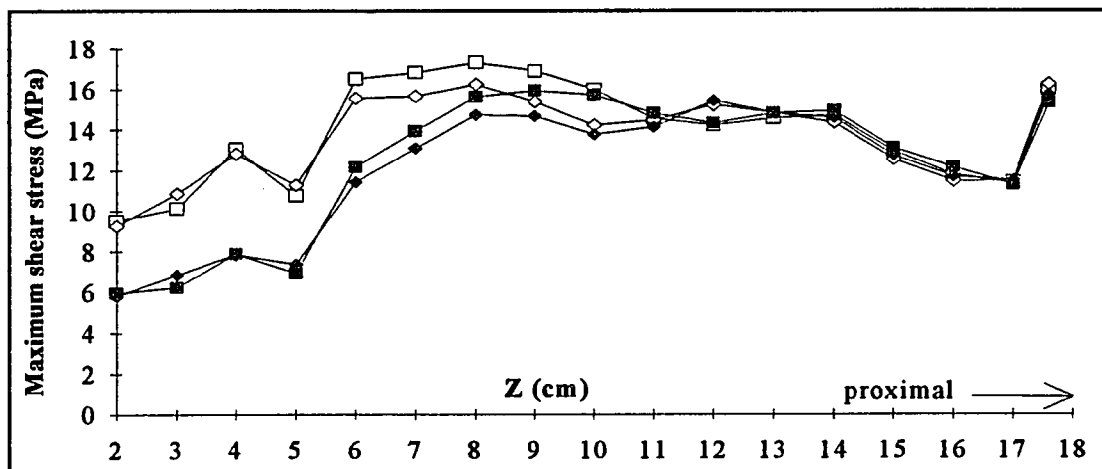
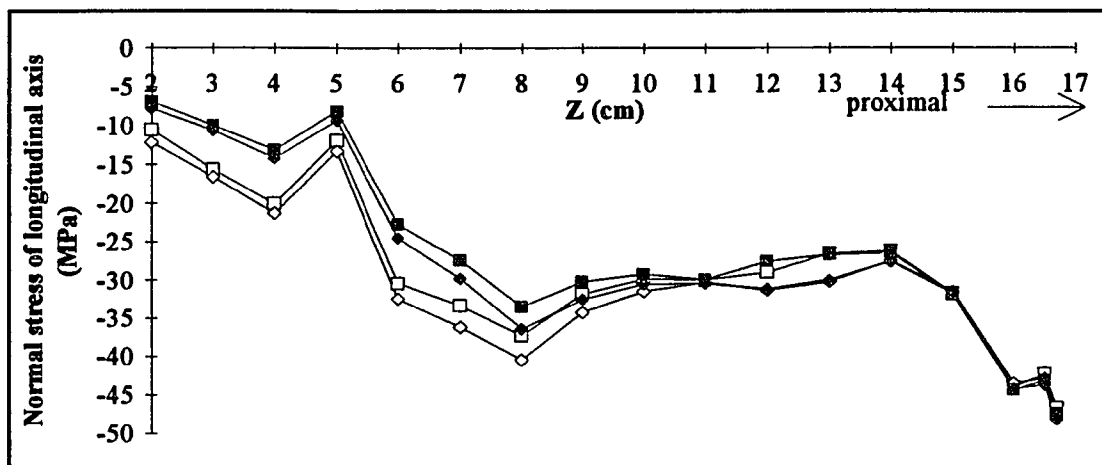
Appendix A10 The stress distributions for normal shape femora (Case 1, 2) and fractured femur (Case 3) along medial femoral surface.



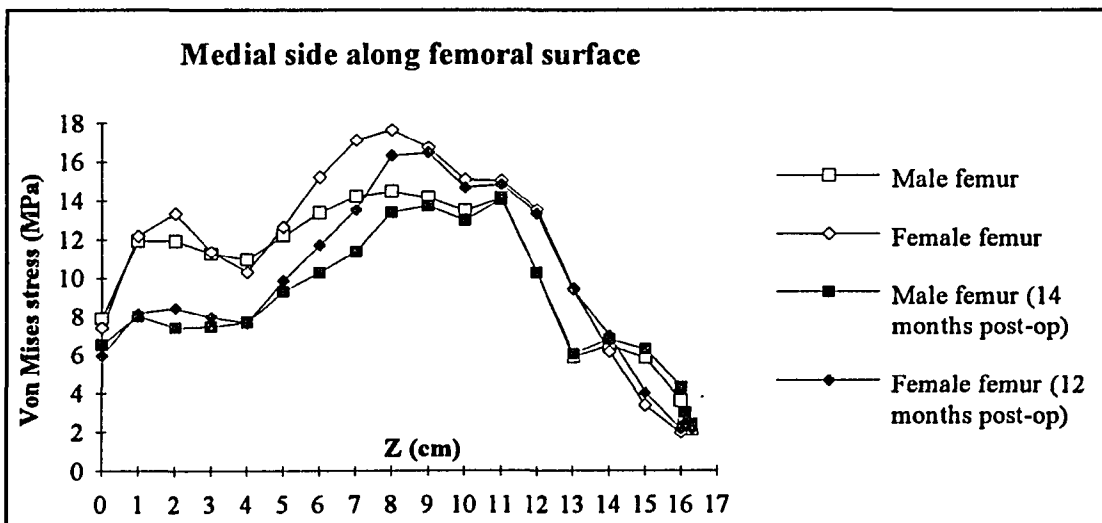
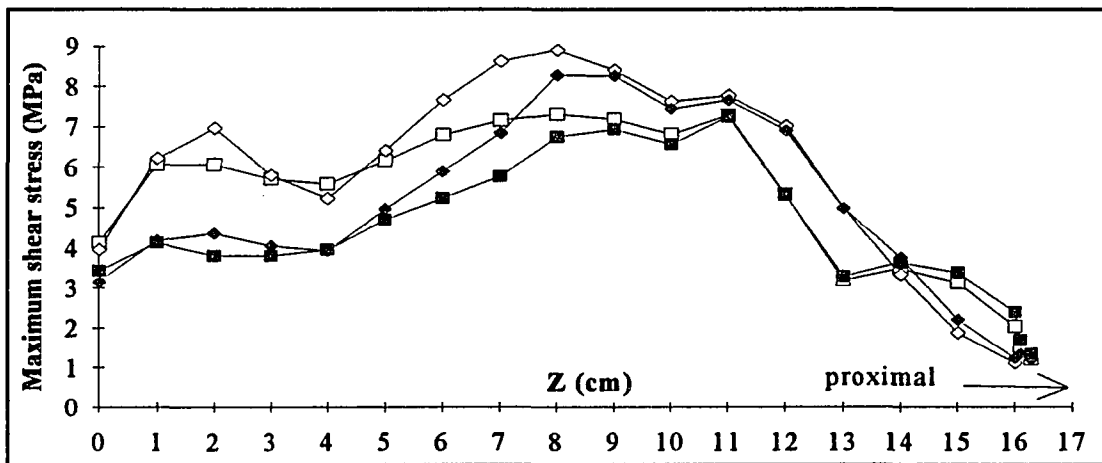
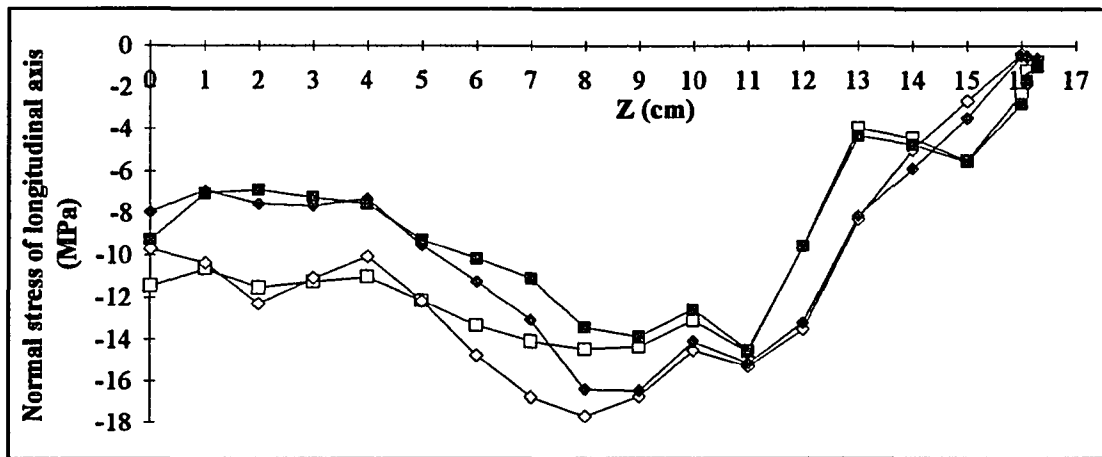
Appendix A11 The stress distributions for normal shape femora (Case 1, 2) and fractured femur (Case 3) along lateral prosthetic stem surface.



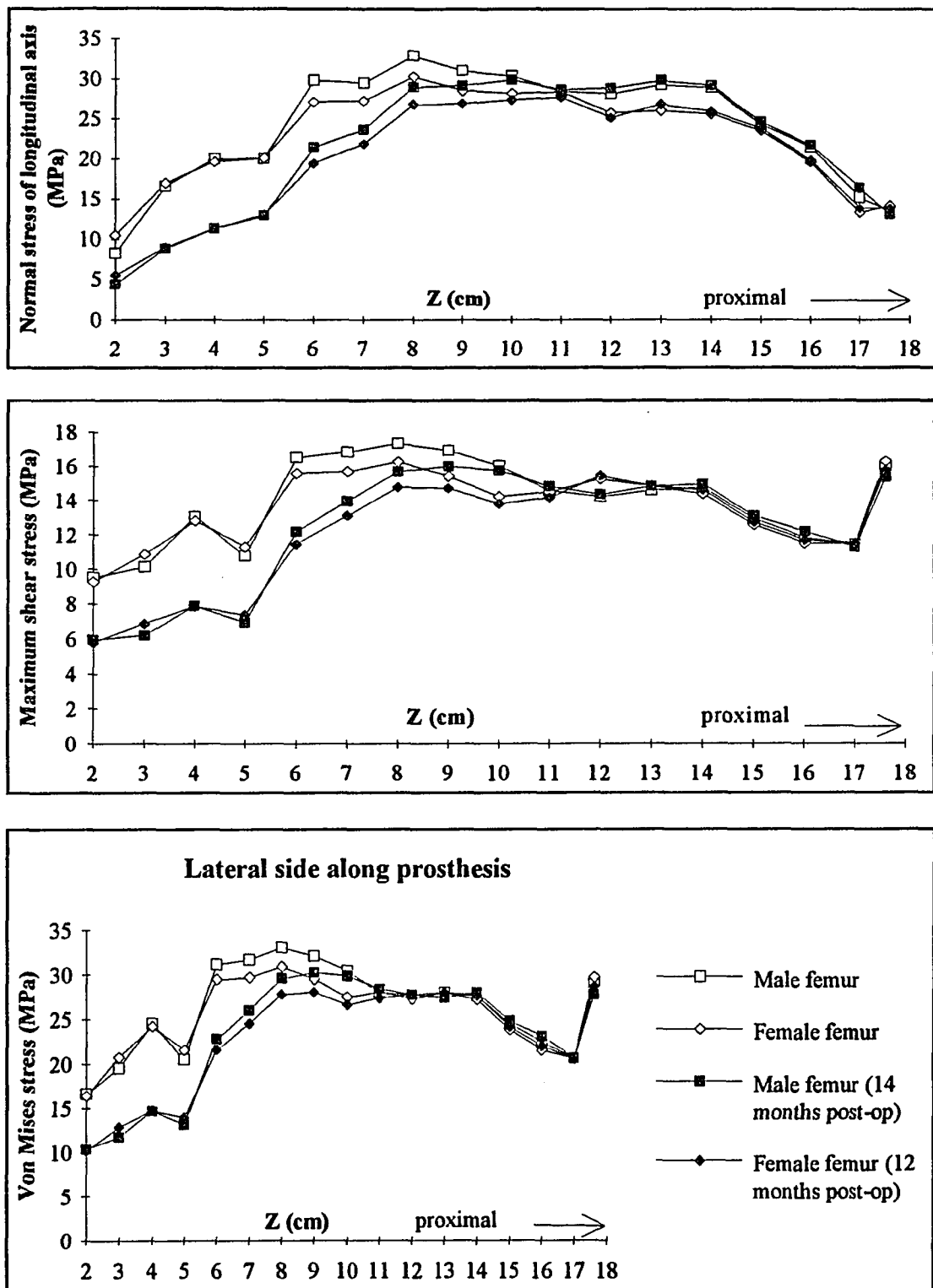
Appendix A12 The stress distributions for normal shape femora (Case 1, 2) and fractured femur (Case 3) along lateral femoral surface.



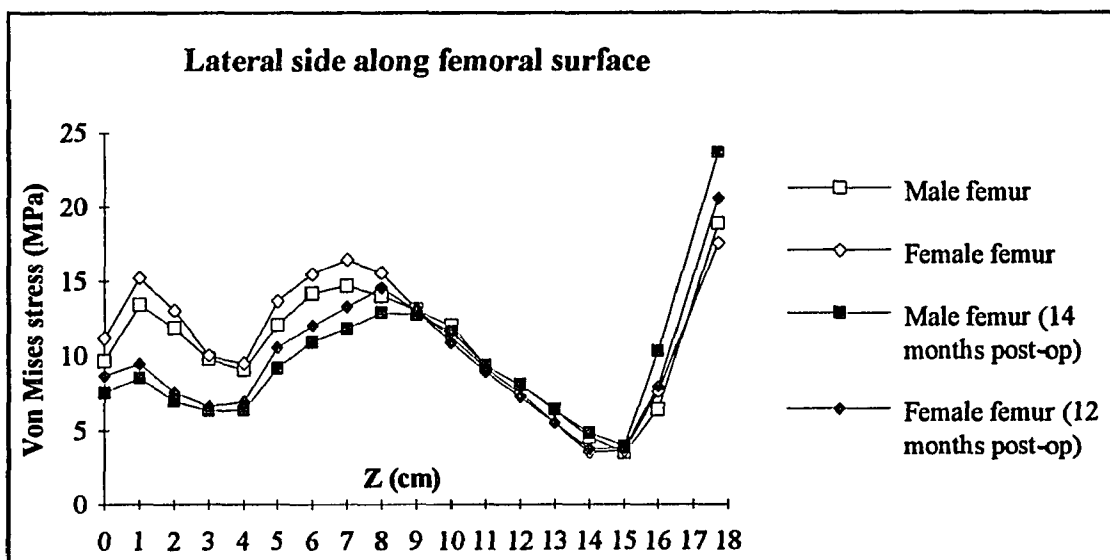
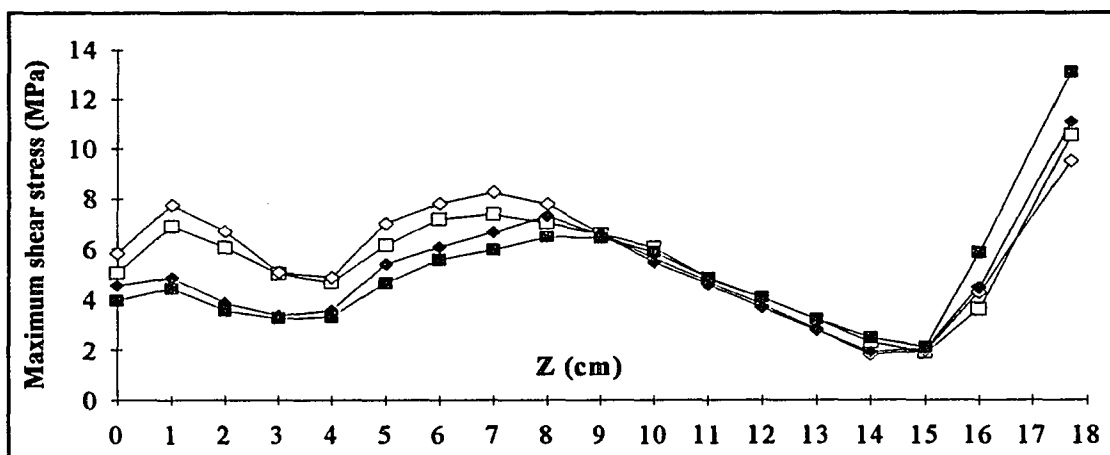
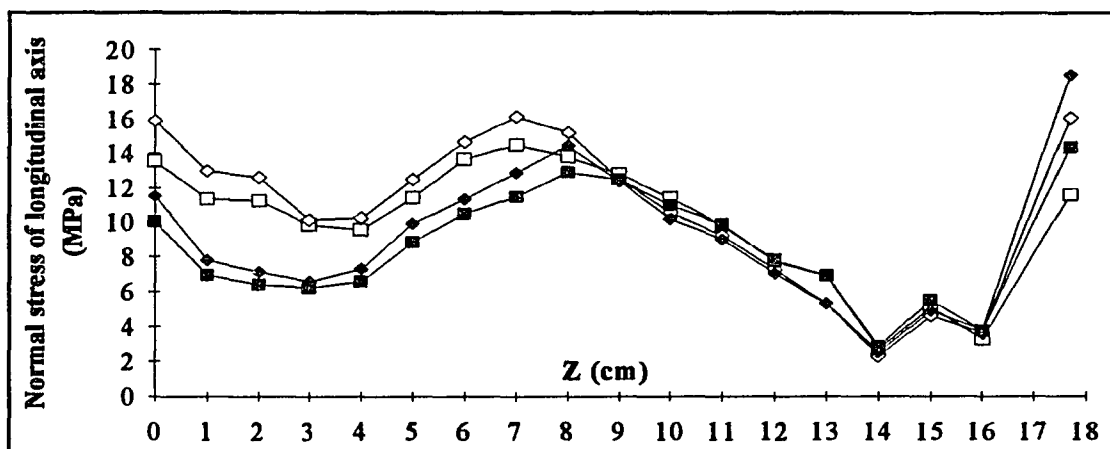
Appendix A13 The stress distributions for preoperation and postoperation of normal shape femora (Case 1, 2) along medial prosthetic stem surface.



Appendix A14 The stress distributions for preoperation and postoperation of normal shape femora (Case 1, 2) along medial femoral surface.



Appendix A15 The stress distributions for preoperation and postoperation of normal shape femora (Case 1, 2) along lateral prosthetic stem surface.



Appendix A16 The stress distributions for preoperation and postoperation of normal shape femora (Case 1, 2) along lateral femoral surface.

APPENDIX B

FORMULATION OF FINITE ELEMENT METHOD

ANSYS finite element program is developed using finite element method employing matrix displacement method based on the energy principle. According to the principle of virtual work,

$$\delta U = \delta V \quad (\text{B.1})$$

Here δU is the total strain energy given by

$$\delta U = \int_v \delta \epsilon^T \sigma dv \quad (\text{B.2})$$

and δV is total potential energy given by

$$\delta V = (\delta u)^T F + \int_v \delta u^T b dv + \int_A \delta u^T s dA \quad (\text{B.3})$$

Where u , F , b and s are nodal displacement, external force, body force and surface traction vectors, respectively. u^T , v and A represent the transpose of the u vector matrix, volume of element and area of element.

Substituting equations (B.2) and (B.3) into equation (B.1), one obtains the following equilibrium equations.

$$\int_v (\delta \epsilon)^T \sigma dv = (\delta u)^T F + \int_v \delta u^T b dv + \int_A \delta u^T s dA \quad (\text{B.4})$$

$$\text{Let } u = N\alpha^e \quad (\text{B.5})$$

Here N and α^e are shape function matrix and the nodal displacement.

Let us begin by relating the strain vector ϵ to the vector of nodal unknowns α^e (i. e., the nodal displacements), or

$$\epsilon = Lu = LN\alpha^e \quad (\text{B.6})$$

Let us refer to the matrix LN as the strain-nodal displacement matrix and denote it by B , or

$$B = LN \quad (\text{B.7})$$

Therefore, equation (B.6) may be written as

$$\varepsilon = Ba^e \quad (B.8)$$

L is a linear operator matrix that contains first derivatives with respect to only x and y . If the shape function is linear functions (in x and y), then the matrix B contains only constants. In any event, B does not contain any of the nodal displacements, which implies that

$$\delta\varepsilon = \delta(Ba^e) = B\delta a^e \quad (B.9)$$

$$\text{and } (\delta\varepsilon)^T = (B\delta a^e)^T = B^T(\delta a^e)^T \quad (B.10)$$

Similarly, we have

$$\delta u = \delta(Na^e) = N\delta a^e \quad (B.11)$$

$$\text{and } (\delta u)^T = (N\delta a^e)^T = N^T(\delta a^e)^T \quad (B.12)$$

Substituting the results from equations (B.9)-(B.12) into equation (B.4)

$$\int_V (\delta a^e)^T B^T \sigma dv = (\delta a^e)^T N^T F + \int_V (\delta a^e)^T N^T b dv + \int_A (\delta a^e)^T N^T s dA \quad (B.13)$$

$$\Rightarrow (\delta a^e)^T \left\{ \int_V B^T \sigma dv - N^T F - \int_V N^T b dv - \int_A N^T s dA \right\} = 0 \quad (B.14)$$

But the term in braces must be zero because $(\delta a^e)^T$ is not necessarily zero and is quite arbitrary. δa^e is arbitrary because it represents arbitrary virtual displacements.

$$\therefore \int_V B^T \sigma dv - N^T F - \int_V N^T b dv - \int_A N^T s dA = 0 \quad (B.15)$$

For linear elastic material the stress-strain relationship is:

$$\sigma = D(\varepsilon - \varepsilon_0) + \sigma_0 \quad (B.16)$$

Where the material property matrix D contains pertinent material properties such as the elastic modulus and Poisson's ratio. ε_0 and σ_0 represent the self-strain vector and the prestress vector respectively.

We may write the following equation from equations B.15 and B.16.

$$\int_V B^T D \varepsilon dv - \int_V B^T D \varepsilon_0 dv + \int_V B^T D \sigma_0 dv - N^T F - \int_V N^T b dv - \int_A N^T s dA = 0 \quad (B.17)$$

$$\Rightarrow \left\{ \int_V B^T D B dv \right\} a^e - \int_V B^T D \varepsilon_0 dv + \int_V B^T D \sigma_0 dv - \int_V N^T b dv - \int_A N^T s dA = N^T F \quad (B.18)$$

Finally we get an equation of the form

$$Ku + f = F \quad (\text{B.19})$$

$$\text{where } K = \int_v B^T DB dv$$

$$f = -\int_v N^T b dv - \int_A N^T s dA - \int_v B^T D \epsilon_0 dv + \int_v B^T \sigma_0 dv$$

$$F = N^T F$$

Equation (B.19) can be rewritten in partitioned matrix form:

$$\begin{bmatrix} K_{ii} & K_{ib} \\ K_{bi} & K_{bb} \end{bmatrix} \begin{bmatrix} u_i \\ u_b \end{bmatrix} = \begin{bmatrix} F_i \\ F_b \end{bmatrix} - \begin{bmatrix} f_i \\ f_b \end{bmatrix} \quad (\text{B.20})$$

The subscripts i and b are used to refer the degrees of freedom that are free and imposed displacements, respectively. The first part of equation (B.20) may be solved for basic unknowns $\{u_i\}$.

$$\{u_i\} = -[K_{ii}]^{-1} [K_{ib}] \{u_b\} + [K_{ii}]^{-1} \{R_i\} \quad (\text{B.21})$$

where $R = F - f$

BIBLIOGRAPHY

1. *ANSYS Engineering Analysis System User's Manual*, Swanson Analysis Systems, Huston, PA., 1990.
2. Andrews, J. G., E. Y. S. Chao, R. C. Johnston, and D. N. Stauffer. "A General Method for Accurate Kinematic Analysis of Biomechanical Systems in Motion." *Annual Meeting of the Orthopaedic Research Society*, Jan, 1972, PP. 28-29.
3. Andriacchi, T. P., S. C. J. Hampton, A. B. Schultz, and J. O. Galante. "Three-Dimensional Coordinate Data Processing in Human Motion Analysis." *Journal of Biomechanical Engineering*, Vol. 101, 1979, PP. 279-283.
4. Ashman, R. B., S. C. Cowin, W. C. Van Buskirk. "A Continuous Wave Technique for The Measurement of The Elastic Properties of Cortical Bone." *Journal of Biomechanics*, Vol. 17(5), 1984, PP. 349-361.
5. Ashman, R. B. "Elastic Modulus of Trabecular Bone Material." *Journal of Biomechanics*, Vol. 18, 1988, PP. 177-181.
6. Bartel, D. L., V. L. Bicknell, and T. M. Wright. "The Effect of Conformity, Thickness, and Material on Stresses in Ultra-High Molecular Weight Componets for Total Joint Replacement." *The Journal of Bone and Joint Surgery*, Vol. 68A, 1986, PP. 1041-1051.
7. Bartel, D. L., A. H. Burstein, E. A. Santavicca, and J. N. Insall. "Performance of The Tibial Component in Total Knee Replacement." *The Journal of Bone Joint Surgery*, 1982, PP. 1026-1033.
8. Beaupre, G. S., R. Vasu, D. R. Carter, and D. J. Schurman. "Epiphyseal-Based Designs for Tibial Plateau Components — II. Stress Analysis in The Sagittal Plane." *Journal of Biomechanics*, Vol. 19(8), 1986, PP. 663-673.
9. Bechtold, J. E., and D. R. Riley. "Application of Beams on Elastic Foundation and B-Spine Solution Methodologies to Parametric Analysis of Intramedullary Implant Systems." *Journal of Biomechanics*, Vol. 24(6), 1991, PP. 441-448.
10. Bensusan, J. S., D. T. Davy, and K. G. Haiple. "Tensile Compressive and Torsional Testing of Cancellous Bone." *Transactions 29th Annual Ors. March*, 1983, PP. 132.
11. Beaudoin, Jr, A. J., W. M. Mihalko, W. R. Krause, and J. A. Cardea. "FEM Study of Fracture Fixation Distal to A Femoral Prosthesis." *Transaction Ors. Res. Soc.*, Vol. 14, 1989, PP. 406-413.

BIBLIOGRAPHY (Continued)

12. Black, J. B. *Orthopaedic Biomaterials in Research and Practice*. Churchill Livingstone Book Co., New York, 1988, PP. 267-330.
13. Bloebaum, R. D., D. L. Dorr, and D. Moynes. *Technical Monograph: The APR Universal Hip System with Cancellous Structured Titanium*. Centinela Hospital Medical Center Press, CA., 1984.
14. Bogumill, G. P., and H. A. Schwamm. *Orthopaedic Pathology*. New York, 1984, PP. 36-43.
15. Borg, S. F. *Matrix-Tensor Methods in Continuum Mechanics*. D Van Nostrand, Inc., NJ., 1963, PP. 1-192.
16. Brown, I. W., and P. A. Ring. "Osteolytic Changes in The Upper Femoral Shaft Following Porous-Coated Hip Replacement." *The Journal of Bone and Joint Surgery*, Vol. 67B, 1985, PP. 218-221.
17. Brown, T. D., and D. R. Pedersen. "Global Mechanical Consequences of Reduced Cement/Bone Coupling Rigidity in Proximal Femoral Arthroplasty: A Three-Dimensional Finite Element Analysis." *Journal of Biomechanics*, Vol. 21(2), 1988, PP. 115-129.
18. Burke, D. W., D. O. O'Connor, E. B. Zalensky, M. Jasty, and W. H. Harris. "Micromotion of Cemented and Uncemented Femoral Components." *The Journal of Bone and Joint Surgery*, Vol. 73B, 1991, PP. 33-37.
19. Burr, D. B. and T. Stafford. "Validity of The Bulk-Straining Technique to Separate Artifacts from in Vivo Bone Microdamage." *Clinical Orthopaedics and Related Research*, Vol. 260, 1990, PP. 305-308.
20. Bushong, S. C. *Radiologic Science for Technologists*. C. V. Mosby, Co., Missouri, 1988, PP. 385-408.
21. Carnahan, B., H. A. Luther, and J. O. Wilkes. *Applied Numerical Methods*. John Wiley & Sons, Inc. 1982, PP. 571-573.
22. Carter, D. R., and W. C. Hayes. "The Compressive Behavior of Bone As a Two-Phase Porous Structure." *The Journal of Bone and Joint Surgery*, Vol. 59A, 1977 PP. 954-962.

BIBLIOGRAPHY (Continued)

23. Carter, D. R., T. E. Orr, and D. P. Fyhrie. "Relationships Between Loading History and Femoral Cancellous Bone Architecture." *Journal of Biomechanics*, Vol. 22(3), 1989, PP. 231-244.
24. Carter, D. R., and R. Vasu. "Stress Changes in The Femoral Head Due to Porous Ingrowth Surface Replacement Arthroplasty." *Journal of Biomechanics*, Vol. 17(10), 1984, PP. 737-747.
25. Carter, D. R., M. Wong, and T. E. Orr. "Musculoskeletal Ontogeny, Phylogeny and Functional Adaptation." *Journal of Biomechanics*, Vol. 24(1), 1991, PP. 3-16.
26. Cheal, E. J., M. Spector, and W. C. Hayes. "Role of Loads and Prosthesis Material Properties on the Mechanics of Proximal Femur after Total Hip Arthroplasty." *Journal of Orthopaedic Research*, Vol. 10, 1992, PP. 405-422.
27. Cook, R. D. "*Concepts and Applications of Finite Element Analysis*." John Wiley & Sons, New York, 1981.
28. Cook, S. D., and K. A. Thomas. "Fatigue Failure of Noncemented Porous-Coated Implants." *The Journal of Bone and Joint Surgery*, Vol. 73B, 1991, PP. 20-24.
29. Cowin, S. C. *Bone Mechanics*. CRC Press, Inc., Florida, 1989, PP. 75-159.
30. Cowin, S. C. "Bone Remodeling of Diaphyseal Surfaces By Torsional Loads: Theoretical Predictions." *Journal of Biomechanics*, Vol. 20, 1987, PP. 1111-1120.
31. Cowin, S. C. "Mechanical Modeling of the Stress Adaptation Process in Bone." *Calcified Tissue International*, Vol. 36, 1984, PP. S98-S103.
32. Cowin, S. C. "Torsion Cylinders with Shape Intrinsic Orthotropy." *Journal of Applied Mechanics*, Vol. 109, 1987, PP. 778-782.
33. Cowin, S. C., R. T. Hart, J. R. Balser, and D. H. Kohn. "Functional Adaptation in Long Bones: Establishing in Vivo Values for Surface Remodeling Rate Coefficients." *Journal of Biomechanics*, Vol. 18, 1985, PP. 665-684.
34. Crowninshield, R. D., R. A. Brand, R. C. Johnston, and J. C. Milroy. "An Analysis of Femoral Component Stem Design in Total Hip Arthroplasty." *The Journal of Bone and Joint Surgery*, Vol. 62A, 1980, PP. 68-78.

BIBLIOGRAPHY (Continued)

35. Crowninshield, R. D., R. A. Brand, R. C. Johnston, and D. R. Pedersen. "An Analysis of Collar Function and the Use of Titanium in Femoral Prostheses." *Clinical Orthopaedics and Related Research*, July-August 1981, PP. 270-277.
36. Crowninshield, R. D., R. C. Johnston, J. G. Andrews, and R. A. Brand. "A Biomechanical Investigation of The Human Hip." *Journal of Biomechanics*, Vol. 11, 1978, PP. 75-85.
37. Currey, J. D. "The Effect of Porosity and Mineral Content on The Young's Modulus of Elasticity of Compact Bone." *Journal of Biomechanics*, Vol. 21, 1988, PP. 131-139.
38. Currey, J. D. "Physical Characteristics Affecting The Tensile Failure Properties of Compact Bone." *Journal of Biomechanics*, Vol. 22, 1990, PP. 837-844.
39. Davy, D. T., G. M. Kotzar, R. H. Brown, K. G. Heiple, V. M. Goldberg, and A. H. Burstein. "Telemetric Force Measurements across The Hip after Total Arthroplasty." *The Journal of Bone and Joint Surgery*, Vol. 70A, January 1988, PP. 45-50.
40. Dawson, J. M., and D. L. Bartel. "Consequence of An Interface Fit on The Fixation of Porous-Coated Tibial Components in Total Knee Replacement." *The journal of Bone and Joint Surgery*. Vol. 74A, February, 1992, PP. 233-238.
41. Dorr, L. D. *Surgical Technique: The APR Universal Hip System with Cancellous Structured Titanium*. Rancho Los Amigos Hospital Press, CA., 1985.
42. *Dual-Lock: Total Hip System*. Manufacture's Manual, Depuy Co., Indiana, 1984.
43. Ducheyne, P., and G. W. Hasting. *Functional Behavior of Orthopaedic Biomaterials*. CRC Press, Inc., Florida, 1984, PP.51-99.
44. Duparc, J., and P. Massin. "Results of 203 Total Hip Replacements Using a Smooth, Cementless Femoral Component." *The Journal of Bone and Joint Surgery*, Vol. 74B, March, 1992, PP. 251-256.
45. *Eclipse Line Computers*, Data General Corporation, No. 014000626, Westboro, MA. August, 1979.
46. Eisenberg, M. A. *Introduction to The Mechanics of Solids*. Addison-Wesley, Inc., MA., 1980, PP. 2-89.

BIBLIOGRAPHY (Continued)

47. Engh, C. A., and J. D. Bobyn. "The Influence of Stem Size and Extent of Porous Coating on Femoral Bone Resorption after Primary Cementless Hip Arthroplasty." *Clinical Orthopaedics and Related Research*, Vol. 231, 1988, PP. 7-28.
48. Engh, C. A., and J. D. Bobyn, and A. H. Glassman. "Porous-Coated Hip Replacement: The Factors Governing Bone Ingrowth, Stress Shielding, and Clinical Results." *The Journal of Bone and Joint Surgery*, Vol. 69B, 1987, PP. 45-55.
49. English, T. A., and M. Kilvington. "In Vivo Records of Hip Loads Using A Femoral Implant With Telemetric Output." *Journal of Biomechanical Engineering*, Vol. 1, 1979, PP. 111-115.
50. Fung, Y. C. *Biomechanics, Mechanical Properties of Living Tissues*. Springer-Verlag, New York, 1981.
51. Fyhrie, D. D., and D. R. Carter. "Femoral Head Apparent Density Distribution Predicted From Bone Stress." *Journal of Biomechanics*, Vol. 23(1), 1990, PP. 1-10.
52. Gallagher, R. H., B. R. Simon, P. C. Johnson, and J. F. Gross. "*Finite Elements in Biomechanics*." John Wiley & Sons Co., New York, 1982.
53. Garg, A., and P. S. Walker. "The Effect of The Interface on The Bone Stresses Beneath Tibial Components." *Journal of Biomechanics*, Vol. 19(12), 1986, PP. 957-967.
54. Gilbert, J. L., R. S. Bloomfeld, E. P. Lautenschlager, and R. L. Wixson. "A Computer-Based Biomechanical Analysis of the Three-Dimensional Motion of Cementless Hip Prostheses." *Journal of Biomechanics*, Vol. 25(4), 1992, PP. 329-340.
55. Goldstein, S. A., D. L. Wilson, P. B. Sonstegard, and L. S. Matthews. "The Mechanical Properties of Human Tibial Trabecular Bone As a Function of Metaphyseal." *Journal of Biomechanics*, Vol. 16(12), 1983, PP. 965-969.
56. Hamilton, W. J. *Textbook of Human Anatomy*. C. V. Mosby, Co., Missouri, 1976, PP 116-221.

BIBLIOGRAPHY (Continued)

57. Hampton, S. J., T. P. Andriacchi, and J. O. Galante. "Three Dimensional Stress Analysis of The Femoral Stem of A Total Hip Prosthesis." *Journal of Biomechanics*, Vol. 13, 1980, PP. 443-448.
58. Harrigan, T. P., and W. H. Harris. "A Three-Dimensional Non-Linear Finite Element Study of The Effect of Cement-Prosthesis Debonding in Cemented Femoral Total Hip Components." *Journal of Biomechanics*, Vol. 24(11), 1991, PP. 1047-1058.
59. Harrigan, J. A., D. O. Kareh, D. W. O'Connor, D. W. Burke, and W. H. Harris. "A Finite Element Study of the Initiation of Failure of Fixation in Cemented Femoral Total Hip Components." *Journal of Orthopaedic Research*, Vol. 10, 1992, PP. 134-144.
60. Herman, G. T. *Image Reconstruction from Projections*. Academic Press, New York, 1980.
61. Hearman, R. F. S. *An Introduction to Applied Anisotropic Elasticity*. Oxford University Press, Oxford, 1961.
62. Hobatho, M. C., R. Darmana, P. Pastor, J. J. Barrau, S. Laboze, and J. P. Morucci. "Development of A Three-Dimensional Finite Element Model of A Human Tibia Using Experimental Modal Analysis." *Journal of Biomechanics*, Vol. 24(6), 1991, PP. 371-383.
63. Holden, J. P., and P. R. Cavanagh. "The Free Moment of Ground Reaction in Distance Running and Its Changes with Pronation." *Journal of Biomechanics*, Vol. 24(10), 1991, PP. 887-897.
64. Hsu, H. P., A. Garg, P. S. Walker, M. Spector, and F. C. Ewald. "Effect of Knee Component Alignment on Tibial Load Distribution With Clinical Correlation." *Clinical Orthopaedics and Related Research*, Vol. 248, 1989, PP. 135-144.
65. Hua, J., and P. S. Walker. "A Comparison of Cortical Strain after Cemented and Press-Fit Proximal and Distal Femoral Replacement." *Journal of Orthopaedic Research*, Vol. 10, 1992, PP. 739-744.
66. Huiskes, R. "On The Modelling of Long Bones in Structural Analyses." *Journal of Biomechanics*, Vol. 15(1), 1982.
67. Huiskes, R. "The Various Stress Patterns of Press-Fit, Ingrown, and Cemented Femoral Stems." *Clinical Orthopaedics and Related Research*, Vol. 261, 1990, PP. 27-38.

BIBLIOGRAPHY (Continued)

68. Huiskes, R., and E. Y. S. Chao. "A Survey of Finite Element Methods in Orthopedic Biomechanics: The First Decade." *Journal of Biomechanics*, Vol. 16, 1983, PP. 385-409.
69. Huiskes, R., and R. Boeklagen. "Mathematical Shape Optimization of Hip Prosthesis Design." *Journal of Biomechanics*, Vol. 22(8), 1989, PP. 793-804.
70. Huiskes, R., H. Weinans, H. J. Grootenboer, M. Dalstra, B. Fudala, and T. J. Slooff. "Adaptive Bone-Remodeling Theory Applied to Prosthetic-Design Analysis." *Journal of Biomechanics*, Vol. 20, 1987, PP. 1135-1151.
71. Huiskes, R., H. Weinans, and B. V. Rietbergen. "The Relationship Between Stress Shielding and Bone Resorption Around Total Hip Stems and the Effects of Flexible Materials." *Clinical Orthopaedics and Related Research*, Vol. 274, 1992, PP. 124-134.
72. Hvid, I., S. M. Bentzen, F. Linde, L. Mosekilde, and B. Pongsoipetch. "X-Ray Quantitative Computed Tomography: The Relations to Physical Properties of Proximal Tibial Trabecular Bone Specimens." *Journal of Biomechanics*, Vol. 22, 1989, PP. 837-844.
73. Kline, J. *Handbook of Biomedical Engineering*. Academic Press, Inc., California, 1988, PP. 243-312.
74. Kurosawa, H., P. S. Walker, S. Abe, A. Garg, and T. Hunter. "Geometry and Motion of The Knee for Implant and Orthotic Design." *Journal of Biomechanics*, Vol. 18(7), 1985, PP. 487-499.
75. Lafortune, M. A. "Three-Dimensional Acceleration of The Tibia During Walking and Running." *Journal of Biomechanics*, Vol. 24(10), 1991, PP. 877-886.
76. Lee, S. M. *Advances in Biomaterials*. Technomic Publishing Co., Pennsylvania, 1987.
77. Lewis, J. I., M. J. Askew, R. L. Wixson, G. M. Kramer, and R. R. Tarr. "The Influence of Prosthetic Stem Stiffness and of a Calcar Collar on Stresses in the Proximal End of the Femur with a Cemented Femoral Component." *The Journal of Bone and Joint Surgery*, Vol. 66A, 1984 PP. 280-286.
78. Lindberg, D. A., and P. L. Reichertz. *Lecture Notes in Medical Information*. Springer-Verlag, New York, 1981.

BIBLIOGRAPHY (Continued)

79. Linde, F., P. Norgaard, I. Hvid, A. Odgaard, and K. Soballe. "Mechanical Properties of Trabecular Bone Dependency on Strain Rate." *Journal of Biomechanics*, Vol. 24, 1991, PP. 803-809.
80. Magid, D., E. K. Fishman, and W. W. Scott. "CT Assessment with Multiplanar Reconstruction." *Radiology* 157: 751, 1985.
81. Mahanian, S., and R. Piziali. "Incompressibility in Bone." *Journal of Biomechanics*, Vol. 18(1), 1985, PP. 77-78.
82. Maistrelli, G. L., V. Fornasier, A. Binnington, K. Mckenzie, V. Sessa, and I. Harrington, "Effect of Stem Modulus in a Total Hip Arthroplasty Model." *The Journal of Bone and Joint Surgery*. Vol. 73B, 1991, PP. 43-46.
83. Mann, K. A., D. L. Bartel, T. M. Wright, and A. R. Ingradin. "Mechanical Characteristics of the Stem-Cement Interface." *Journal of Orthopaedic Research*, Vol. 9, 1991, PP. 798-808.
84. Marom, S. A. *Computer Aided Stress Analysis of Long Bones Utilizing Computed Tomography*. Doctoral Dissertation, N.J.I.T., 1986.
85. Marom, S. A., and M. J. Linden. "Computer Aided Stress Analysis of Long Bones Utilizing Computed Tomography." *Journal of Biomechanics*, Vol. 23(5), 1990, PP. 399-404.
86. Martell, J. M., R. H. Pierson, J. J. Jacobs, A. G. Rosenberg, M. Maley, and J. O. Galante, "Primary Total Hip Reconstruction with a Titanium Fiber-Coated Prosthesis Inserted without Cement." *The Journal of Bone and Joint Surgery*, Vol. 75A(4), April, 1993, PP. 554-571.
87. Martens, M., P. Van Andekercke, D. Delport, P. De Meester, and J. C. Mulier. "The Mechanical Characteristics of Cancellous Bone at The Upper Femoral Region." *Journal of Biomechanics*, Vol 16, 1983, PP. 971-983.
88. Martens, M., P. Van Andekercke, and J. C. Mulier. "Mechanical Behaviour of Femoral Bones in Bending Loading." *Journal of Biomechanics*, Vol 19(6), 1986, PP. 443-454.
89. Martin, R. B. "Determinants of The Mechanical Properties of Bones." *Journal of Biomechanics*, Vol. 24(1), 1991, PP. 79-88.

BIBLIOGRAPHY

(Continued)

90. Mcalister, G. B., and D. D. Moyle. "Some Mechanical Properties of Goose Femoral Cortical Bone." *Journal of Biomechanics*, Vol. 16(8), 1983, PP. 577-589.
91. McElhaney, J. M., J. L. Fogle, J. W. Melvin, R. P. Haynes, V. L. Roberts, and N. M. Alem. "Mechanical Properties of Cranial Bone." *Journal of Biomechanics*, Vol. 3, 1970, PP. 495-513.
92. McLeish, R. D., and J. Charnley. "Abduction Forces in The One-Legged Stance." *Journal of Biomechanics*, Vol. 3, 1970, PP. 191-209.
93. Mears, D. C. *Materials and Orthopaedic Surgery*. Williams & Wilkins, MD., 1979, PP. 29-82.
94. Mihalko, W. M., A. J. Beaudoin, J. A. Cardea, and W. R. Krause. "Finite Element Modelling of Femoral Shaft Fracture Fixation Techniques Post Total Hip Arthroplasty." *Journal of Biomechanics*, Vol. 25(5), 1992, PP. 469-476.
95. Minns, R. J., G. R. Bremble, and J. Campbell. "A Biomechanical Study of Internal Fixation of The Tibial Shaft." *Journal of Biomechanics*, Vol. 10, 1977, PP. 569-579.
96. Mont, M. A., D. C. Maar, K. A. Krackow, and D. Hungerford. "Hoop-Stress Fractures of The Proximal Femur During Hip Arthroplasty." *The Journal of Bone and Joint Surgery*, Vol. 74B, March, 1992, PP. 257-260.
97. Moyle, D. D., and R. W. Bowden. "Fracture of Human Femoral Bone." *Journal of Biomechanics*, Vol. 17(3), 1984, PP. 203-213.
98. Murase, K., R. D. Crowninshield, D. R. Pedersen. "An Analysis of Tibial Component Design in Total Knee Arthroplasty." *Journal of Biomechanics*, Vol. 16(1), 1982, PP. 13-22.
99. Nalcioglu, O., and Z. H. Cho. *Selected Topics in Image Science*. Springer-Verlag, New York, 1984.
100. Paul, J. P. *Bio-Engineering Studies of The Forces Transmitted by Joints. (II) Engineering Analysis*. Oxford, Pergamon Press, 1965, PP. 369-380.
101. Pilkington, T. C., B. Loftis, J. F. Thompson, S. L. Woo, T. C. Palmer, and T. F. Budinger. *High-Performance Computing in Biomedical Research*. CRC Press, Inc., Florida, 1993.

BIBLIOGRAPHY (Continued)

102. Pilliar, R. M., J. M. Lee, and C. Maniopoulos. "Observations on the Effect of Movement on Bone Ingrowth into Porous-Surfaced Implants." *Clinical Orthopaedics and Related Research*, Vol. 208, 1986, PP. 108-113.
103. Profio, A. E. *Biomedical Engineering*. John Wiley & Sons, Inc., New York, 1993, PP. 205-212.
104. Reddy, J. N. *An Introduction to The Finite Element Method*. McGraw-Hill, Inc., New York, 1984, PP. 1-11.
105. Reismann, H., and P. S. Powlik. *Elasticity, Theory and Applications*. John Wiley & Sons, Inc., New York, 1980, PP. 44-143.
106. Reilly, D., P. S. Walker, M. Ben-Dov, and F. C. Ewald. "Effects of Tibial Components on Load Transfer in the Upper Tibia." *Clinical Orthopaedics and Related Research*, Vol. 165, 1982, PP. 273-282.
107. Reilly, D. T., A. H. Burstein, V. H. Frankel. "The Elastic Modulus for Bone." *Journal of Biomechanics*, Vol. 7, 1974, PP. 271-275.
108. Reilly, D. T., and A. H. Burstein. "The Elastic and Ultimate Properties of Compact Bone Tissue." *Journal of Biomechanics*, Vol. 8, 1975, PP. 393-397.
109. Revell, P. A. *Pathology of Bone*. Academic Press, Inc, California, 1986, PP. 14-23.
110. Rice, J. C., S. C. Cowin, and J. A. Bowman. "On The Dependence of The Elasticity and Strength of Cancellous Bone on Apparent Density." *Journal of Biomechanics*, Vol. 21, 1988, PP. 155-168.
111. Rietbergen, B. V., R. Huiskes, H. Weinans, D. R. Summer, T. M. Turner, and J. O. Galante. "The Mechanism of Bone Remodeling and Resorption Around Press-Fitted THA Stems." *Journal of Biomechanics*, Vol. 26(4/5), 1993, PP. 369-382.
112. Robertson, D. D., and H. K. Huang. *Quantitative Measurement of Bone Using CT with Second Order Correction*. University Microfilms, Inc., 1984, PP. 37-67.
113. Rohl, L., E. Larsen, F. Linde, A. Odgaard, and J. Jorgensen. "Tensile and Compressive Properties of Cancellous Bone." *Journal of Biomechanics*, Vol. 24(12), 1991, PP. 1143-1149.

BIBLIOGRAPHY (Continued)

114. Rohlmann, E. J., E. J. Cheal, W. C. Hayes, and G. Bergmann. "A Nonlinear Finite Element Analysis of Interface Conditions in Porous Coated Hip Endoprostheses." *Journal of Biomechanics*, Vol 21(7), 1988, PP. 605-611.
115. Rohrlé, H., R. Scholten, C. Sigolotto, W. Sollbach, and H. Kellner, "Joint Forces in The Human Pelvis-Leg Skeleton During Walking." *Journal of Biomechanics*, Vol. 17, 1984, PP. 409-424.
116. Rubin, P. J., P. F. Leyvraz, J. M. Aubaniac, J. N. Argenson, and P. Esteve. "The Morphology of the Proximal Femur: A Three-Dimensional Radiographic Analysis." *The Journal of Bone and Joint Surgery*, Vol. 74B, 1992, PP. 28-32.
117. Rubin, P. J., P. E. Rakotomanana, P. K. Leyvraz, P. K. Zysset, A. Curnier, and J. H. Heegaard. "Frictional Interface Micromotions and Anisotropic Stress Distribution In a Femoral Total Hip Component." *Journal of Biomechanics*, Vol. 26(6), 1993, PP. 725-739.
118. Salathe, E. P., and G. A. Arangio, "An Application of Beam Theory to Determine The Stress and Deformation of Long Bone." *Journal of Biomechanics*, Vol. 22(3), 1989, PP. 189-199.
119. Schaffler, M. B., and D. B. Burr. "Stiffness of Compact Bone: Effects of Porosity and Density." *Journal of Biomechanics*, Vol. 21(1), 1988, PP. 13-16.
120. Schmid-Schonbein, G. W., S. L. Y. Woo, and B. W. Zweifach. *Frontiers in Biomechanics*. Springer-Verlag, New York, 1985, PP. 245-262.
121. Scott, W. W., Jr. D. Magid, and E. K. Fishman. *Computed Tomography of The Musculoskeletal System*. University Park, Press, Baltimore, 1987.
122. *Siemens*, Operating Instructions - Somatom DR CT scanner, Version G/G1/H, 1986.
123. *Siemens*, Technical Information - Rotation Fan Beam CT Systems: Principles, 1978.
124. Simon, B. R., S. L. Woo, G. M. Stanley, S. R. Olmstead, M. P. McCarty, G. F. Jemmott, and W. H. Akeson. "Evaluation of One-, Two-, and Three-Dimensional Finite Element and Experimental Models of Internal Fixation Plate." *Journal of Biomechanics*, Vol. 10, 1977, PP. 79-86.
125. Skalak, R., and S. Chien. *Handbook of Bioengineering*. McGraw-Hill Book Co., New York, 1987, PP. 40.1-40.25.

BIBLIOGRAPHY (Continued)

126. Stark, K. *Image Recovery: Theory and Application*. Academic Press, Inc., Florida, 1987, PP. 321-368.
127. Sumner, D. R., C. L. Olson, P. M. Freeman, J. J. Lobick, and T. P. Andriacchi. "Computed Tomographic Measurement of Cortical Bone Geometry." *Journal of Biomechanics*, Vol. 22(6), 1989, PP. 649-653.
128. *Surgical Overview and Technique for the Porous Primary Series*. Manufacture's Introduction on Surgical Techniques and Prosthesis, Biomet Inc., Indiana, 1992.
129. Svensson, N. L., S. Valliappan, and R. D. Wood. "Stress Analysis of Human Femur With Implanted Charnley Prosthesis." *Journal of Biomechanics*, Vol. 10, 1977, PP. 581-588.
130. Technical Note, "On The Modelling of Long Bones in Structural Analyses." *Journal of Biomechanics*, Vol. 15(1), 1982, PP. 65-69.
131. *The BDH Universal Hip System*. Manufacture's Introduction on Surgical Techniques and Prosthesis, Intermedics Orthopedic, TX., 1984.
132. Timoshenko, S., and J. Goodier. *Theory of Elasticity*. McGraw-Hill, Inc., 1970, PP. 200-387.
133. *Total Hip System*. Manufacture's Manual, Zimmer Co., Indiana, 1982.
134. Turner, T. M., R. M. Urban, D. R. Sumner, and J. O. Galante. "Revision, without Cement, of Aseptically Loose, Cemented Total Hip Prostheses." *The Journal of Bone and Joint Surgery*, Vol. 75A, 1993, PP. 845-862.
135. Udupa, J. K., and G. T. Herman. *3D Imaging in Medicine*. CRC Press, Inc., Florida, 1991.
136. Ugural, A. C., and S. K. Fenster. *Advanced Strength and Applied Elasticity*. New York, 1982, PP. 1-58.
137. Van Buskirk, W. C., R. B. Ashman. "The Elastic Moduli of Bone." *ASME Applied Mechanics Division*, Vol. 45, 1981, PP. 131-143.
138. Vasu, R., D. R. Carter, D. J. Schurman, and G. S. Beaupre. "Epiphyseal-Based Designs for Tibial Plateau Components — I. Stress Analysis in The Frontal Plane." *Journal of Biomechanics*, Vol. 19(8), 1986, PP. 647-662.

BIBLIOGRAPHY (Continued)

139. Walker, P. S., C. Ranawat, and J. Insall. "Fixation of The Tibial Components Of Condylar Replacement Knee Prosthesis." *Journal of Biomechanics*, Vol. 9, 1976, PP. 269-275.
140. Weinans, H., R. Huiskes, and H. J. Grootenboer. "Trends of Mechanical Consequences and Modeling of a Fibrous Membrane Around Femoral Hip Prostheses." *Journal of Biomechanics*, Vol. 23, 1990, PP. 991-1000.
141. Weinans, H., R. Huiskes, B. Van Rietbergen, D. R. Sumner, T. M. Turner, and J. O. Galante. "Adaptive Bone Remodeling Around Bonded Noncemented Total Hip Arthroplasty: A Comparison Between Animal Experiments and Computer Simulation." *Journal of Orthopaedic Research*, Vol. 11, 1993, PP. 500-513.
142. Weisberg, L. A., C. Nice, and M. Katz. *Cerebral Computed Tomography*. W. B. Saunders, Co., Philadelphia, 1978, PP. 10-27.
143. Wheeler, P. R., and H. G. Burkitt. *Skeletal Tissues*. Churchill Livingstone, New York, 1987, PP. 52-142.
144. Whiteside, L. A., and J. Pafford. "Load Transfer Characteristics of a Noncemented Total Knee Arthroplasty." *Clinical Orthopaedics and Related Research*, Vol. 239, 1989, PP. 168-177.
145. Williams, J. F., and N. L. Svensson. "A Force Analysis of The Hip Joint." *Biomedical Engineering*, Vol. 3, 1968, PP. 365-370.
146. Williams, J. L., J. L. Lewis. "Properties and An Anisotropic Tibial Epiphysis Model of Cancellous Bone from The Proximal Tibial." *Journal of Biomechanical Engineering*, Vol. 104, February, 1982, PP. 50-56.
147. Woodburne, R. T. *Essentials of Human Anatomy*. Oxford University Press, New York, 1983, PP. 547-549.
148. Woolson, S. T., P. Dev, L. L. Fellingham, and A. Vassiliadis. "Three-Dimensional Imaging of Bone from Computerized Tomography." *Clinical Orthopaedics and Related Research*, Vol. 202, January, 1986, PP. 239-248.
149. Yoon, H. S., and J. L. Katz. "Ultrasonic Wave Propagation in Human Cortical Bone. II. Measurement of Elastic Properties and Micro-Hardness." *Journal of Biomechanics*, Vol. 9, 1976, PP. 459-466.